NTNU

Norwegian University of
Science and Technology

Characterization of Solar Cell Wafers with Low Coherence Interferometry

Ove Simonsen

Master of Science in Electronics
Submission date: July 2011
Supervisor: Astrid Aksnes, IET
Co-supervisor: Lars Johnsen, Sintef

Norwegian University of Science and Technology
Department of Electronics and Telecommunications

Problem description

Characterization of Solar Cell Wafers with Low Coherence Interferometry

The goal of this project is to characterize wafers used in solar cell production. A low coherence interferometer was built for this purpose by Ove Simonsen in his project the fall of 2010. This LCI setup will be modified to increase the resolution and to quantify measurements. Finally measurements on silicon samples with defects will be performed.

Background: To make the solar cell industry more competitive opposed to traditional energy sources the efficiency of the production of solar cell wafers must be improved. Wafers are hence cut as thin as possible to increase the number of wafers per silicon block. After the sawing process the wafers are tested and inspected according to strict quality requirements. As the quality requirements increase new equipment is needed to characterize the silicon wafers and detect defects (cracks, inclusions and surface imperfections). As silicon is transparent for wavelengths in the range of 1.25µm to approximately 6µm NIR-interferometry is an excellent tool for characterizing silicon wafers. It is of special interest to detect the micro cracks in the surface as these micro cracks reduce the mechanical tensile strength of the wafer.

Assignment: To modify and further develop an existing LCI setup to work with wavelengths > 1250nm. All components are available in the Optical measurement laboratory at SINTEF. To verify that the LCI setup functions, characterization of simple defects (large cracks) will be performed first. Focus will be on improving the resolution and keeping control of different depth levels. Finally micro cracks in the surface which require a high spatial resolution will be characterized.

Outline of work:

1. Theoretical investigations of achievable spatial and axial resolution
2. Further develop the LCI setup (initially built by Ove Simonsen).
    a. Determine which parts are critical to achieve high resolution and optimize the setup to increase the resolution
    b. Include more functionality in software to control the LCI setup.
    c. Use phase step algorithms as a tool to quantify measurements
3. Carry out measurements on different samples with the LCI system.
4. Compare measurements with the LCI system with other measurement techniques.

Summary:

Characterize silicon wafers used in solar cell production with a NIR-LCI interferometer. The interferometer is further developed and measurements on silicon samples are carried out.

1 Abstract

Silicon wafers are traditionally used for solar cell production. The process of making these wafers is by a multi-wire saw. Slurry consisting of silicon carbide particles and polyethylene glycol is responsible for the material removal. The silicon carbide particles work as small indentations in the silicon and lead to chips of silicon being removed. The sawing process produces imperfect surfaces which contain small cracks and defects. To characterize these defects and cracks microscopy is traditionally used. This means that sawed wafers are inspected, but not the process in-situ.

The aim of this project is to further develop a near infrared (NIR) low coherence interferometer (LCI) to examine the sawing process. This is done by using a Vickers indenter to simulate how a single silicon carbide particle works on the silicon surface. The main focus in this report is the optical and electrical aspects of the setup.

Low coherent interferometry is utilized to extract the surface topography of silicon during indentations. Silicon is nearly transparent for wavelengths in the range $1.25\mu m$ to approximately $6\mu m$. Choosing a source in the near infrared region makes it possible to image the indentation from the inside as this is most practical and proved the best view.

The deformation is in the micrometer scale, and high resolution is thus required. For increasing the spatial resolution the concept of solid immersion is utilized. The spatial resolution is a trade-off between the depth of focus. The depth of focus and coherence length of the system decides the axial resolution of the LCI setup. The spatial resolution of the system is investigated experimentally. How different components of the system affect the spatial resolution is accounted for.

Indentations in a silicon samples with the (100) and (111) planes pointing out of the samples are carried out. A Vickers tip is used as an indenter. The corners of the Vickers with respect to the crystal lattice of silicon is considered. The phase maps from the indentations require interpretation, and areas of the indentation may contain false depth information due to multiple reflections, abrupt surfaces and reflection from too large angles.

The recorded phase maps from an indentation can be used for depth measurements. The depth of an indentation is investigated, where a confocal microscope image with a corresponding depth profile is used as a reference. A mismatch between the confocal microscope image and the phase map is found. Chippings with large angles result in an interference pattern with closely spaced fringes. At a

specific angle the fringes are so close they cannot be resolved by the setup. With increased optical resolution the system can characterize chippings with larger angles.

2 Preface

This project was written in the fifth year of the master's program in Electrical Engineering at the Norwegian University of Science and Technology. This project is a part of a bigger project at SINTEF. Lars Johnsen is running the project and the Department for Optical Measurements at SINTEF has worked with the specific problem before this thesis started. My main supervisor has been Lars Johnsen and I am grateful for the super support that I have received from him during this thesis. He always had time for a discussion and the discussions topic was always much simpler and clearer after a talk with Lars. He's experience and lab expertise has been of great value to me and the project.

Astrid Aksnes has been my teaching supervisor for the thesis. Her abilities to figure out which parts of the project that is of importance have kept me going in the right direction. The structure and flow of this report has improved with Astrid's assistance.

Kay Gastinger was my supervisor in the fall of 2010 and was a bigger part of the project when he was working for SINTEF. Even though he has a new job now, he is still involved in this project. Every time we spoke he had new initiatives and he has been a great source for LCI information.

Due to the enthusiasm of my supervisors I was very lucky to attend the congress Optical Metrology in Munich. During that conference I learned a lot from attending presentations and seeing so many other working with optics was an inspiration.

Wilhelm Dall must be thanked for carrying out the measurements where the lattice direction of the samples was found. I learned a lot about EBSD and the electron microscope when spending time with him. Søren Heinze performed measurements on one of my samples in the electron microscope in the Nanolab. I am grateful for he's help and the measurements he performed are of value to the project. The Mechanical workshop at NTNU has contributed in making parts to the current setup. Their efficiency and precision is much appreciated. At last Sergio Armada must be thanked for the work he has done with the confocal microscope. He's measurements has helped us to understand our system better.

Contents

1 Abstract **i**

2 Preface **iii**

3 Introduction **1**

3.1 Motivation . . . 1

3.2 Contribution . . . 1

3.3 Outline . . . 3

4 Theory **4**

4.1 Interferometry . . . 4

4.1.1 Interference . . . 5

4.1.2 Coherence . . . 8

4.1.3 Low Coherence Interferometry . . . 11

4.2 Resolution . . . 16

4.2.1 Spatial resolution . . . 16

4.2.2 Axial resolution . . . 20

4.2.3 Example with a silicon lens . . . 21

4.2.4 Aberration . . . 23

4.3 Phase . . . 25

4.3.1 Phase-stepping . . . 25

4.3.2 Fresnels equations . . . 27

4.4 Newton fringes . . . 28

4.5 Electron Backscatter Diffraction . . . 30

4.6 Wafer sawing . . . 32

4.7 Analog to Digital . . . 34

5 Experimental setup **36**

5.1 Optical setup . . . 36

5.1.1 Interferometer configuration . . . 36

5.1.2 Components . . . 40

5.2 Electrical setup . . . 45

5.2.1 Overview . . . 45
5.2.2 Programming . . . 46

6 Results **50**
6.1 Resolution . . . 50
6.2 Indentation . . . 57
6.2.1 Sample 1 . . . 57
6.2.2 Sample 2 . . . 61
6.2.3 Sample 3 . . . 63
6.3 Quantification . . . 66

7 Discussion **68**
7.1 Resolution . . . 68
7.2 General indentation . . . 69
7.3 Sample differences . . . 71
7.4 Quantification . . . 71
7.5 Advantages and limitations of the LCI technique . . . 74

8 Future work **75**

9 Conclusion **77**

A Appendix **81**
A.1 Paper . . . 81
A.2 Custom Parts . . . 91
A.3 Superluminescent diode datasheet . . . 93
A.4 Xenics NIR camera . . . 95
A.5 Mitutoyo NIR microscope objective . . . 98
A.6 Piezoelectric actuator PAS005 . . . 100
A.7 Piezoelectric actuator PAZ020 . . . 102
A.8 National instruments 9263 . . . 104
A.9 LabVIEW code for calibrating the phase-step piezo . . . 107
A.10 LabVIEW code for recording a phase map . . . 109
A.11 LabVIEW code for ramping the piezo . . . 111
A.12 LabVIEW code for indentation and phase recording . . . 113

3 Introduction

3.1 Motivation

Silicon is the main material used in solar cell production, and over 95% of all commercial solar cells are made from silicon [1]. Silicon is manufactured into long blocks and cut into thin wafers by multi-wire sawing. These wafers are usually from 150um to 180um thick, and can be used for solar cell production. During the sawing process surface defects on the wafer are introduced. These surface defects may lead to problems later on in the production and the quality of these wafers is critical for solar cell production. Efficiency and price of the solar cell is also dependent on the wafer quality. For that reason the fabrication of the wafer is the most part of producing a solar cell.

An improvement of the sawing process is of interest as this will reduce the cost of solar cells. This requires knowledge of how the sawing process works. Investigation of a sawed wafer can provide information about this process. Examinations of sawed wafers and simulation of the sawing process reveal deformations and cracks in the silicon. The defects and cracks are located and studied, and the results are used to develop theories of how the deformation occured during the sawing process. Inspecting this process optically may introduce new information on the subject of wafer sawing.

There are different tools used for examination of wafers and simulated sawing processes. Investigation of cracks has been done by the use of a transmission electron microscope(TEM) [1]. This provides high resolution images of the small cracks made by the sawing process. Another attempt to understand the silicon behavior has been to introduce cracks with a Vickers [2]. Vickers is a tool usually used to test the hardness of materials. A Vickers indenter was used to make defects/indentations in the silicon. The silicon samples were then investigated with high-voltage electron microscopy (HVEM) and atomic force microscopy (AFM) afterwards.

3.2 Contribution

The aim of this project is to further develop a setup that can investigate in-situ how the sawing process takes place. During the cutting process, the surface of the silicon is covered with slurry (sharp particles and carrier liquid) and a steel wire drives this slurry around the silicon. Examining the cutting process from the surface is therefore difficult. The setup used in this project exploits the fact that silicon is transparent for light with wavelengths in the range $1.25\mu m$ to approximately $6\mu m$. The cutting process will be studied from the inside of the silicon.

The idea and proof of principle for the setup built in this project was already carried out and presented by Kay Gastinger and Lars Johnsen in [3] before this project started. A first model of the setup was built in my project assignment in fall 2010. This setup is based on a Michelson interferometer to obtain phase maps of the inside of a silicon sample. The technique of solid immersion is utilized to improve the resolution of the system. My contribution to the ongoing project is primarily further development of the optical and electrical setup and carrying out experiments on different silicon samples. A more precise description of what that includes is provided in this project report.

Optical setup - The optical and electrical parts are investigated for the setup to perform as desired. How the different parts of the optical system affect the level of detail achieved by the system is thoroughly examined. This is also theoretically investigated.

Programming - Programs for controlling the electronic part of the setup are updated for better measurements and made more user-friendly. LabVIEW is the main program which implements the different parts while MatLab is the preferred program for calculations.

Resolution investigations - Investigating which parts of the setup that affects the level of detail that can be achieved is important. To measure the level of detail, the optical resolution of the system is considered. The optical resolution is examined both experimentally and theoretically. A systematic study of how the different parts influence the optical resolution is carried out. As a measuring standard a sample with a custom made resolution chart is used.

Indentation - Several measurements are performed with an indentation. The indentation was made by pressing a Vickers indent into the silicon sample. The microscopic deformation that takes place is captured in-situ and investigated. The crystal lattice of silicon has a diamond structure, and two different samples which are cut along the (100) and (111) planes are examined. The angle of the Vickers indenter is also of importance.

Paper - Parts of the work done in fall 2010 and in this thesis was presented at the Optical Metrology conference in Munich in May 2011. I attended the conference and Lars Johnsen from SINTEF presented the work. Along with the presentation a paper on the subject was written. The name of the paper is 'Inspection of processes during silicon wafer sawing using low coherence interferometry in the near infrared wavelength region' and is attached in appendix A.1. My contribution was the theory on imaging and experimental results chapters as well as performing the experimental results.

3.3 Outline

The report starts with background theory about interferometry and coherence. Further theory about resolution of an optical system is presented followed by theory about the phase of the light and Newton fringes. Electron backscatter diffraction, wafer sawing and the sampling theorem is presented last in the theory chapter. The experimental setup is then reviewed followed by the results. The results are separated into three parts consisting of resolution measurements, indentation and quantification of a chipping. The results are discussed in chapter 6 and conclusions are summarized in chapter 9. Some suggestions for improving the setup is presented in chapter 8.

4 Theory

This chapter will cover the background information in form of theory that is the basis for the project. The optical setup is based on interferometry and is described first. Basic theory about resolution with specific examples concerning this particular project is provided next. The last two sections contain theory about how wafers for solar cells are manufactured and an introduction to phase-stepping.

4.1 Interferometry

Interference is one of the fundamental phenomena of the wave theory and results from the superposition of electromagnetic waves. When two or more waves are simultaneously present in the same place at the same time, the total wave is a sum of all individual waves. This is called interference and arises if the waves are coherent or partly coherent. The derivations regarding interference, coherence and low coherence interferometry in this chapter follows Saleh and Teich [4].

To be sure that the two waves interfering are coherent, the waves typically emerge from the same source. They are led into two different beam paths, and are recombined in a detector. The detector will observe the interference pattern the two waves produce. This splitting and recombination of waves can be achieved in several ways and is the general concept for interferometry. In this chapter it will be illustrated with a Michelson interferometer, as shown in figure 4.1.

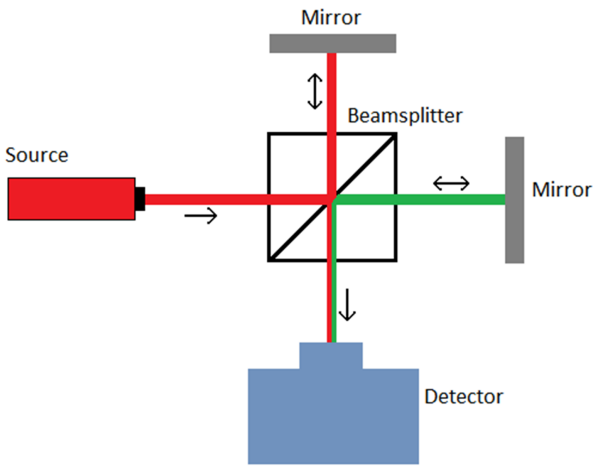

Figure 4.1: A sketch of a Michelson interferometer

4.1.1 Interference

Interference of two waves
If we consider an optical wave $u(\vec{r}, t)$ it is convenient to represent it in terms of a complex function. A monochromatic wave can be represented as in equation 4.1.

$$u(\vec{r}, t) = a(\vec{r})cos[2\pi\nu t + \phi(\vec{r})] \tag{4.1}$$

a	Amplitude of the wave
$\vec{r}$	Position vector
ν	Optical frequency
ϕ	Phase

The real wavefunction 4.1 can be represented in terms of the complex function

$$U(\vec{r}, t) = a(\vec{r})\mathrm{e}^{j\phi(\vec{r})}\mathrm{e}^{j2\pi\nu t} \tag{4.2}$$

where $U(\vec{r})$ is referred to as the complex amplitude. The complex amplitude contains information about the amplitude and phase of the wave at a position $\vec{r}$ and is independent t.

A wave with complex amplitude, $U(\vec{r})$, is sent from the source and split into two waves by a beamsplitter as illustrated in figure 4.1. Both beams will be reflected at each mirror and sent back to the beamsplitter where they are combined again. When the beams are split, one beam is introduced as the reference beam, and the other as the object beam. When these two waves are superposed at a point $\vec{r}$ they have a field described by the total complex amplitude given by

$$U_{tot}(\vec{r}) = U_1(\vec{r}) + U_2(\vec{r}). \tag{4.3}$$

U_{tot}	Total complex electric field
U_1	Complex electric field from the reference beam
U_2	Complex electric field from the object beam

The complex electric fields U_1 and U_2 are here the complex fields of each beam given by $a_1(\vec{r})\mathrm{e}^{j\phi_1(\vec{r})}$ and $a_2(\vec{r})\mathrm{e}^{j\phi_2(\vec{r})}$, respectively. The detector cannot measure complex amplitude, only time average intensity. The optical intensity is proportional to the average of the squared wavefunction. Thus the total intensity will, if we neglect the explicit dependency on $\vec{r}$, be expressed as

$$\begin{aligned} I &= |U_{tot}|^2 = |U_1 + U_2|^2 \\ &= U_1^2 + U_2^2 + U_1 U_2^* + U_1^* U_2. \end{aligned} \tag{4.4}$$

where * is the complex conjugate.

Laser interferometry

For laser interferometry the coherence length of the source is normally longer than the optical system. This means that the source can be considered as fully coherent. For laser interferometry we can exploit the rules of complex numbers and trigonometric relations [5] and rewrite equation 4.4 yielding

$$I = I_1 + I_2 + 2\sqrt{I_1 I_2}\cos(\phi). \tag{4.5}$$

I_1	Intensity of the object beam
I_2	Intensity of the reference beam
ϕ	Phase difference between the object and reference beam

I_1 and I_2 correspond to the intensity of the two beams. The third term represents the interference term, where $\phi = \phi_2 - \phi_1$. Due to the interference term it is clear that the sum of the two waves is not equal to the sum of their intensities. The interference term is strongly dependent on the phase difference of the two waves. As it is dependent on a cosine term, it can take positive as well as negative values. It is this interference term which is interesting to investigate.

When considering various phase differences, expressions for maximum and minimum intensity can be obtained. Minimum intensity is achieved when $cos(\phi) = -1$ which means that $\phi_2 - \phi_1$ must be an integer times 2 π. The total intensity is then given by $I_{min} = I_1 + I_2 - 2\sqrt{I_1 I_2}$. This case is called destructive interference. Maximum intensity, constructive interference, is achieved when $\phi_2 - \phi_1$ is π times an integer. This gives $cos(\phi) = 1$ and results in $I_{max} = I_1 + I_2 + 2\sqrt{I_1 I_2}$.

In the case where the two beams have equal intensity it is easily seen that the minimum intensity is 0, and maximum is $4I$. For the special case where $\phi_2 - \phi_1$ results in an integer times $\pi/2$, the interference term vanishes.

Michelson interferometer

When considering the situation in figure 4.1, the distance from the beamsplitter to each mirror is equal. This will give a phase difference of zero and results in constructive interference. Placing one of the mirrors in a different distance from the beamsplitter than the other mirror, will introduce a different optical path length in one of the beams. The mirror that can be moved is referred to as the reference mirror and the beam that is reflected by this mirror is the reference beam. This difference in optical path length can be one cause for the phase difference $\phi = \phi_2 - \phi_1$ mentioned in the previous section. Figure 4.2 illustrates the displacement of a mirror, where the reference mirror can be moved with respect to the beamsplitter.

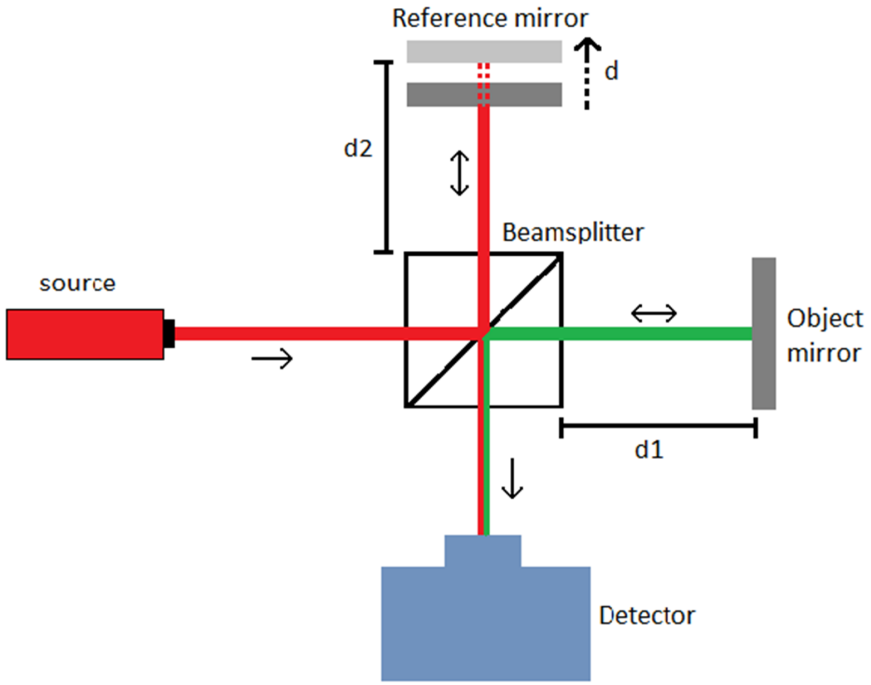

Figure 4.2: Sketch of a Michelson interferometer where the reference mirror can be moved with respect to the beamsplitter.

The change in optical path length results in a phase difference of the two beams at the detector. This means that we investigate the phase difference between the two waves by looking at the intensity of the superposed waves. The interference equation for a reference and object beam with equal intensity can be obtained by rewriting equation 4.5. Using $I_1 = I_2 = I_0$ and $\phi = kd = 2\pi d/\lambda$ we acquire equation 4.6. Here d is the optical path length difference between the reference and object beam.

$$I = 2I_0[1 + \cos(\phi)] = 2I_0[1 + \cos(\frac{2\pi d}{\lambda})] \tag{4.6}$$

The intensity dependence on phase is illustrated in figure 4.3.

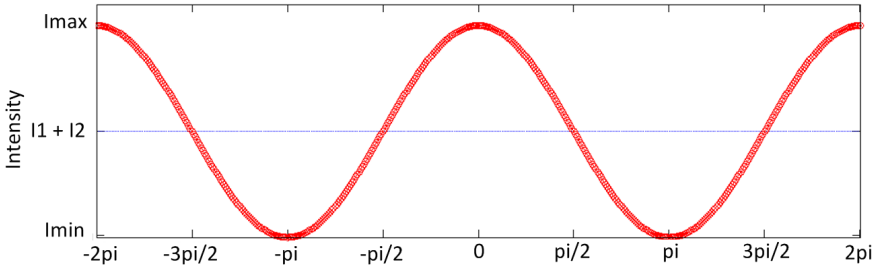

Figure 4.3: Total intensity of two interfering waves as a function of phase difference when $I_1 = I_2 = I_0$.

If we investigate the cosine argument it is obvious that $2\pi d/\lambda = 2\pi nd/\lambda_0 = 2\pi n\nu d/c_0$, where n is the refractive index, ν optical frequency and d the optical path length difference. This means that a small change in refractive index, frequency or distance can be observed by examining the intensity.

4.1.2 Coherence

When considering random light, $U(\vec{r}, t)$ is a random function of position and time. The light is said to be random because of unpredictable fluctuations of the source or of the medium it propagates in. The opposite of random light can be a monochromatic wave which consists of only one wavelength. The field dependence of time and position of a monochromatic wave is predictable and therefore not random. The coherence is also dependent on the bandwidth of the light. When the light consists of several frequencies the degree of coherence will decrease.

Degree of coherence

The intensity of random light will also vary with time and position, and is given by averaging over many realizations of the random function. In the case where

light is stationary the average intensity is constant and does not vary with time. The average intensity of stationary light can be calculated by taking a time average over a long period of time instead of averaging over several realizations of the light beam. The intensity will in this situation be given by

$$I(\vec{r}) = \lim_{T\to\infty} \frac{1}{2T} \int_{-T}^{T} |U(\vec{r},t)|^2 \, dt. \tag{4.7}$$

The random fluctuations of $U(\vec{r},t)$ can be described by a time period representing the "memory" of the random function. After this period the function has no correlation with the original wave. If we look at two samples from a wave which are separated in time with a period longer than the memory of the random function, they will be independent of each other. On the other hand, if the two samples are taken within the memory time, they would be dependent to a certain degree. This memory-like behavior can be determined by the autocorrelation function, given by

$$G(\tau) = \lim_{T\to\infty} \frac{1}{2T} \int_{-T}^{T} U^*(t)U(t+\tau), dt. \tag{4.8}$$

This function describes how much dependence two wave functions , which are separated by a certain time, have on each other. The autocorrelation function is for optical coherence theory known as the temporal coherence function. Since $\vec{r}$ is fixed, we can for simplicity skip the $\vec{r}$-dependence in the equation.

The temporal coherence function contains information about intensity and degree of correlation. From equation 4.8 we see that $G(0)$ is equal to the intensity. To obtain the normalized autocorrelation function we divide equation 4.8 with $G(0)$,

$$g(\tau) = \frac{G(\tau)}{G(0)} = \frac{\langle U^*(t)U(t+\tau)\rangle}{\langle U^*(t)U(t)\rangle} \tag{4.9}$$

where $\langle . \rangle$ denotes the time average. $g(\tau)$ is called the complex degree of temporal coherence and can have values from 0 to 1. $g(\tau)$ equal to 1 indicates that the wave is fully coherent, e.g. a monochromatic wave. $g(\tau)$ contains only the degree of coherence between two wave functions separated by a time delay τ.

Equation 4.9 can be used to determine the coherence time of a function. If $g(\tau)$ of the investigated function drops below a prescribed value, often 1/2, this can be used as measurement of the memory time of the fluctuations. Figure 4.4 illustrates the coherence function and a measure of coherence time.

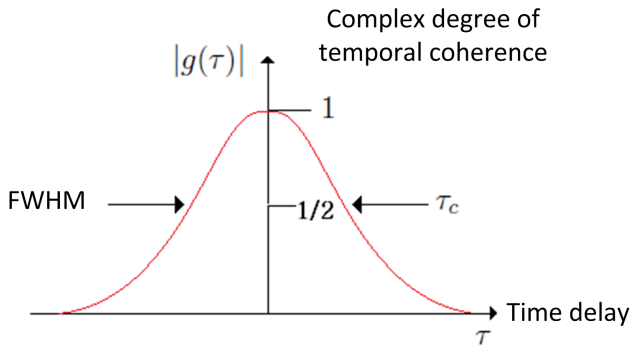

Figure 4.4: Complex degree of temporal coherence as a function of τ, and the indicated coherence time. Here described with FWHM.

As mentioned above the coherence time can have several definitions. Full Width at Half Maximum, FWHM is frequently used with laser sources. The coherence length of the source is proportional to the coherence time as defined by

$$l_c = c\tau_c \tag{4.10}$$

where c is the speed of light.

Mutual coherence

The temporal coherence function describes the correlation of a wave with itself. To describe the coherence between two waves we introduce the mutual coherence function. The mutual coherence function considers the degree of coherence of two waves at position $\vec{r_1}$ and $\vec{r_2}$, where $\vec{r_2}$ is delayed with τ in time,

$$G(\vec{r_1}, \vec{r_2}, \tau) = \langle U^*(\vec{r_1}, t)U(\vec{r_2}, t+\tau)\rangle\,. \tag{4.11}$$

We can obtain the normalized form of equation 4.11 with the same procedure as we did for the complex degree of temporal coherence. Dividing by $G(\vec{r_1}, \vec{r_2}, 0)$ provides equation 4.12, which is known as the complex degree of coherence.

$$g(\vec{r_1}, \vec{r_2}, \tau) = \frac{G(\vec{r_1}, \vec{r_2}, \tau)}{\sqrt{I(\vec{r_1})I(\vec{r_2})}} \tag{4.12}$$

In the case where $\vec{r_1}$ equals $\vec{r_2}$, equation 4.12 will reproduce the complex degree of temporal coherence function in equation 4.9.

4.1.3 Low Coherence Interferometry

Low coherence interferometry,LCI, is based on a standard interferometer with a low coherent source. The strength of the interference will decrease as the interfering waves become less and less coherent.

Interference equation

To obtain the low coherence interference equation, the time average intensity has to be calculated. This will include the degree of coherence and can be done by time averaging equation 4.4.

$$\begin{aligned} I &= \left\langle U_1^2 \right\rangle + \left\langle U_2^2 \right\rangle + \langle U_1^* U_2 \rangle + \langle U_1 U_2^* \rangle \\ &= I_1 + I_2 + G_{12} + G_{12}^* \\ &= I_1 + I_2 + 2\Re[G_{12}] \end{aligned} \tag{4.13}$$

Here $\langle U_1^* U_2 \rangle = G(\vec{r_1}, \vec{r_2}, 0) = G_{12}$ is the cross-correlation term.

It is useful to introduce the normalized coherence term of two waves from equation 4.12. Solving equation 4.12 for G_{12} provides a new expression for the interference equation given by

$$I = I_1 + I_2 + 2\sqrt{I_1 I_2}\cos(\phi)|g_{12}|. \tag{4.14}$$

It is seen from equation 4.14 that the interference term is strongly dependent on the degree of coherence. If the two beams are mutually coherent, g_{12} is equal to 1 and we acquire the original interference equation, 4.5. If the two beams are completely uncorrelated, g_{12} is equal to 0 and the total intensity reduces to

$I = I_1 + I_2$.

In chapter 4.1.1 we examined a Michelson interferometer with a coherent source at certain mirror displacements. Figure 4.3 showed that the interference signal was given by a cosine function. Doing the same experiment with a low coherent source will provide a different result.

Inserting $I_1 = I_2 = I_0$ in equation 4.14 generates

$$I = 2I_0[1 + |g_{12}| \cos(\frac{2\pi d}{\lambda})]. \tag{4.15}$$

We consider a source with a normalized autocorrelation function as in figure 4.4. The normalized autocorrelation function is monotonically decreasing with increasing τ. As the mirror separation d, and hence τ, increases, the interference term will decrease. This is relevant for all interferometers, but when the optical path difference in the two arms of the interferometer is shorter than the coherence length, the interference will not disappear. The intensity dependence on τ is illustrated in figure 4.5.

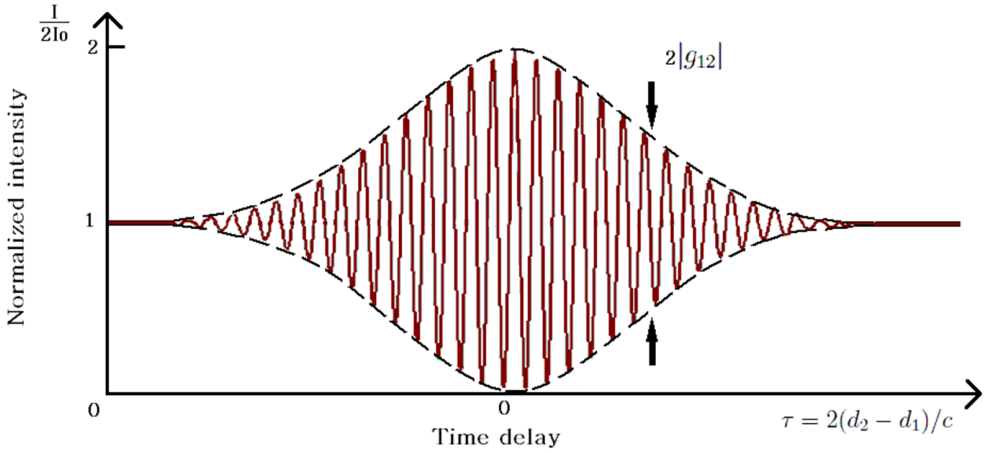

Figure 4.5: Normalized intensity as a function of time delay, τ, for two interfering waves. The coherence length is shorter than the OPD in the two armes of the interferometer.[Reprint from Saleh and Teich [4]]

Figure 4.5 shows that the interference is strongly dependent on the degree of coherence. The interference term will vanish if the mirror displacement becomes

large enough. This means that the coherence length decides the maximum mirror displacement when we experience interference.

Visibility is a measure of how strong the interference is. That means that it is a measure for how good contrast there is between constructive and destructive interference. The visibility is defined by

$$V = \frac{I_{max} - I_{min}}{I_{max} + I_{min}}, \tag{4.16}$$

Where Imin and Imax is found by changing the phase, ϕ. Imax and Imin are both dependent on the degree of coherence, $|g_{12}|$. Still considering the case where $I_1 = I_2 = I_0$ equation 4.16 reduces to

$$V = |g_{12}|. \tag{4.17}$$

Coherence Layer

When a low coherent source is used, interference can only be detected within a certain distance. The volume wherein interference is observed is called the coherence layer. The coherence layer is determined by the coherence length of the source, illustrated in figure 4.4. In the case of a Michelson interferometer the coherence layer is not equal to the coherence length of the source due to the fact that the Michelson interferometer is a double path interferometer.

With the use of a low coherent source and a Michelson interferometer, low coherent interferometry is obtained. If the object mirror in figure 4.2 was to be replaced with a rough surface, LCI could be used to investigate the surface. Consider the case where the rough surface has a slope topography as in figure 4.6. The object beam that hits the surface will be reflected along the whole slope, but only beams that are coherent with the reference beam will contribute to the interference observed at the detector. The FWHM of the interference signal determines the coherence layer and is illustrated with red lines in 4.6.

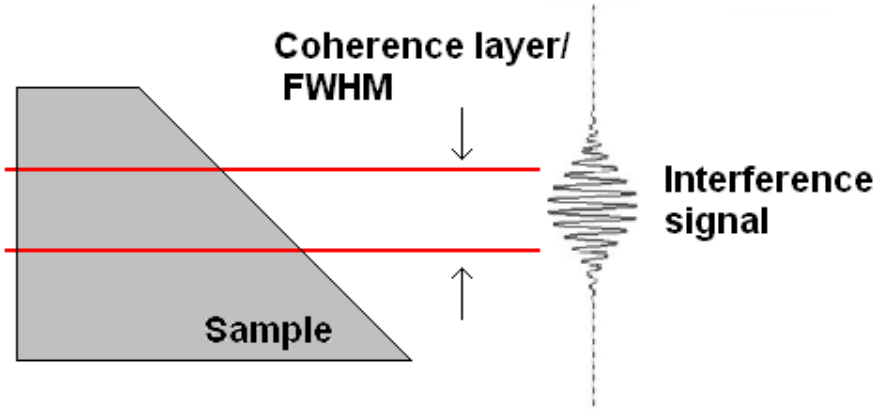

Figure 4.6: Displays the reflected interference signal in a low coherent interferometer. The coherence layer is marked with red lines.

As the reference mirror is movable, the reference mirror can be used to scan the coherence layer through the whole sample. If the coherence layer is placed above or below the sample, none of the reflected beams will interfere with the reference beam and only the background intensity $I_1 + I_2$ will be detected. Scanning the coherence layer through the sample will provide information about the surface. Figure 4.7 illustrates the coherence layer at a deeper position in the sample. Moving the coherence layer deeper into the sample is done by moving the reference mirror and hence the optical path difference is increased.

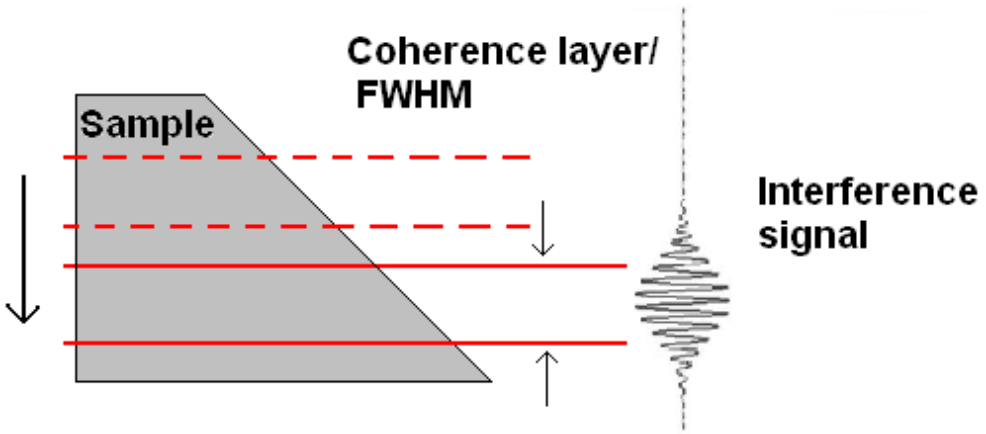

Figure 4.7: Illustrates the coherence layer at a deeper position than in figure 4.6. The interference signal is now detected only at the the deeper position and not from the initial position marked with the dottet red line.

The Michelson interferometer in figure 4.2 does not illuminate the whole sample.

Because the beam waist is so thin, it illuminates only a small part of the sample. To acquire a full image of the sample, introducing an additional mirror that scans the beam over the sample is a common solution [6]. Another technique is to insert a beam expander which collimates the source. Replacing the point detector with a CCD camera will introduce the possibility to capture an image of the whole sample in one instance. This can be realized with the setup in figure 4.8.

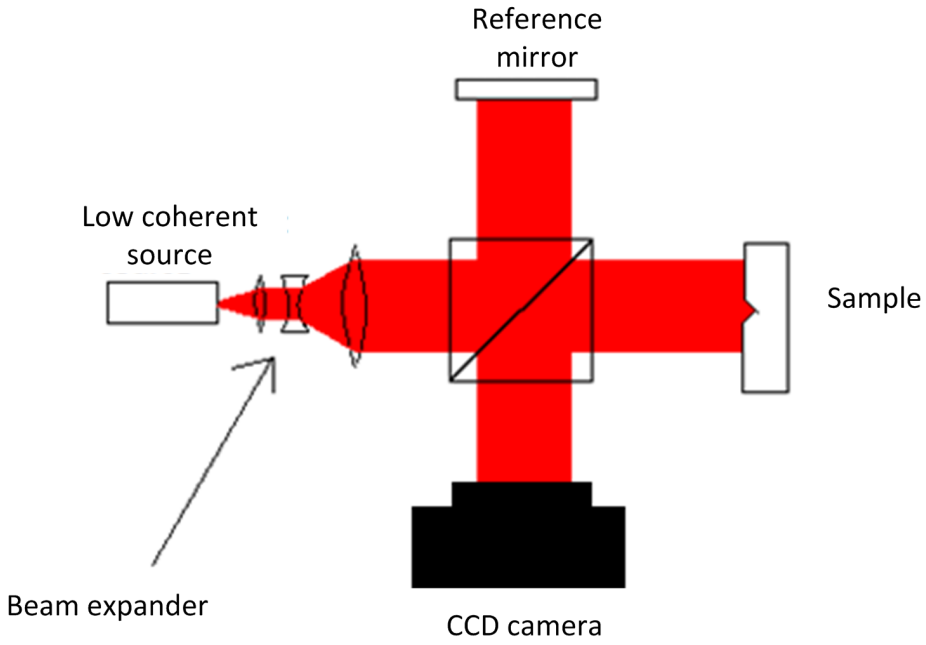

Figure 4.8: : A sketch of a low coherence interferometer setup that records a 2-D image in one instance.

Source

Depending on the type of measurement there are several requirements for the source in a low coherent interferometer. The different aspects of the source are examined part for part in this section.

The intensity of the source has to be high enough to utilize the dynamic range of the camera which can lead to optimized fringe contrast. LCI can be used to image the inner structure of a material and requires intensity high enough to penetrate the material and be reflected. This is obviously dependent on the material under investigation.

The Wavelength of the source is also of importance when imaging inside a material. Some materials are transparent above a certain wavelength. Silicon which is under investigation in this project is transparent for wavelengths in the range $1.25\mu m$ to approximately $6\mu m$.

Depending on the application, the source needs a large spectral width. A large spectral width equals a narrow coherence layer and provides enhanced axial resolution. Other applications require the spectral width to be of a certain width. For the beams to interfere at the detector, they must not only be temporally coherent, but also spatially coherent.

In a Michelson interferometer 50% of the light is reflected back towards the source. This is a problem as it can lead to mode hopping and as a result the fringe pattern will be unstable. A source with a built in isolator is desired to avoid this problem.

4.2 Resolution

The resolution of an optical system can be decided by the system's ability to separate two points from each other. This may be two spatially or axially separated points. Both spatial and axial resolution will in this chapter be examined. Imaging through a silicon lens will be done in this project, and calculation of resolution for this case is provided at the end of this chapter.

The theory in this chapter is based on the work done by Gastinger and Johnsen in [3] and further developed. Gastinger and Johnsen investigated the theoretical limits for resolution for the setup used in this project. A closer investigation of the calculations done in [3] will be provided in the following chapter.

4.2.1 Spatial resolution

The transverse resolution for optical microscopy is determined by the focusing properties of the optical beam. The systems' ability to focus an optical beam into a small spot size is inversely proportional to the transverse resolution. The spatial resolution can have several definitions. The one used here is given by [7]

$$\delta x = \frac{4\lambda_c}{\pi}\frac{1}{2NA}. \tag{4.18}$$

δx	Resolution
λ_c	Center wavelength
NA	Numerical aperture

The numerical aperture of a lens is decided by the refractive index of the medium and the half angle of the light cone as [8]

$$NA = n\sin(\alpha), \tag{4.19}$$

where n is the refractive index of the medium and α is the angle of rays that hits the lens. This means that a large cone of rays which contribute to the image will give a high numerical aperture. This is illustrated in figure 4.9.

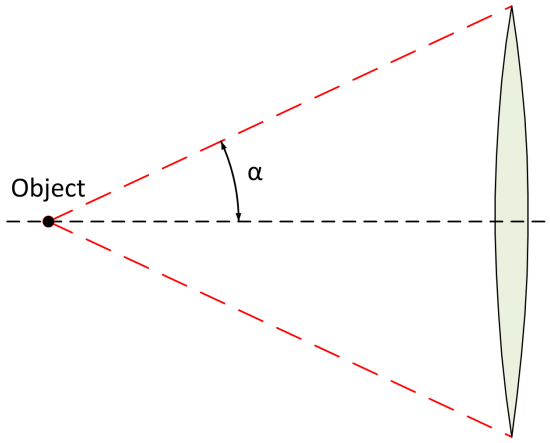

Figure 4.9: The illustration shows how the components contribute to the numerical aperture. The red lines are the outmost rays of light that hit the lens with an angle α.

When using the numerical aperture with the formula for spatial resolution, n and α have to be chosen with care. The numerical aperture in equation 4.18 can be treated as an effective numerical aperture of the whole imaging system. The starting point for the angle, refractive index and the wavelength is at the object of interest.

One possibility is to investigate how n, α and λ_c translate towards the detector. For plane surfaces the product $n\sin(\alpha)$ is constant and can easily be calculated.

This will provide the correct NA and center wavelength at the detector in 4.18. For non-plane surfaces this becomes more complicated.

Another possibility is to calculate the numerical aperture directly from the object. In this case the center wavelength inside the silicon, $\lambda_{Si} = \lambda_{c,air}/n_{Si}$, has to be used. As the wavelength inside silicon is already scaled with the refractive index, the numerical aperture is reduced to angular aperture, $sin(\alpha)$. This method can be easier to use if we are dealing with non-planar surfaces where Snell's law does not apply.

Immersion

Immersion is a method for improving the optical resolution in microscopy [9]. The specimen is often covered with glass, so the light cone from the specimen will be refracted at the air-glass interface as shown in figure 4.10. According to equation 4.18, the spatial resolution depends on the cone of rays forming the image. Thus the refraction in the glass-air surface is a limitation to the spatial resolution of the imaging system.

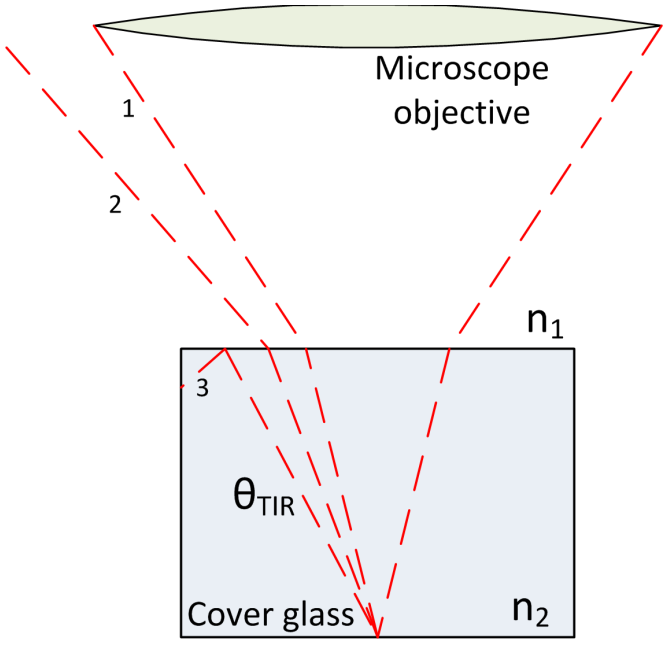

Figure 4.10: Microscope imaging of a specimen covered with a glass plate. n_1 is the refractive index of air, while n_2 is the refractive index of glass.

If we study ray 3 in figure 4.10 we see that it will experience total internal reflection at a certain angle. Ray 2 with slightly smaller angle will be strongly refracted at the glass/air interface and be bent away from the microscope objective. It is obvious that rays above a certain angle do not contribute to the imaging system.

The light cone that hits the lens will be reduced inside the cover glass. To increase the cone of rays that hit the lens, it is possible to fill the gap between the lens and the cover glass with an immersion liquid. If this liquid has a refractive index close to the refractive index of the cover glass, the light rays will not be refracted on their way to the lens. As a result, the cone of rays that contribute to the image become larger, as seen in figure 4.11. This can be seen as an increase in numerical aperture and thus an increase in spatial resolution.

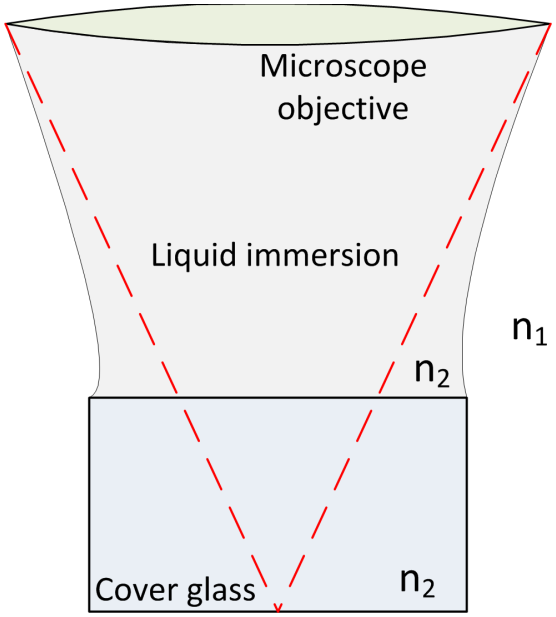

Figure 4.11: Microscope imaging of a specimen covered with glass. Liquid immersion between the lens and the glass plate is used to improve the numerical aperture. n_1 is the refractive index of air, n_2 the refractive index of glass and n_3 the refractive index of the liquid immersion. $n_2 \approx n_3$.

Solid immersion

The principle of immersion can be used in a different way. Instead of using immersion liquid between the lens and the glass plate, it is possible to form a lens on the glass plate. This is called solid immersion and was first developed by Mansfield and Kino [10]. The emerging rays from the object will in this case have normal incidence to the surface, as seen in figure 4.12. This means that the rays will not be refracted; only lose some intensity due to reflections.

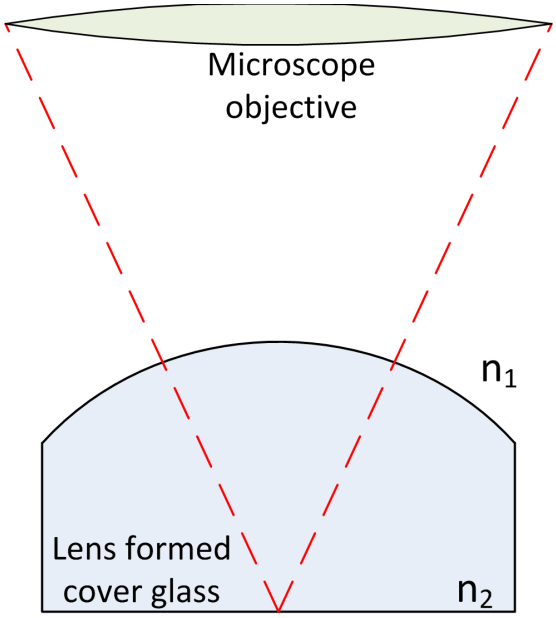

Figure 4.12: The figure illustrates the principle of solid immersion in microscopy. No refraction occurs at the silicon/air interface as the light beam has normal incidence.

In an ideal situation all light rays have normal incidence with respect to the surface. This is the case when the center thickness of the lens formed cover glass is equal to the radius of curvature of the convex part of the cover glass. In this situation it is possible to obtain the same increased numerical aperture as with immersion liquid.

4.2.2 Axial resolution

The axial resolution of an LSI system is determined by the coherence length of the source and the depth of focus of the imaging system. For systems with low numerical aperture the depth of focus exceeds the coherence length of the source. Thus the coherence length of the source decides the axial resolution. Several definitions can be used for the coherence length, a commonly used expression is [3]

$$\delta z \approx \frac{2ln2}{\pi}\frac{\lambda_c^2}{\delta\lambda}. \tag{4.20}$$

Here δ_c is the center wavelength and $\delta\lambda$ is the FWHM of the light source, and the inverse of the coherence length.

In the case where the depth of focus is shorter than the coherence length of the source, the interference signal will be blurred outside the depth of focus. Hence the depth of focus is a determining factor for the axial resolution. As the interference signal is detectable beyond the depth of focus, the criteria for focal length with respect to coherence time should be considered. This is an investigation beyond the scope of this project. The depth of focus is given by [3]

$$\delta z = \frac{\lambda}{\pi N A^2}. \tag{4.21}$$

When dealing with objects inside or behind plane surfaces the formula is straight forward. When non-planar surfaces are present one should consider the parameters at the object for easier calculations. The wavelength at the object and angular aperture instead of numerical aperture should be considered. The problem with non-planar surfaces is explained in greater detail under 4.2.1.

4.2.3 Example with a silicon lens

Gastinger and Johnsen presented in [3] an idea for improving the resolution when imaging inside silicon. The idea was to design a plano-convex silicon lens with focal point on the plane surface. Imaging the plane surface through the convex lens provides an improved resolution. A clear way of calculating the resolution will be demonstrated in the following example.

Spatial resolution

We consider a microscope objective with $NA = 0.4$ to image inside a silicon lens with refractive index equal to 3.51. A superluminescent diode with center wavelength of 1200nm and FWHW of 50nm is used. The objective lens can detect light which emerges from the focal point with an angle within 23.5°. We first consider the situation in figure 4.13(a) where the air-silicon interface is a plane surface. The microscope objective will only detect light within an angle of 6.54° emerging from the object as indicated in the figure.

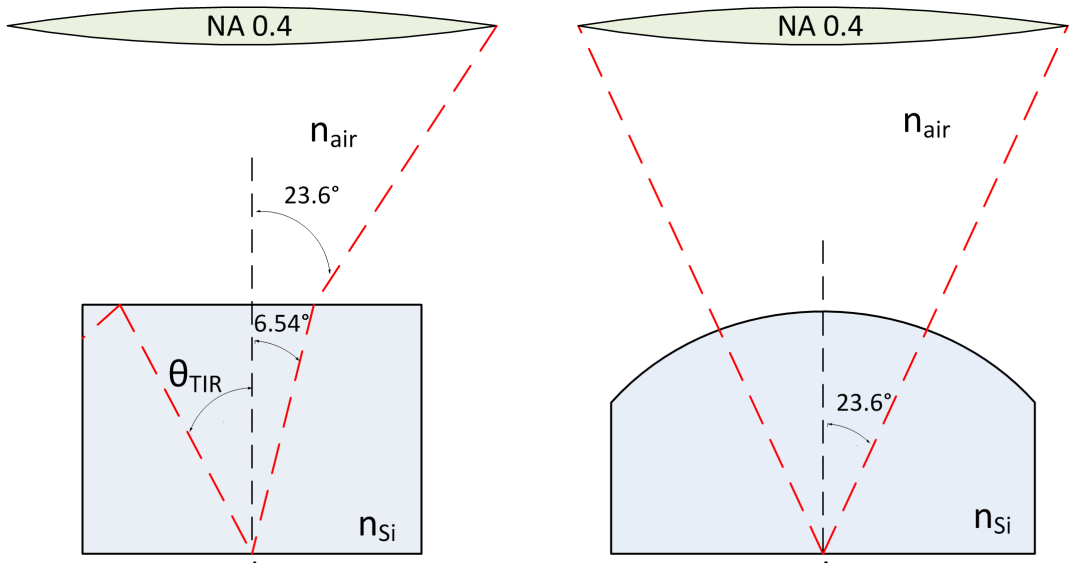

(a) Illustration of imaging inside a silicon block. Total internal reflecion(θ_{TIR}) occurs at 16.55°.

(b) Illustration of imaging inside a plano-convex silicon lens. Curvature and depth of the lens is designed so no refraction occur at the silicon/air interface.

Figure 4.13: Illustration of imaging in a silicon lens. With and without solid immersion.

As we are dealing with a plane surface Snell's law dictates that the numerical aperture is the same on both sides of the surface; $NA_{Si} = NA_{air} = 0.4$. Thus the resolution will be the same for imaging inside a plane surface of silicon, as in air. Equation 4.18 yields

$$\delta x_{air} = \delta x_{Si} = \frac{4\lambda_c}{\pi}\frac{1}{2NA} = \frac{4 * 1280nm}{\pi}\frac{1}{2 * 0.4} \approx 2\mu m. \tag{4.22}$$

In the case of solid immersion, figure 4.13(b), the detected cone of rays is expanded to 23.5° due to normal incidence on the silicon/air surface. The surface is no longer plane and Snell's law can not be used. Calculating the resolution directly from the object is a suitable approach. The center wavelength inside silicon is used and only sine of the angle is considered for numerical aperture.

$$\delta x_{Si,lens} = \frac{4\lambda_c}{n_{Si}\pi}\frac{1}{2sin(\alpha)} = \frac{4 * 1280nm}{3.51\pi}\frac{1}{2 * 0.4} \approx 0.6\mu m \tag{4.23}$$

This shows that the spatial resolution can be improved by a factor of n, equal to the refractive index, with solid immersion.

Axial resolution

To decide the axial resolution of the system the depth of focus and coherence length have to be considered. The coherence length is calculated according to equation 4.20. The wavelength is scaled inside silicon.

$$\delta z \approx \frac{2ln2}{\pi}\frac{\lambda_c^2}{n_{Si}\delta\lambda} \approx \frac{2ln2}{\pi}\frac{1280nm^2}{3.51 * 50nm} \approx 4.1\mu m. \tag{4.24}$$

The case with a plane surface for depth of focus is first considered. Using angular aperture and the scaled wavelength inside silicon together with equation 4.21 yields

$$\delta z = \frac{\lambda}{n_{Si}\pi NA^2} = \frac{1280nm}{3.51\pi sin(6.54^\circ)^2} \approx 9\mu m. \tag{4.25}$$

Using the same approach to calculate the depth of focus for a silicon lens yields

$$\delta z = \frac{\lambda}{n_{Si}\pi NA^2} = \frac{1280nm}{3.51\pi 0.4^2} \approx 0.7\mu m. \tag{4.26}$$

This results in a focal length shorter than the coherence length of the system.

4.2.4 Aberration

Several kinds of aberrations can be present in an optical system. These can be separated by chromatic aberrations and monochromatic aberrations [8]. Chromatic aberrations occur because the wavelength is dependent on the refractive index. Considering an illumination source with a spectral width of 34nm chromatic aberrations are present to some degree, but as this is effect minor the details of this will be disregarded in this report.

The monochromatic aberrations deteriorate the image and can be astigmatism, coma or spherical aberration. The latter one is due to the fact that the paraxial approximation is not valid for imaging through spherical surfaces at large angles. The marginal rays with large angles will be bent more or less (depends if converging or diverging lens) than the paraxial rays and as a result the focal spot will

be stretched out. This effect is not only present when using spherical surfaces, but imaging through cover glass or a cubical beamsplitter will also induce this phenomenon. A plane surface will produce the same effect act as a diverging lens, marginal rays are focused behind the paraxial rays, and the spherical aberration is said to be negative.

Even though spherical aberration is mainly an effect observed with spherical surfaces, the result of this phenomenon is the same through plane surfaces and the effect will in this report thus be referred to as negative spherical aberration [11]. The case where a microscope objective with NA of 0.4 is imaging backscattered rays through a 15mm glass beamsplitter is presented in 4.14.

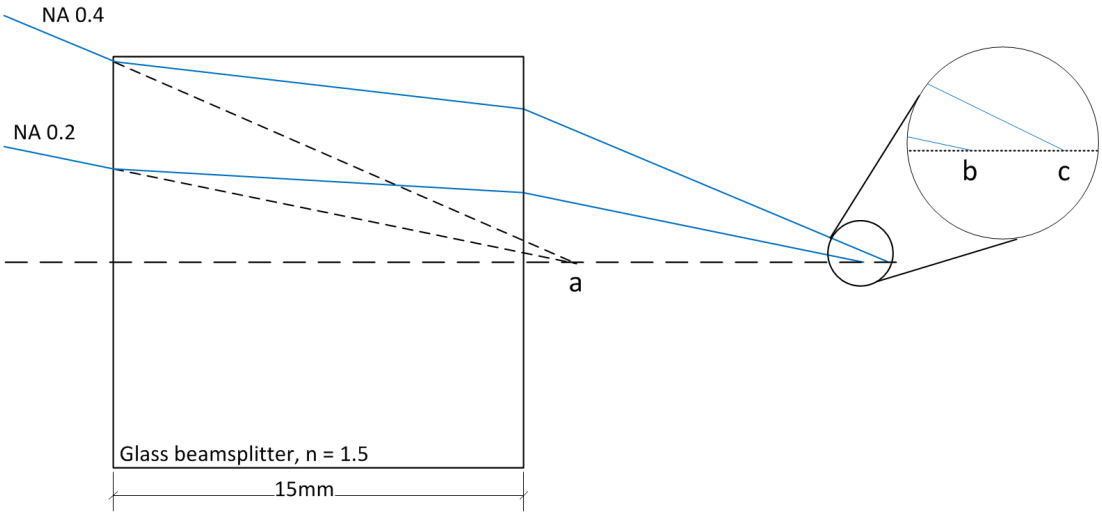

Figure 4.14: The figure illustrates how rays at different angles are focused at different positions. This is known as negative spherical aberration.

Two ray paths are illustrated in figure 4.14. These two ray paths represent the marginal rays of microscope objectives with numerical aperture of 0.2 and 0.4. The marginal ray that represents the NA 0.2 objective has its focal plane at point b, far behind the paraxial focal plane a. Inspecting the marginal ray that belongs to the NA 0.4 objective, it is seen that this focal plane is even further behind the NA 0.2 focal plane. This shows that the negative spherical aberration increases as the numerical aperture increases. The size and refractive index of the beamsplitter also has a large influence on the spherical aberration.

4.3 Phase

4.3.1 Phase-stepping

Calculation of the phase can in several optical measurement techniques improve the accuracy. In interferometry it is possible to calculate the phase by performing phase stepping. It is common to have a reference beam which the reflected beam from the sample is compared to. The optical path length in the reference arm is changed in small fractions over a distance corresponding to a whole wavelength. This can be done by moving the reference mirror small steps in the beam direction, and is often accomplished by the use of a piezoelectric actuator, hereby referred to as a piezo [12].

With the use of a digital camera the intensity in each pixel is recorded. Thus the camera will record, in each pixel, a series of measurements over one cycle of a sinusoidal intensity variation. A variety of different calculations depending on the number of samples taken will provide the phase [13].

At least 3 measurements have to be made to calculate the phase. A method for calculating the phase using N + 1 steps is here provided. The derivations in this section follow Creaths approach to phase-stepping [14]. If we consider an interferometer with a digital detector, the fringe pattern can be expressed as

$$I(x,y) = a(x,y) + b(x,y)\cos[\phi(x,y)]. \tag{4.27}$$

$a(x,y)$	Background intensity
$b(x,y)$	Fringe contrast
$\phi(x,y)$	Phase

Acquiring N + 1 images over a full wavelength results in a phase change between each image equal to $\phi_s = 2\pi/(N+1)$. The intensity in each pixel is given by

$$\begin{aligned} I_n(x,y) &= a(x,y) + b(x,y)\cos[\phi(x,y) + n\phi_s] \\ &= I_0(x,y)[1 + \gamma(x,y)(\cos(\phi(x,y))cos(n\phi_s) \\ &\quad -sin(\phi(x,y))sin(n\phi_s))]. \end{aligned} \tag{4.28}$$

$I_o(x,y)$	=	a(x,y)
$\gamma(x,y)$	=	a(x,y)/b(x,y)
n	=	0,1,...,N

These acquired images are multiplied by the corresponding factor $cos(n\phi_s)$ and summed over n. The use of the orthogonality of the trigonometric functions

provide equation 4.29 which is a part of the argument needed in the phase calculation.

$$\begin{aligned}\beta(x,y) &= 2\sum_{n=0}^{N} I_n(x,y)\cos(2\pi n/N) \\ &= NI_0(x,y)\gamma(x,y)\cos[\phi(x,y)] \end{aligned} \tag{4.29}$$

By the use of the same procedure, but multiplying with the factor $sin(n\phi)$, we find the other part of the phase argument.

$$\begin{aligned}\alpha(x,y) &= 2\sum_{n=0}^{N} I_n(x,y)\sin(2\pi n/N) \\ &= -NI_0(x,y)\gamma(x,y)\sin[\phi(x,y)] \end{aligned} \tag{4.30}$$

The phase for each pixel can be calculated with

$$\phi(x,y) = \arctan[-\alpha(x,y)/\beta(x,y)]. \tag{4.31}$$

For a phase step procedure consisting of four images(N=3) the step interval is $\pi/2$. With 4 pictures taken, equation 4.29 and 4.30 reduce to $\alpha(x,y) = B_3 - B_1$ and $\beta(x,y) = B_0 - B_2$, respectively. Entering this into equation 4.31 provides a four step algorithm for calculating the phase,

$$\phi(x,y) = \arctan(\frac{B_3 - B_1}{B_0 - B_2}). \tag{4.32}$$

When such a phase map is recorded the optical path difference,OPD, of each detector point can be reconstructed by [15]

$$OPD = \frac{\lambda}{2\pi}\phi(x,y). \tag{4.33}$$

If the optical path difference exceeds the range corresponding to 2π, unwrapping algorithms have to be applied. Unwrapping will remove the 2π periodicity and calculate the actual optical path difference.

4.3.2 Fresnels equations

In this section the behavior of a plane wave incident at a planar boundary between two dielectric media will be treated. The reflection and transmission coefficients are described by the Fresnel equations. From these equations the phase shift at internal reflection can also be deducted. The reflection and transmission coefficients for TE and TM polarization are [4]

$$r_x = \frac{n_1 cos(\Theta_1) - n_2 cos(\Theta_2)}{n_1 cos(\Theta_1) + n_2 cos(\Theta_2)}, t_x = 1 + r_x \tag{4.34}$$

$$r_y = \frac{n_1 sec(\Theta_1) - n_2 sec(\Theta_2)}{n_1 sec(\Theta_1) + n_2 sec(\Theta_2)}, t_y = (1 - r_y)\frac{cos(\Theta_1)}{cos(\Theta_2)}. \tag{4.35}$$

Here n_1 and n_2 represent the refractive indices of the two media while Θ_1 and Θ_2 are the incoming and transmission angles. r_x represents TE polarization while r_y represents TM polarization. The graph corresponding to the r_x and r_y reflection coefficients are shown at the bottom of figures 4.15(a) and 4.15(b), respectively. For normal incidence the Fresnel´s reflection coefficients reduce to

$$r_x = r_y = (n_1 - n_2)/(n_1 + n_2). \tag{4.36}$$

Squaring equation 4.36 gives the power reflection, $r_x^2 = R$. Consider the case in section 4.2.3 where the inside of a plano-convex silicon lens is imaged. For this boundary between silicon and air, $n_1 = 1$ and $n_2 = 3.5$. Light with a normal incidence to the plane silicon-air surface of the silicon lens will have a power reflectance of $R = r_x^2 = 0.28$ meaning a 28% of the light is reflected. For increasing angle the power reflectance will increase and become unity, meaning total internal reflection, at the critical angle $\Theta_c = sin^{-1}(n_2/n_1) = 16.6°$.

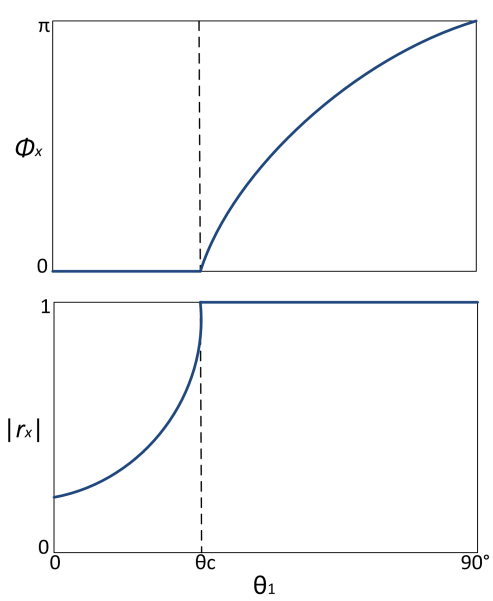

(a) Phase and reflection coefficient for TE polarization. Critical angle at 16.6°.

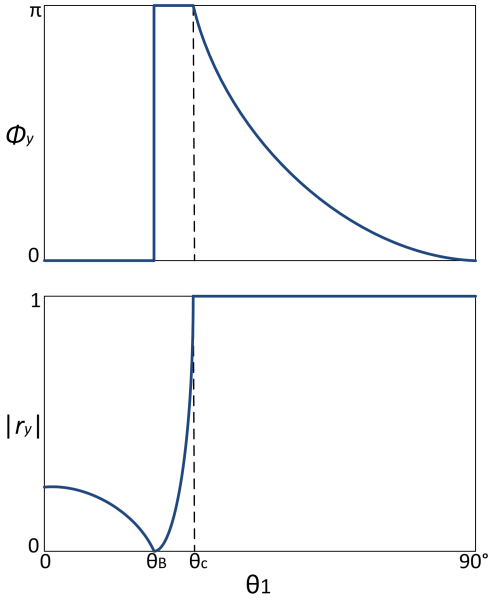

(b) Phase and reflection coefficient for TM polarization. Brewster angle at 16° and critical angle at 16.6°.

Figure 4.15: Magnitude and phase reflection coefficient as a function of angle for TM (a) and TE (b) polarized light for internal reflection. θ_1 is the angle of the incident light beam. The figures are adapted from Saleh and Teich [4].

The phase shift is different for TM and TE polarization. The phase shift at normal incidence is zero for both TE and TM polarization. The TE phase shift is zero until the incident angle reaches the critical angle, Θ_c. It then starts to increase and ends up at π at 90°. The TM phase shift jumps to π between the Brewster angle $tan(n_1/n_2) = 16°$ and the critical angle. From the critical angle to 90° it decays.

4.4 Newton fringes

The basic theory in this chapter follow the derivation from Malacara [16]. The phenomena of Newton rings can be observed when illuminating two surfaces which are in contact or close to contact. The reflections of light from the two surfaces interfere and are most easily observed if the illumination source is monochromatic. A monochromatic light source is not necessary to observe Newton fringes, but with the long coherence length of monochromatic light the two surfaces can

be relatively far apart and still produce an interference pattern.

To create Newton fringes a plane surface and an oblique surface may be used. Consider the situation in figure 4.16 where the oblique structure is placed just below the plane surface. A light beam emerges from the source and is reflected down towards the plane surface by the beamsplitter. The beam enters the plane surface and only has a small reflecion component at the top as this surface is anti-reflection coated. The lower part of this plane surface is not anti-reflection coated and will reflect parts of the beam toward the detector. The other part will be both transmitted and reflected at the oblique surface. These to reflected waves will then interfere and create an interference pattern at the detector.

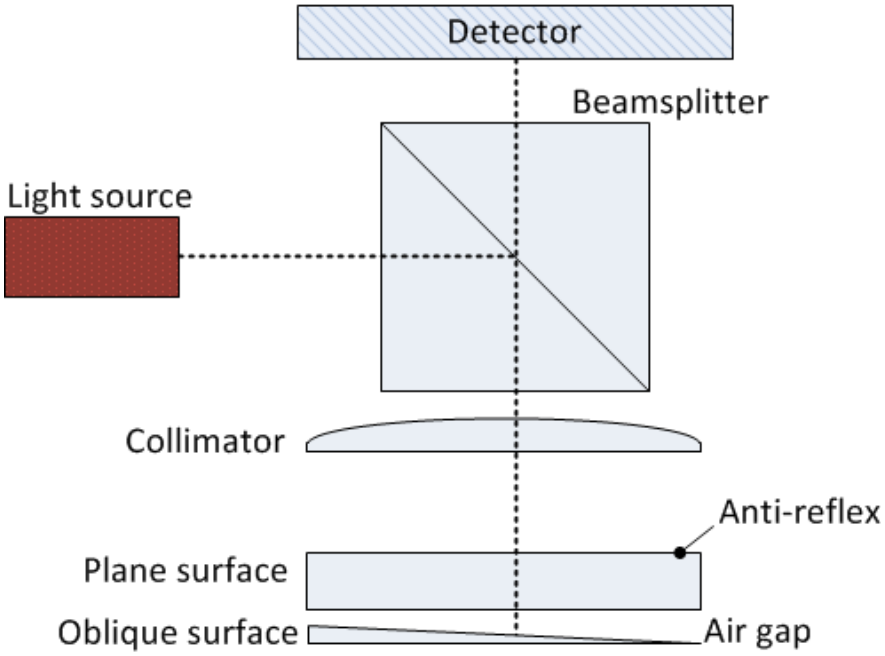

Figure 4.16: Optical setup where Newton fringes can be observed. Destructive and constructive interference occur due to the different optical path length of each ray in the air gap. The figure is adapted from Malacara [16].

Investigating what happens at the air gap between the two surfaces will reveal how the Newton fringes occur. In figure 4.17 incoming rays which interfere destructively different positions are illustrated. All these rays are internally reflected at the plane surface and reflected from the top of the oblique surface. Each of the illustrated rays has a different optical path length (ODL) which is approximately equal to two times the size of the air gap at the specific position.

Note, figures 4.16 and 4.17 are simplified. The reflected beam from the oblique surface will be a bit displaced as it has an incident angle and hence an reflection angle with respect to the normal of the oblique surface. The optical path length due to the air gap will therefore be longer than two times the size of the air gap depending on the angle of the oblique surface.

If the oblique surface is a dielectric, it will also pick up a phase change of π when it is reflected. Due to this, destructive interference (dark fringes) occurs when the phase difference between the two beams is an integer multiple of wavelength. The phase difference between the two reflected beams thus decides the intensity on the detector.

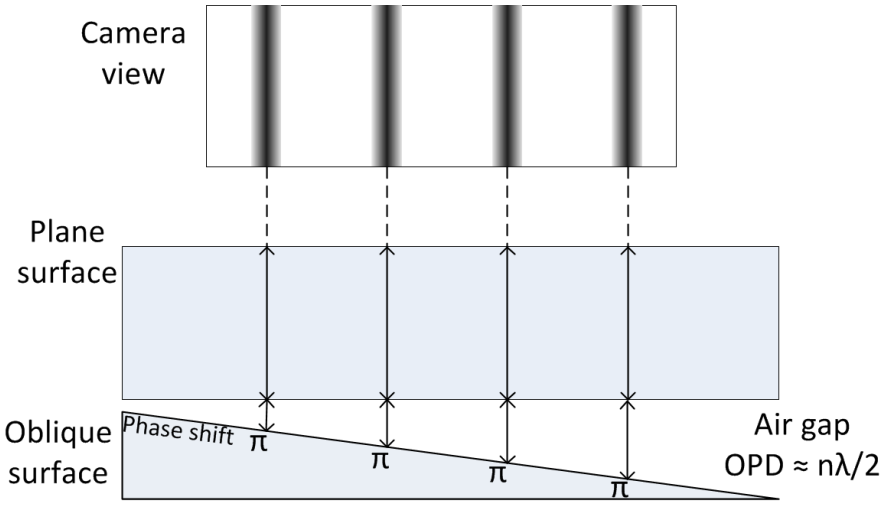

Figure 4.17: Detailed illustration of how the optical path difference and phase shift produce dark fringes. The optical path length in the air gap varies as a function of positions. The figure is adapted from Malacara [16].

The fringes are in this case straight lines with equal spacing between the fringes. Switching the oblique surface with a convex surface will produce circular fringes (Newton rings). The structure of the Newton fringes and the spacing between them can provide detailed information about the item under investigation.

4.5 Electron Backscatter Diffraction

When investigating the sawing process described in section 4.6 the direction of the crystal lattice of the silicon is of importance. A technique to find the crystal direction is thus needed. Electron backscatter diffraction (EBSD) [17] is such a

technique and will here be briefly reviewed.

A scanning electron microscope (SEM) equipped with a phosphor screen is used as a tool. A stationary electron beam strikes a tilted sample and interacts with the atoms, a process which creates backscattered electrons. The sample is tilted 70° to enhance the proportion of backscattered electrons that undergo diffraction and is backscattered to the phosphor screen. These diffracted electrons form a pattern on the phosphor screen which is dependent on the crystallographic structure of the sample. Such a pattern consists of several bands which is called Kikuchi bands. When several Kikuchi bands are present, the width of the bands relate to the interplanar spacing, d_{hkl} and obey Braggs law [18],

$$2d_{hkl}sin(\Theta_{hkl}) = n\lambda. \tag{4.37}$$

Here d_{hkl} represents the distance between the diffraction planes, Θ_{hkl} is the Bragg angle, n the refraction order and λ the wavelength of the incident electron beam.

These bands are interpreted by a computer which can provide information about the direction of the crystal lattice. A Kikuchi band which is read by a computer is shown in figure 4.18. The computer analyzes the bands and calculates how the crystal planes in the sample are aligned. This is represented by a pole figure, shown in figure 4.18. Here we can see that the <001> directions are aligned with the transverse (TD) and rolling (RD) direction.

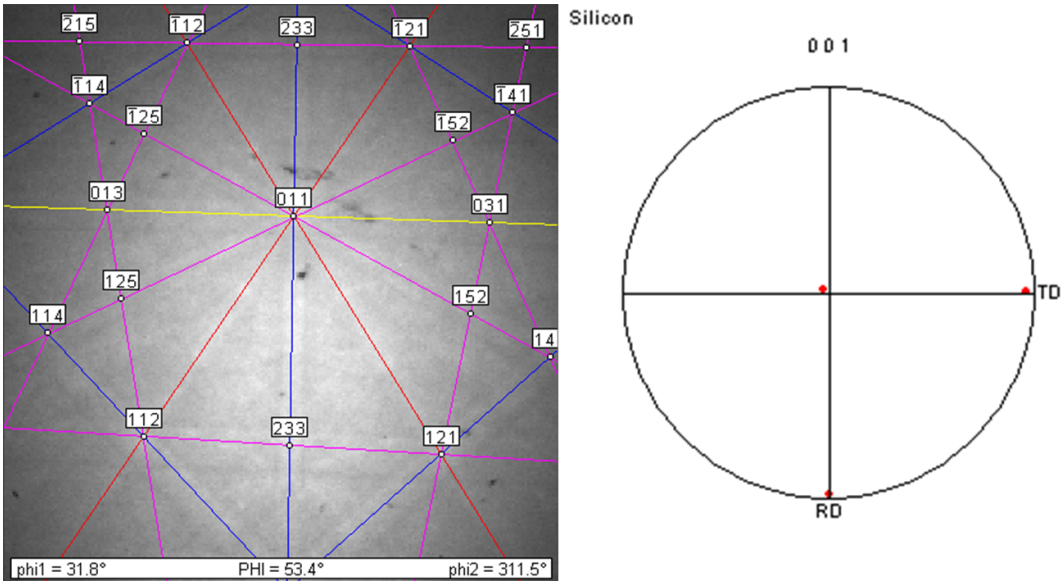

Figure 4.18: Kikuchi bands marked with colors and read by a computer (left) with corresponding pole figure(right). The red dots in the pole figure represents the <100> directions.

4.6 Wafer sawing

The material mainly used for producing solar cells is silicon. Large blocks of silicon are cut into wafers which are further treated and ready for solar cell manufacturing. The theory in this chapter is based on Möllers paper on Multicrystalline silicon for solar cells [1].

The process of cutting blocks of silicon into wafers is today mainly done by multi-wire sawing. Multi-wire sawing can be accomplished by using a stainless steel wire which is led through a number of wire guides. This forms a net of wires which consists of 500 to 1000 parallel wires. The wire is pulled through the system with a speed between 5 to 20 m/s. The sawing process is illustrated in figure 4.19.

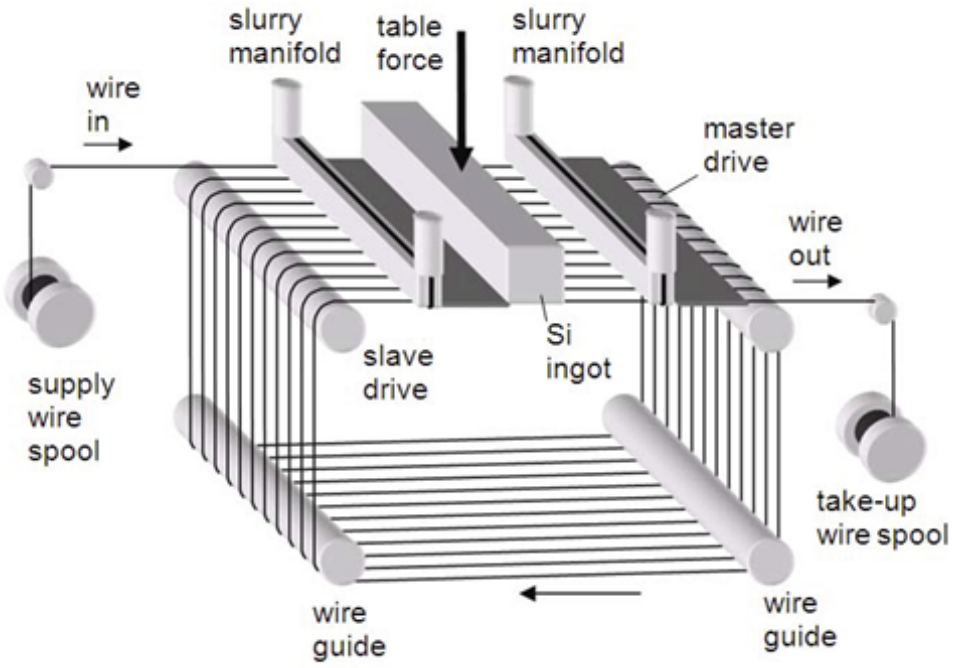

Figure 4.19: Multi-wire sawing process. A steel wire forms a net which carries slurry around the silicon ingot. [reprint from K. Gastinger and L. Johnsen [3]]

The space between the silicon block and the sawing wire is filled with slurry. The slurry consists of Polyethylene Glycol(PEG) as carrier and Silicon Carbide(SiC) working as abrasive particles. A cross section of the sawing channel is illustrated in figure 4.20. When the particles are pressed against the silicon by the wire, there will be pressure on the largest particles that are in contact with the wire and the silicon. This pressure will be largest just below the wire, and decreases

toward the side. It is the sides on the sawing channel that will become the surface of the wafer, and thus decide the quality of the wafer.

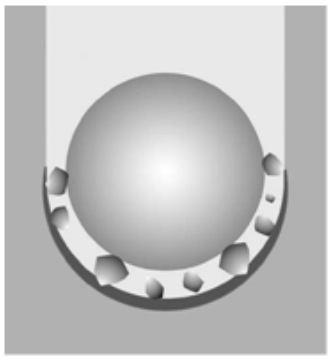

Figure 4.20: Schematic cross section of the sawing channel. Sharp silicon carbide particles are pressed against the silicon by the steel wire.

As the wire moves along the sawing channel in the silicon, the sharp SiC particles start to roll. When the sharp part of the SiC particles get pressed against the silicon by the wire, high pressure can occur on a small part of the silicon. This can be seen as small indents, and small chips of silicon will fall off as the wire moves. When a part of the silicon is chipped away, small cracks can occur underneath the chipped area. An illustration of an indent which results in chipping is shown in figure 4.21. The small cracks underneath the chipping area decreases the wafers tensile strength.

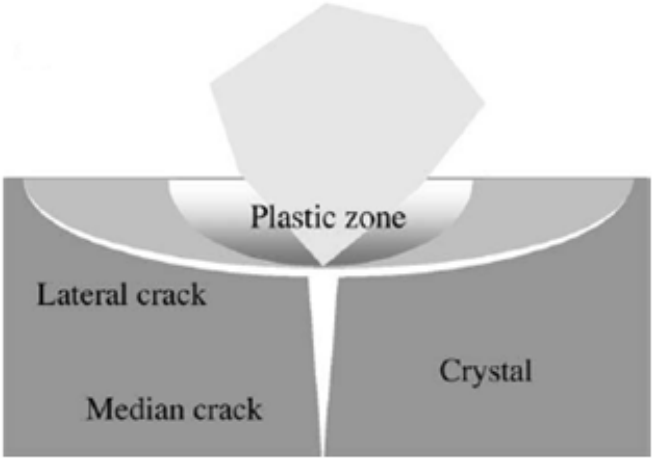

Figure 4.21: Illustration of microcrack underneath a chip. The silicon carbide particle produces an indentation in the silicon material.

4.7 Analog to Digital

Most signals are analog. To process the analog signal by digital means, the analog signal must be converted into digital form. This is done by taking samples of the analog signal with a specific frequency. The theory in this chapter follows Proakis and Manolakis [19] and covers periodic sampling. The relationship between the analog and digital signal is described by

$$x(n) = x_a(nT), \ -\infty < n < \infty, \tag{4.38}$$

where n is an integer and T is the sampling period. The discrete time signal $x(n)$ in 4.38 is produced by taking samples of the analog signal $x_a(t)$ with a period of T. The sampling rate is thus $F_s = 1/T$. The connection between t, n, T and F_s is

$$t = nT = \frac{n}{F_s}. \tag{4.39}$$

In equation 4.39 t os the time dependency of the analog signal, and F_s is the sampling frequency. There exists a relationship between the analog and the descrete frequency. This can be shown by sampling the simple analog signal

$$x_a(t) = Acos(2\pi Ft + \Theta) \tag{4.40}$$

where F is the analog frequency and θ is the phase of the analog signal. When sampled with a frequency F_s the signal in equation 4.40 yield

$$\begin{aligned} x_a(nT) = x(n) &= Acos(2\pi FnT + \Theta) \\ &= Acos(\frac{2\pi Fn}{F_s} + \Theta) \\ &= Acos(2\pi fn + \Theta) \end{aligned} \tag{4.41}$$

where the discrete frequency thus is $f = F/F_S$. It can be shown that $-1/2 < f < 1/2$. When $f = 1/2$ and the sample rate is F_s it follows that the the maximum value for F is

$$F_{max} = \frac{F_s}{2}. \tag{4.42}$$

The maximum frequency that can be uniquely distinguished when a signal is sampled with a frequency F_s is thus $F_{max} = F_s/2$. This frequency is called the Nyquist frequency or the folding frequency. This means that the signal in equation 4.40 can be perfectly identified if $F < F_s/2$.

To investigate what happens when the frequency is higher than F_s, consider the same signal as in equation 4.40 but with the frequency $F_k = F + KF_s$. K is here an integer. The discrete signal now yield

$$\begin{aligned} x(n) &= A cos(2\pi \frac{F + KF_s}{Fs} n + \Theta) \\ &= A cos(2\pi n \frac{F}{F_s} + 2\pi K n + \Theta) \\ &= A cos(2\pi n f + \Theta). \end{aligned} \tag{4.43}$$

This signal is identical to the sampled signal in 4.40 which had another frequency. The frequencies F_K are called aliases of the lower frequency F.

This can also be seen by examining the frequency spectrum of the sampled signal. Figure 4.22 shows the frequency spectra of a sampled signal. The frequency spectra will be repeated for every nF_s where n is an integer, indicated with the green spectrum. The red spectrum in figure 4.22 is the original spectrum.

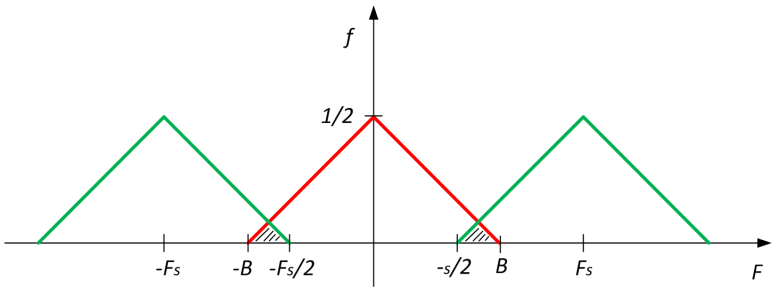

Figure 4.22: Illustration of how a sampled signal. The original signal will be repeated at every nF_s. Overlapping of the frequency spectra creates a spectrum unlike the original.

In figure 4.22 the sampling frequency is not twice the highest frequency component of the original signal, and the sampled signal will hence be altered. Frequencies above half the sampling frequency will be folded about the folding/Nyquist frequency back into lower frequencies. This mean that all the frequency components from the original signal with a frequency $> F_s/2$ will have an alias frequency below $F_s/2$.

5 Experimental setup

This chapter will describe the optical and electrical setup. The setup was first built in fall 2010 as a part of my project assignment. The setup used in this master thesis is slightly redesigned to be used with other equipment and some mechanical parts are updated. Several updates to the program which controls the components have been done. This mainly includes automation, user interface and better piezo control. The programming will be shown with flowcharts for easier understanding.

5.1 Optical setup

An early model of the interferometer system used in this project was built by Gastinger and Johnsen and presented in [3]. The setup built by Gastinger and Johnsen provide a proof-of-principle and schematics for the interferometer configuration used in this project.

The optical setup is based on a Michelson interferometer, the main theory is described in chapter 4.1.1. An interference based approach is chosen due to its ability to detect microscopic changes in a material. A large variety of components can be chosen for a Michelson interferometer. Depending on the application the different components have to be chosen with care. The main components used for this project were suggested by Gastinger and Johnsen in [3]. The requirements and specifications for the components will be presented in 5.1.2.

5.1.1 Interferometer configuration

The chosen basis for the interferometer is a 30mm cage system from Thorlabs [20]. Selecting components small enough to fit within the cage system provides the opportunity to attach everything with rods which is connected to the cage. Every component is directly connectrf to each other, contrary to when the components just are connected via the table. This offers a stable environment as the source, reference mirror, object and detector are directly connected through the rods.

An illustration of the cage system with the microscope objective, source and the reference and objective lenses in each side of the cage is shown in figure 5.1. In addition to improved stability the rods make the alignment of the components, with respect to each other, easier.

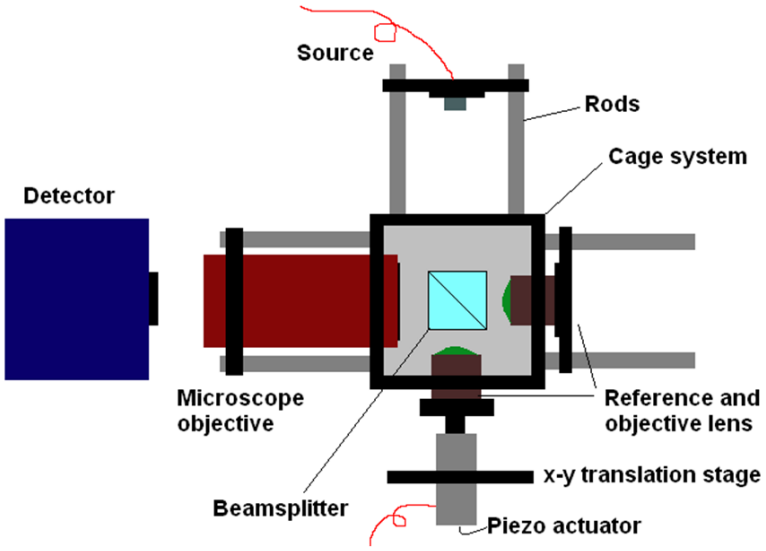

Figure 5.1: Illustration of the cage system connecting the components of the interferometer.

A photograph of the components inside the cage system is shown in figure 5.2. The holder for the reference lens is custom made to fit with the piezo actuator. The sample lens holder is manufactured to provide as large as possible surface area on the plane backside of the silicon lens. This was done so a TRIBOCOR tribometer could access the lens and make in-vivo scratch tests.

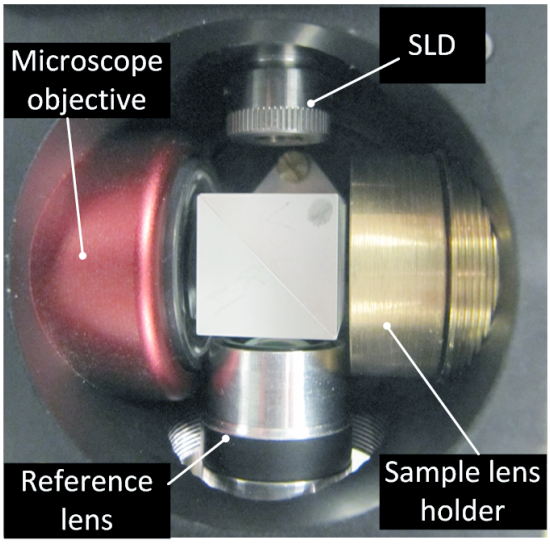

Figure 5.2: Photograph of the components inside the cage system. Two identical silicon lenses are used, one for indentation and one as a reference.

The scratch test in the tribometer is not a part of this project, but parts of the

setup are designed to fit with the tribometer. This includes a mirror at 45° to create a 90° bend. An illustration of the whole setup is shown in figure 5.3

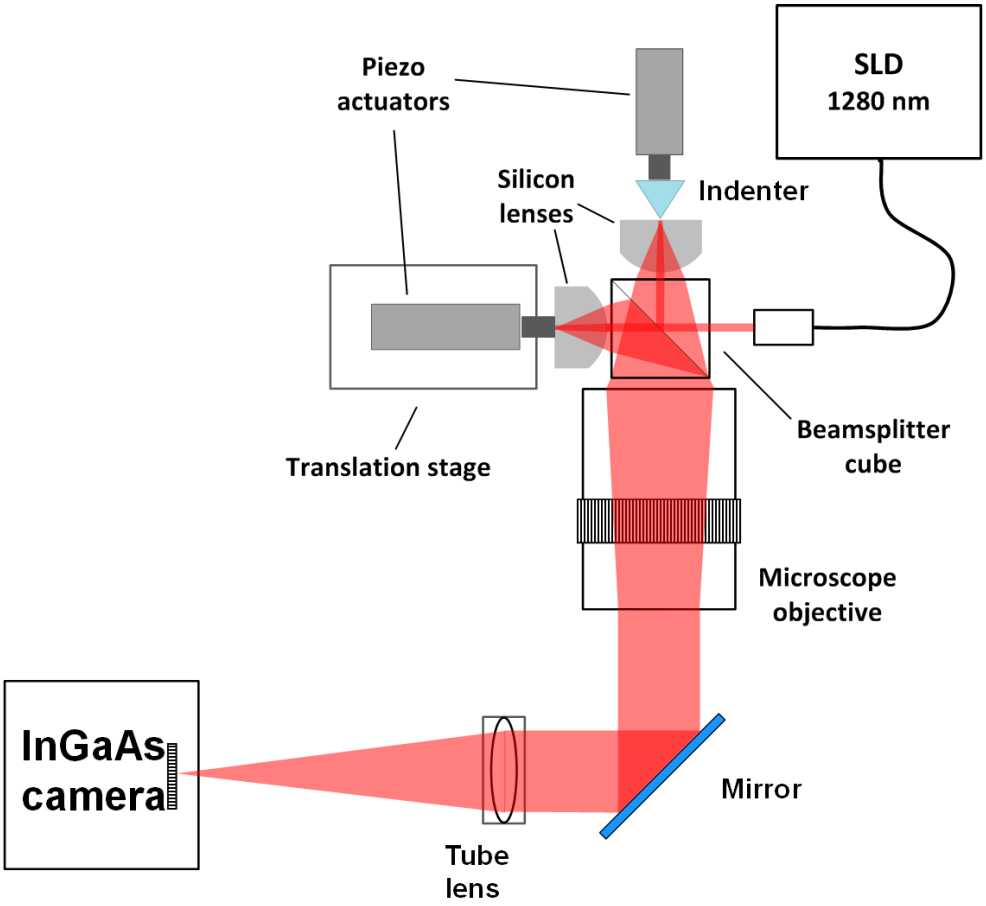

Figure 5.3: Illustration of the optical setup. The light beam from the SLD is split by the beamsplitter and reflected at the back side of the silicon lenses. The reflections interfere and this pattern is imaged through the microscope objective. Phase maps may be obtained by stepping the reference piezo. Figure made by Lars Johnsen.

When building such a setup there are several challenges to overcome. The mechanical workshop at NTNU was frequently used for adapting special parts to the commercial equipment at the lab. The parts which were crafted in fall 2010 and still are used in the setup are: an adapter for fitting the piezoelectric actuator to the translation stage, a pillar for placing the beamsplitter at the correct height and position and an adapter for fitting the indenter to a piezoelectric actuator. Schematic diagrams of these three parts are found in appendix A.2. An updated lens holder to fit with the magnetic head of the piezoelectric actuator has been crafted for this project, together with a sample holder for the silicon lens.

A photograph of the whole setup used for indentation is shown in figure 5.4

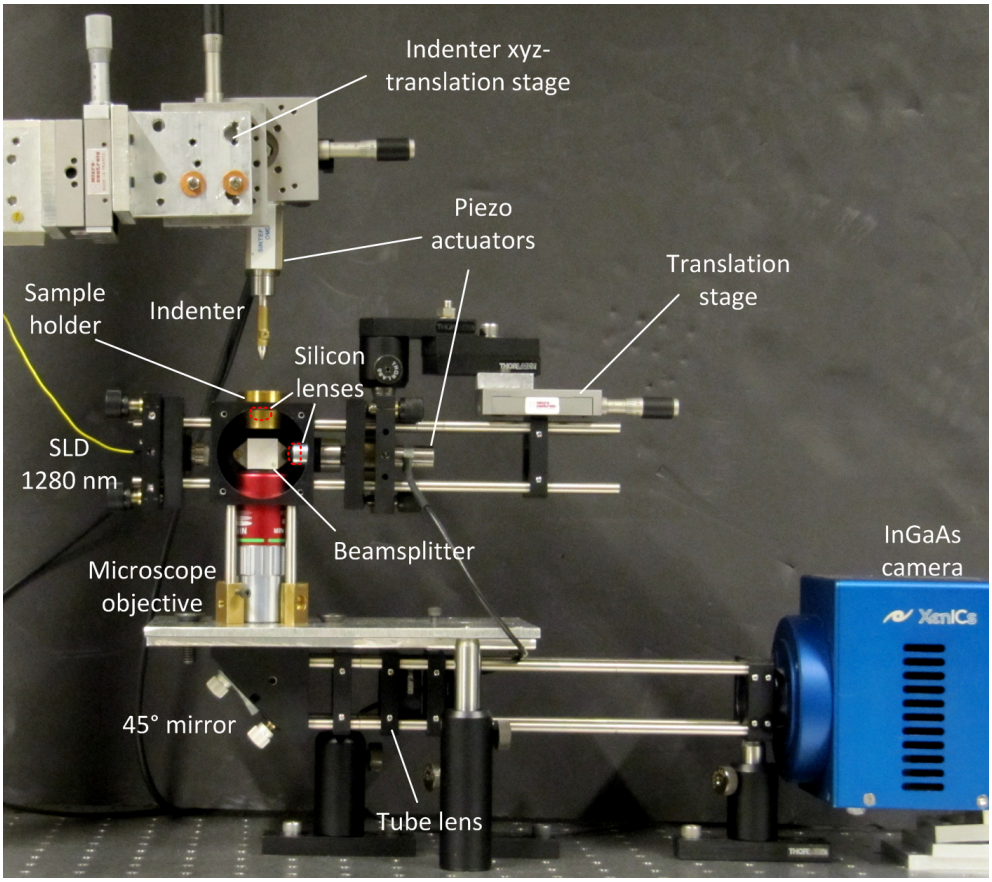

Figure 5.4: Photo of the optical setup used for indentation and phase map recordings.

For some resolution measurements a simplified setup was as seen in figure 5.5. The tube lens was not in the setup at all times, as the effect of this lens was to be measured.

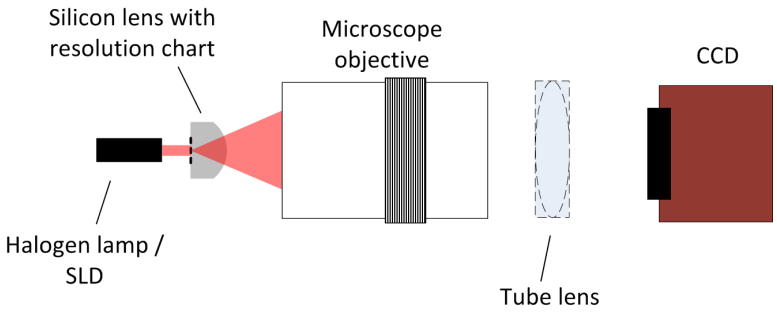

Figure 5.5: Illustration of the optical setup used in some resolution measurements.

5.1.2 Components

The different components for the LCI system will in this chapter be accounted for. The criteria each component have to fulfill will be evaluated, followed by the specification of the component.

Source

The criteria for the light source are discussed in detail in chapter 4.1.3. The most critical aspects to consider are the following:

- The spectral width of the source determines the coherence layer of the system. This is of importance when phase-stepping is used for recording a phase map of a deformation. When investigating a deformation the coherence layer should be wide enough to cover the whole profile depth of the deformation.
  On the other hand, using the LCI system for investigating the topography after deformation requires a thin coherence layer for high axial resolution.

- To obtain interference the source has to be spatially coherent.

- The light has to penetrate silicon, thus have a wavelength between $1.25\mu m$ and approximately $6\mu m$.

- Have sufficient intensity. The signal will be weakened on its round trip inside the silicon lenses due to attuenuation, scattering and reflections.

As high intensity, broadband and near-infrared wavelength are required, a superluminescent diode is used. The specific model is S1300-G-I-20 from Superlum [21]. SLDs are available with different characteristics, the one used in this setup has the intensity-wavelength relation shown in figure 5.6.

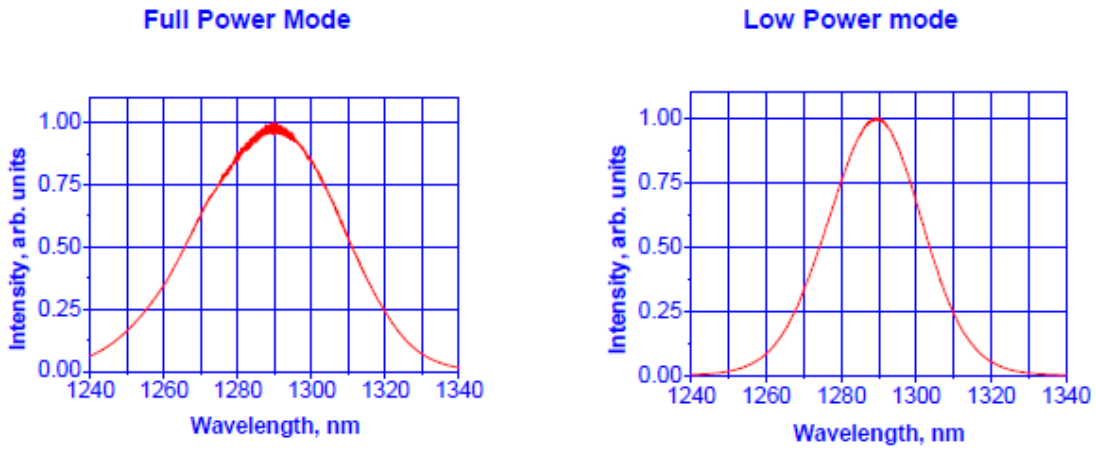

Figure 5.6: Intensity-wavelength characteristics of the two available modes on the SLD

From figure 5.6 it is seen that the SLD provides a broad spectrum which lies higher than 1250nm wavelength. The SLD can be used with low power or full power mode where the low power mode provides enough intensity to image inside silicon. The option for high power mode is useful for applications where low integration time on the camera is needed. Figure 5.6 also reveal different FWHM for the two modes. FWHM for the full power mode is 45nm and 30nm for the low power mode. If the dimensions of the deformation are critical, the low power mode is beneficial due to its broader band.
As discussed under section 4.1.3 the Michelson interferometer reflects 50% of the power back to the source. To avoid problems associated with the backreflection from the interferometer, the SLD has a built in isolator. The full datasheet for the superluminescent diode is provided in appendix A.3

Camera

The interferometer is built with the purpose of measuring inside silicon, which means that the camera has to be sensitive to wavelengths above 1250nm. The deformation we want to measure occurs very quickly. Thus a camera with high framerate is desired.
The CCD should have a low pixel pitch. The pixel pitch is the length between the center of one detector to another on the CCD. The interferometer is used together with a microscope objective, which leads to high spatial optical resolution. If the pixel pitch is not sufficiently low the camera will be unable to record the high optical resolution. A camera with low pixel pitch utilizes the full potential of the interferometer system and is therefore preferred.

The camera used in the setup is a Xeva-1.7-640 from Xenics [22]. It has a CCD constructed from InGaAs and consists of 640x512 pixels. The maximum obtainable framerate at full resolution is 90fps. At lower resolutions a framerate of 200fps can be achieved. The InGaAs CCD is sensitive for wavelengths within the range of 0.9 to 1.7μm. As the SLD is in the range of $1265 - 1365\mu m$(FWHM) the camera covers the whole spectral width of the source. Full specifications are found under appendix A.4

The magnification of the system, which consists of the microscope objective and silicon lens, provide a field of view which is approximately $200\mu m\ x\ 160\mu m$ on the camera side. The pixel pitch of the CCD is $20\mu m$ which is good enough for the required spatial resolution as calculated in chapter 4.2.3 which is $0.6\mu m$.

The camera is connected to a computer via a USB 2.0 port. The program X-Control, provided by Xenics, is used for controlling settings, live view, recording and more. Drivers for implementing the same features available in X-Control in LabView are also available from Xenics. This makes it possible to implement the camera in LabView so it can work together with the rest of the system.

Object and reference material

As the material in the objective arm of the interferometer is under investigation, this material sets the requirements for other components. In this case the object can also be modified to increase the quality of the measurements. As the aim of this project is to investigate deformation from the inside of silicon, it is clear that the object arm has to consist of silicon. If possible it is beneficial to have the reference objective (usually a mirror) equal to the object under investigation. This will give equal reflections from each arm which results in maximum contrast in the interference pattern. Investigation of equation 4.5 supports this, as the sum $I_1 + I_2$ is constant for a Michelson interferometer.

Another aspect of having the reference objective equal to the investigated object is that the alignment will be easer when the optical path length is equal. This means that the beams in each arm will travel an equal distance inside silicon.
The material should be modified/formed to fit the optical imaging system for increased resolution.

Both arms consist of two identical custom made silicon lenses. The silicon lenses

are plano-convex where the focal point lies at the plane surface. The convex side is facing the beamsplitter, and the plane surface is accessible at the back side. The height of the lenses are 8mm at the center, and the width is 12.5mm to fit inside standard Thorlabs [20] lens holders. This means that the radius of the convex part is 8mm. The convex surface is anti-reflection treated to increase the illumination and avoid multiple reflections inside the lens. As discussed in 4.2.1 the lens will work as solid immersion, increasing the resolution.

Microscope objective

The microscope objective has to be optimized for near infrared, meaning the transmittance spectrum for the objective should cover the near infra red region. The working distance is an important parameter. It should be long enough so the focal plane is placed on the back of the silicon lens. This means that the working distance should be long enough to travel through the whole silicon lens, as well as the beamsplitter.

The spatial and axial resolution is dependent on the numerical aperture of the microscope objective. The radius of the microscope objective is limited by the size of the cage. Thus having the radius fixed, a higher numerical aperture is equivalent with shorter working distance in this case.

The selected microscope objective is a Mitutoyo 20x NIR objective. It is an infinity corrected objective which means that paralell rays emerges from the back side of the objective and is collected by a tube lens to form the image. For 20x magnification a tube lens with a focal length of 20cm is needed. The numerical aperture and magnification of the objective is important for obtaining the desired image resolution and size. The NA provides an increased resolution while the magnification of 20x is needed to attain a clear image with the camera. Detailed information is found in the datasheet in appendix A.5.

The working distance of the objective is 20mm. The cubical beamsplitter has sides of 15mm and consist of glass. The effective working distance used by the beamsplitter is $15mm/n_{glass} = 15mm/1.5 = 10mm$. As the silicon lenses have a radius of curvature of 8mm this requires 8mm of the working distance. The result is a clearance of 2mm.

Piezoelectric actuator

A piezo is used for moving the reference mirror so phase stepping can be achieved. A linear voltage-displacement curve is preferred for easier programming. When

performing phase stepping the piezo has to be able to delay the reference beam a distance of λ with respect to the object beam. The beam picks up a delay two times as long as the piezo displacement in one round trip. The piezo thus needs a minimum displacement of $\lambda/2$. In the case where the center wavelength is 1290nm the displacement has to be minimum 645nm.

A piezo is also used for making a controlled indentation in the object lens. Longer displacement means more force to the indentation, which is why a piezo with long displacement is desired for this use. Positioning the indent just above the surface of the silicon lens is challenging. A long displacement will therefore also provide better control of the indent before it makes contact with the silicon lens.

Both piezos used are from Thorlabs [20]. The one at the reference arm which is holding the silicon lens is a PAZ005. It has a maximum displacement of $20\mu m$ which is more than sufficient for phase stepping. More information about the PAZ005 can be found under appendix A.6. The piezo used for controlling the indenter is a PAZ020. It has a maximum displacement of $20\mu m$ as well. The PAS020 is equipped with an output channel where displacement, force og voltage can be measured. This channel provides information about how much force the indenter applies to the material. More information about the PAZ005 can be found under appendix A.7.

Vickers indent

To simulate how the sharp SiC particles in the slurry interact with the silicon, a single indentation is performed. The material used for the simulation should be robust and have a known shape.

A Vickers indenter is often used for hardness testing of materials. The same indenter is also suitable for this simulation. The Vickers indenter has a pyramid shaped tip where the angle of the sides are 136°. The material of the tip is diamond and is illustrated in figure 5.7

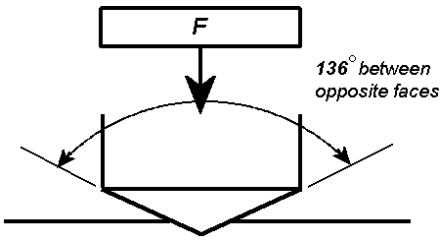

Figure 5.7: Illustration of the tip of the Vickers indenter. Illustration is a reprint from [23]

A microscope image of the Vickers indenter is shown in figure 5.8. This is a microscope image which was taken after all the experiments were performed, and shows that the Vickers still has its tip intact.

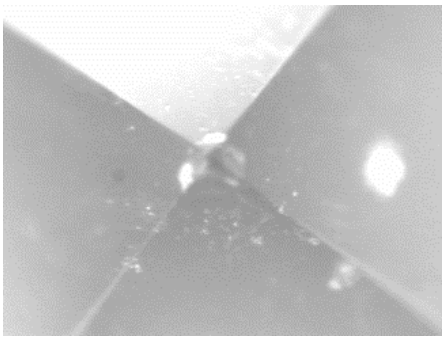

Figure 5.8: Microscope image of the tip of the Vickers indenter. Magnification is 10X.

The Vickers indenter is mounted on a piezo for a controlled indent on the back of the silicon lens. An adapter for mounting the Vickers indenter to the piezo was crafted by the mechanical workshop at NTNU for the project assignment in fall 2010. A sketch of the adapter is attached together with the custom parts in appendix A.2. The field of view of the silicon surface is approximately $170x120\mu m^2$. For the Vickers indenter to hit the right spot on the lens, a precise xyz-translation stage is thus required. The xyz-translation stage for the Vickers indenter can be seen in figure 5.4. The translation stage is used for positioning the Vickers, while the actual indentation is done by the piezo and controlled from a computer.

5.2 Electrical setup

5.2.1 Overview

The electrical setup describes how the two piezos and the camera are controlled. As mentioned in chapter 5.1.2 the camera has a USB connection which provides direct control from a computer. To control the piezos an analog to digital card is needed. The piezo that controls the indenter needs high voltage for maximum actuation. As a result an amplifier is connected between the AD card and piezo. A schematic of the electrical setup is shown in figure 5.9

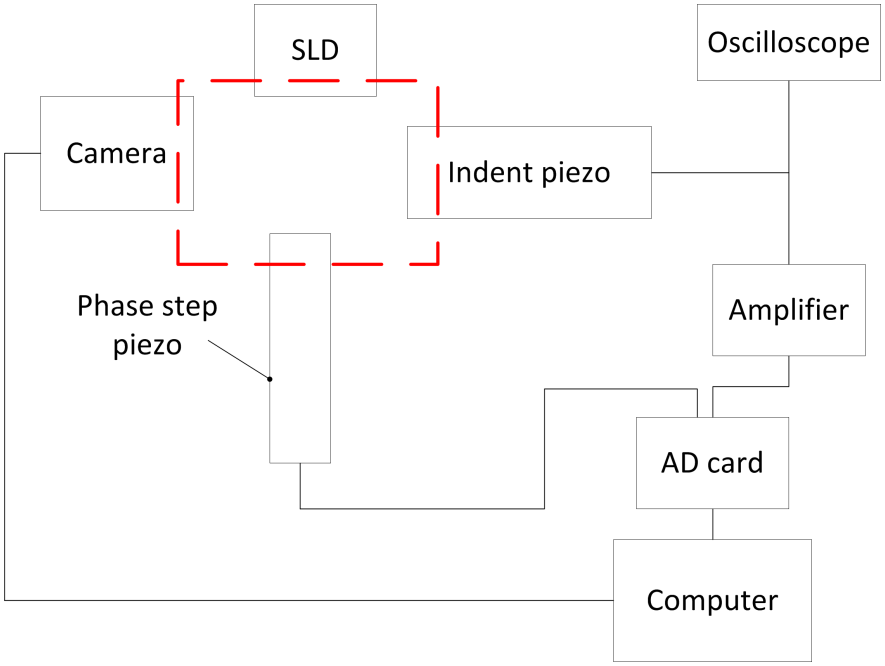

Figure 5.9: Schematic of the electrical setup used for indentation and recording of phase maps. The red cube indicates the interferometer.

The AD card is a four channel module from National Instruments with model number 9263. It delivers a maximum of ten volts which is enough for the reference piezo to be connected directly to the AD card. Full specifications can be found under appendix A.8. The output from the amplifier is connected to the indent piezo as well as an oscilloscope for control readings.

5.2.2 Programming

For purely imaging or only inspecting the interference signal, the X-Control software works well. If phase-stepping and indentation is to occour, all the components have to work together. As X-Control only controls the camera, LabVIEW [24] is introduced. LabVIEW is a program used for developing sophisticated test and control systems. Both piezos and the camera can be controlled via LabVIEW.

Piezo calibration
When performing phase stepping, the distance-voltage relation of the piezo attached in the reference arm is important. The distance-voltage curve is linear except for some millivolts at the starting position. The calibration used to determine the distance-voltage relation is shown with a flowchart in figure 5.10.

The piezo is increased until the reference arm is moved a whole wavelength. The initial image is then equal to the image taken after applying sufficient voltage. The full code is attached in appendix A.9.

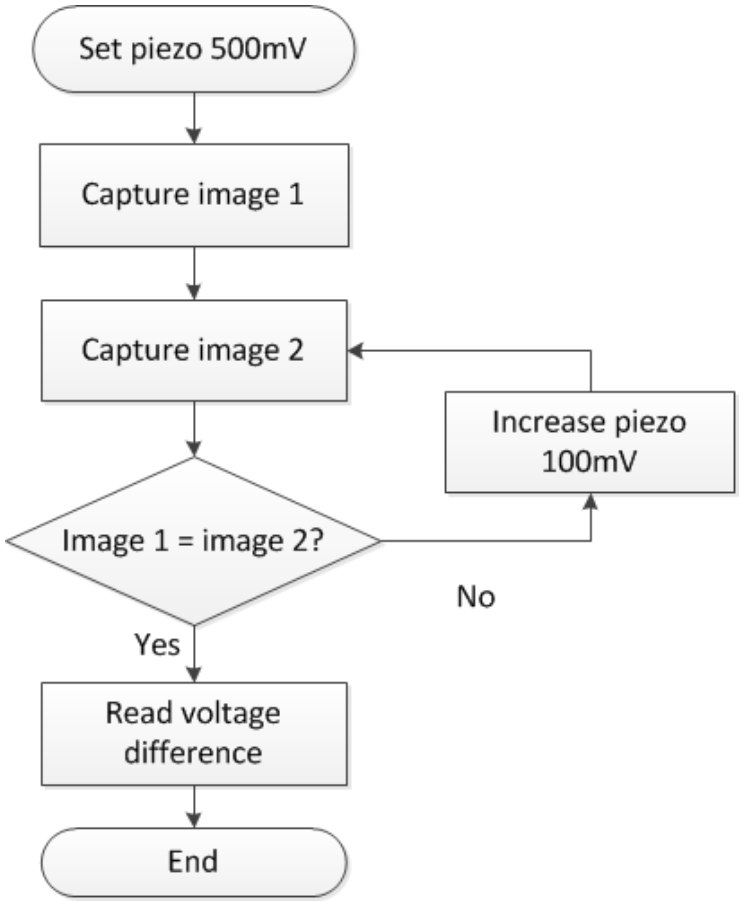

Figure 5.10: Flowchart of piezo phase-stepping calibration routine. Offset of 500mV to avoid the non-linear area of the piezo.

Retrieving Phase map

When the distance-voltage relation is found, we know how many volts equals a 90° phase shift and hence phase-stepping is possible. The flowchart of the routine for making a phasemap is shown in figure 5.11. The program used is LabVIEW which has the feature of implementing MatLab code. The calculation part of the program is therefore executed by MatLab and can be seen on the full code provided in appendix A.10.

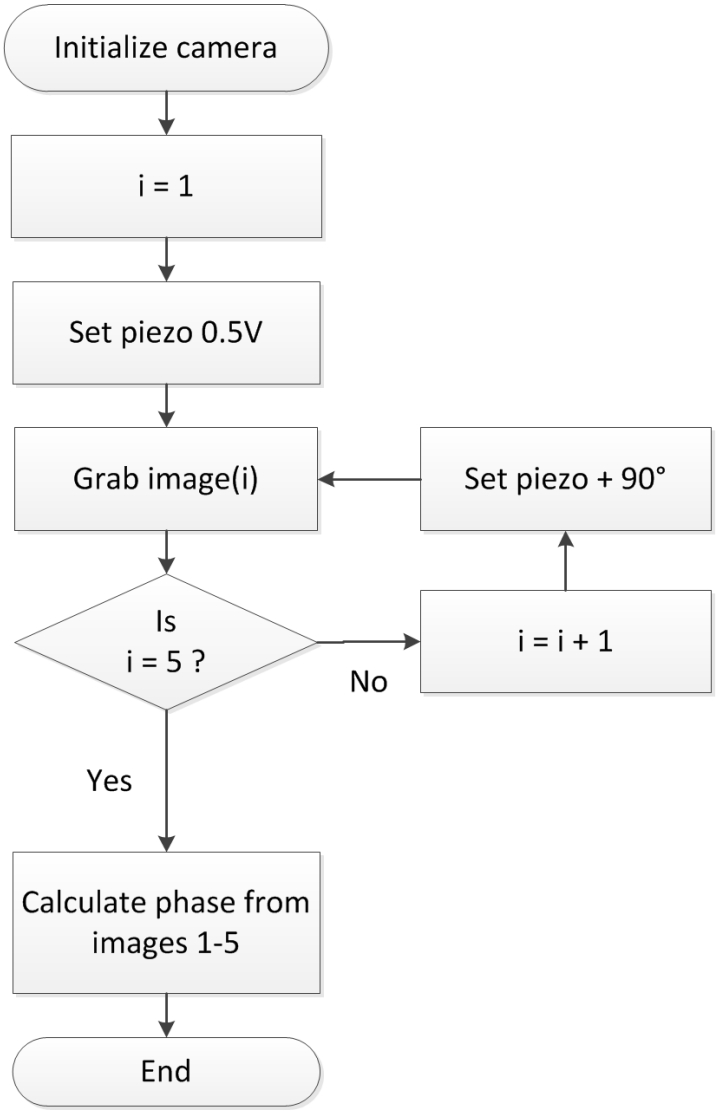

Figure 5.11: Flowchart of how the phase stepping routine is programmed. How many volts equals 90° is found during the calibration.

Indentation and phase map recording

As mentioned under section 5.1.2 two piezos are needed to perform indentation while recording phase maps. A system that controls both piezos and the camera is programmed. A flowchart showing the basics of the program is shown in figure 5.12. For the indentation done in this project, the steps in the flowchart were not programmed to work automatically. The desired depth of the indentation and frequency of phase map recordings is adjustable during indentation. The function for ramping the piezo up or down is provided in appendix A.11. The full code for the indentation and phase map recording can be seen in appendix A.12. The 'grab phase' box in A.12 is the 'Retrieving Phase map' code from A.10.

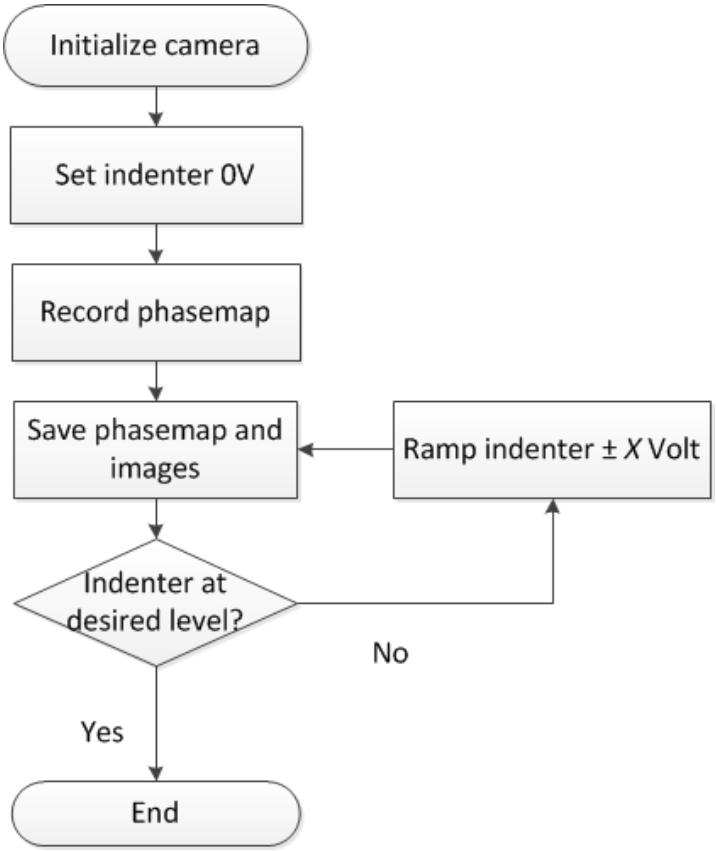

Figure 5.12: Flowchart of how indentation with phasemapping was carried out.

6 Results

In this section the results will be presented. A detailed investigation of the resolution of the system is first carried out. This involves how different components affect the image quality. A custom made resolution chart deposited on the back side of a silicon lens is used as a test object. This custom made silicon lens was processed in the fall of 2010 [25] and is used to determine the resolution limit of the system.

Further several indentations in a silicon sample are presented. These indentations are made on the back side of a plano-convex silicon lens. There are two indentations in lenses with the (100) plane pointing out of the plane surface, and one indentation in a lens where the (111) plane is pointing out. The measurements are done with the use of the setup described in chapter 5. One indentation has been further invesitaged with the Scanning Electron Microscope in the NanoLab at NTNU.

The last section of this chapter contains quantification measurements from an indentation. The depth information about a chipping is investigated. The actual indentation was not performed during this master thesis, only the measurements and calculations.

6.1 Resolution

To measure the optical resolution of the system, a custom made resolution chart is used. This chart is made by deposition of platinum on the plane surface of a plano-convex silicon lens with the form of the lens described in section 4.2.3. The resolution chart is deposited on the plane interface at the center of a silicon lens. As the field of view is not exactly in the middle of the lens, the resolution chart lens is mounted on a xyz-translation stage for positioning and focus adjustment. The different lines in the resolution chart have a specific pitch which represent the resolution of the system. This is indicated in figure 6.1.

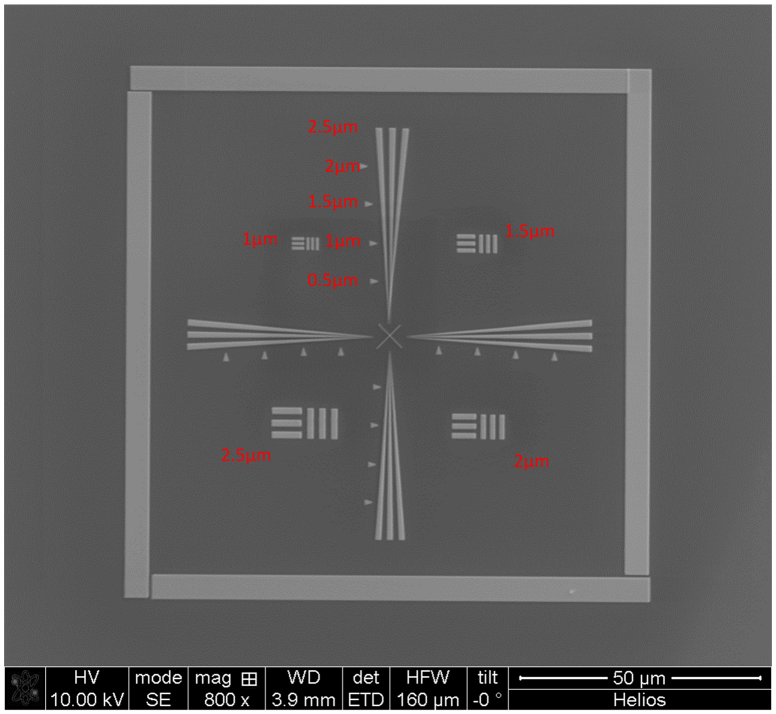

Figure 6.1: SEM image of the custom resolution chart. Different pitch size is marked.

There are several parameters that influence the resolution. The beamsplitter, the wavelength of the illumination source and the presence of a tube lens. To determine the effect of each of these parameters the resolution pattern has been imaged with different setups. The first resolution measurements of the system [25] were carried out with the halogen lamp as background illumination due to practical issues. For comparison reasons, the resolution measurements with a halogen lamp are also performed in this project. The first measurement is with the halogen lamp as background illumination, and without the beamsplitter and tube lens present.

Halogen lamp

Without the tube lens the microscope objective is used as a non-infinity corrected object and the distance to the camera is 16cm for optimal focus. This means that the working distance is not exactly 20mm as specified in the data sheet and the sample is adjusted in the z-direction. It is difficult to direct enough light from the halogen lamp to the desired area of the resolution pattern. The integration time of the camera is therefore adjusted to obtain a bright enough photo. The integration time is set to $4000\mu s$ and the halogen lamp is driven with a voltage of 11volts and a current of 0.76A.

To determine if two points can be separated, several criteria can be used [26]. If the signal amplitude from one point to another is above a specific level, the two points can be separated. To measure this level the minimum and maximum gray level in the image have to considered. The range between minimum and miximum define a signal amplitude of 100%. If the signal amplitude between the lines in the custom resolution chart is above 10%, they are considered resolved in this report. To measure where the signal amplitude drops below 10% the original image from the resolution chart has to be normalized first with respect to the dynamic range, a process often referred to as dynamic range expansion. For 8bit images this means that the minimum gray level in the image is set to 0 and maximum is set to 255. The original and the normalized photo are presented in figures 6.2(a) and 6.2(b), respectively.

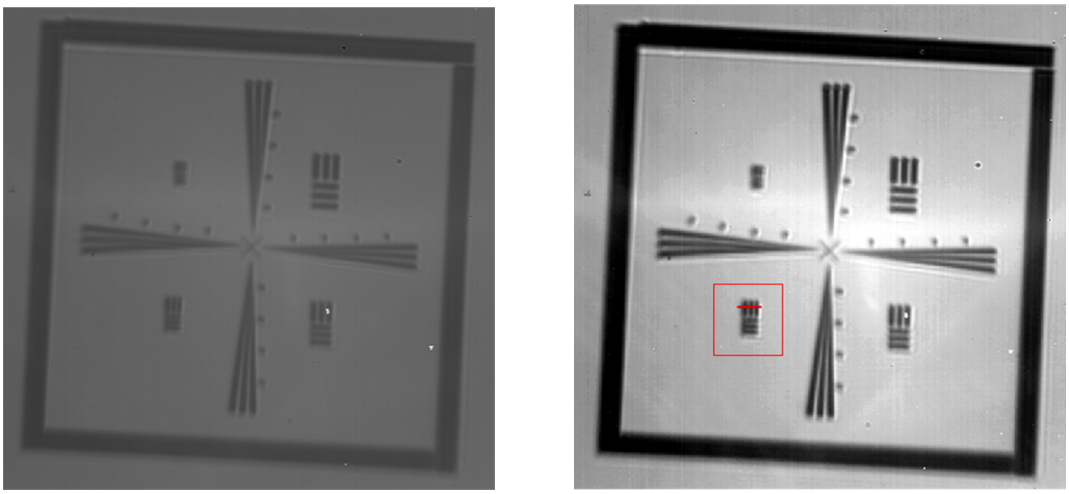

(a) Original photo of the resolution pattern.

(b) Normalized photo. The resolution limit is marked with a red line.

Figure 6.2: Photos of the resolution pattern with a halogen lamp as background illumination. The change from image (a) to (b) is due to the normalization.

With the eye one can see that all the vertical and horizontal elements apart from the smallest one are resolved. To verify this the photo has been examined using MatLab. A horizontal line as indicated in figure 6.2 is selected and the intensity of this line is examined in figure 6.3.

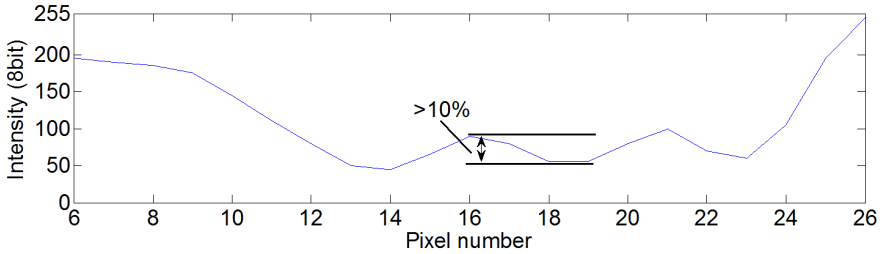

Figure 6.3: Intensity plot corresponding to the line in figure 6.2(b). The lines have a pitch of 1.5μm and are still above 10% signal amplitude.

The results in figure 6.3 reveal that the resolution of the system with a halogen lamp as background illumination is just below 1.5μm. This method for determining the resolution is used for the other optical setups as well.

Halogen lamp and tube lens

An achromatic doublet lens is introduced as a tube lens to work with the microscope objective. Parallel rays now emerge from the microscope objective and are collected by the tube lens which forms an image on the camera. The tube lens has 20cm focal length and gives 20x magnification. With the presence of the tube lens the working distance of the camera is exactly 20mm and the sample is adjusted to obtain focus. The effect of the tube lens is presented in figure 6.4. The integration time of the camera, and the voltage and current applied the halogen lamp are unchanged from previous setup.

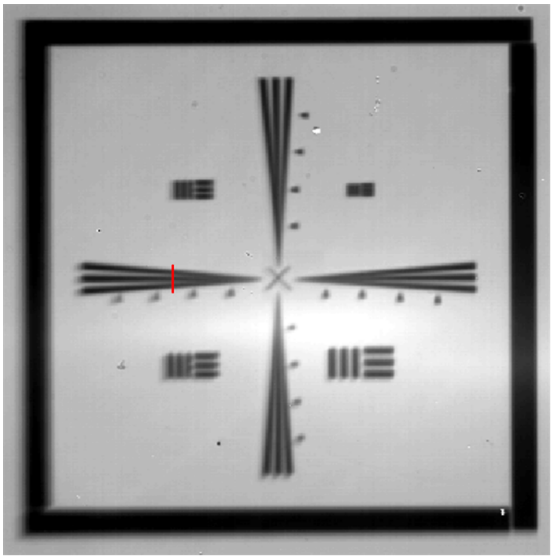

Figure 6.4: Photo of the resolution pattern with halogen background illumination and a tube lens present. Red line represents a resolution of 1.2μm.

With the tube lens present the resolution is further increased. This can be seen with the eye by comparing figures 6.2(b) and 6.4. The vertical lines can be better resolved when the tube lens is present. With the use of MatLab, the intensity of the line can be examined more closely and the result from this reveals that the intensity has dropped to 10% where the lines have a pitch of $1.2\mu m$. $1.2\mu m$ is thus the resolution of the system.

Superluminescent diode

The setup is intended to be used with a SLD with a center wavelength of 1280nm. The SLD can be mounted in the system as background illumination and resolution measurements with this SLD are thus carried out. The intensity of the SLD is much stronger than the halogen lamp, and the integration time of the camera is set down to $1382\mu s$ to prevent the CCD from saturating. As the tube lens is not present, the camera is again placed 16cm from the objective and the sample is adjusted in the z-direction to obtain focus. The result of changing the halogen source with the SLD is shown in figure 6.5.

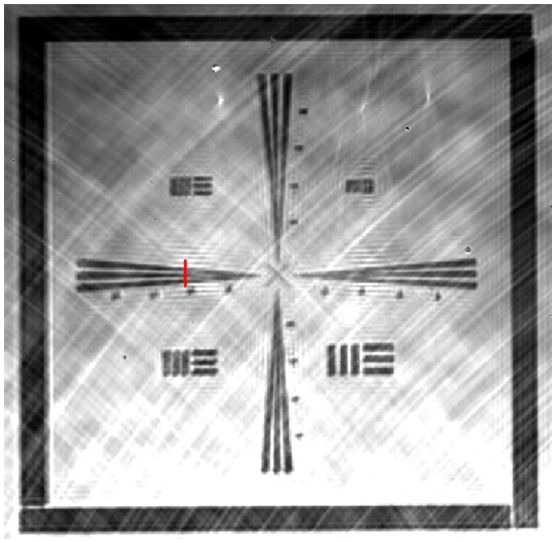

Figure 6.5: Photo of the resolution pattern with a SLD as background illumination. No tube lens present. Red line represents a resolution of $1.1\mu m$

The resolution with the SLD is improved contrary to the halogen lamp. A resolution of $1.1\mu m$ is achieved without the tube lens.

Superluminescent diode and tube lens

With the introduction of the tube lens the sample is adjusted in the z-direction to obtain focus. This causes the illumination from the SLD to be misaligned and the intensity is switched from low to high to obtain enough intensity. As a result of the increased intensity the integration time of the camera is set reduced $288\mu s$. The result of introducing the tube lens is shown in figure 6.6.

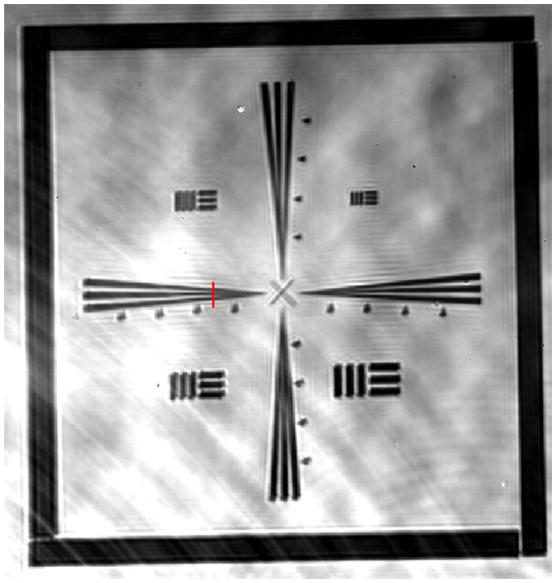

Figure 6.6: Photo of the resolution pattern with a SLD as background illumination and the tube lens present. Red line represents a resolution of $0.8\mu m$

The resolution is further increased with the tube lens in the system and the imaging setup now works as an infinity corrected objective as it is meant to be used. The resolution limit is now $0.8\mu m$ as seen in figure 6.6.

Superluminescent diode and beamsplitter

For interferometric measurements a beamsplitter has to be used. The one designed to fit with this system is a $15x15mm$ cubic glass beamsplitter. The SLD is set to high intensity and the camera has an integration time of $325\mu s$. The effect the beamsplitter has on the resolution is shown in figure 6.7.

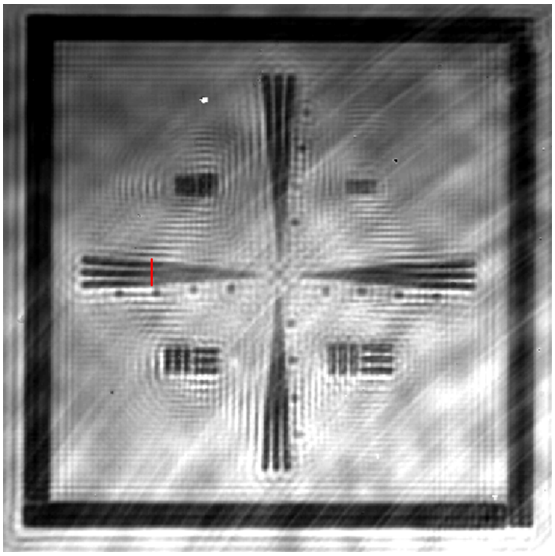

Figure 6.7: Photo of the resolution pattern through the beamsplitter with background illumination. Lines resolved at $1.5\mu m$ pitch.

Superluminescent diode, tubelens and beamsplitter

When introducing the tube lens, the integration time and focus are adjusted to achieve the best resolution. The cameras integration time is set to $407\mu s$ for optimal imaging. The result of including the tube lens is seen in 6.8.

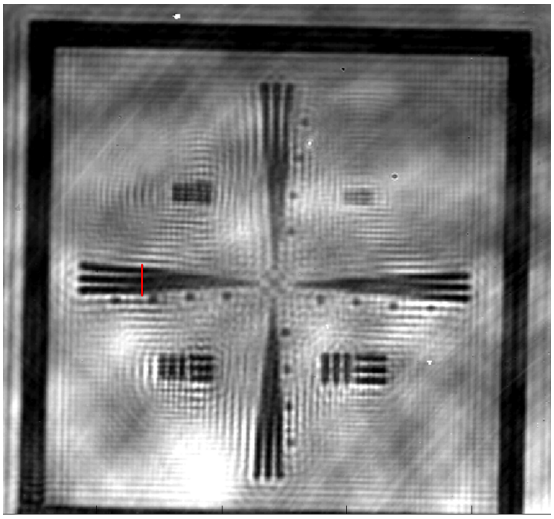

Figure 6.8: Photo of the resolution pattern through the beamsplitter with background illumination and tube lens present. Lines resolved at $1.6\mu m$ pitch.

6.2 Indentation

The aim of this experiment was to simulate how a single Silicon Carbide particle works on the silicon material during wafer sawing. This is done by making several indentations on the plane surface of a plano-convex silicon lens. These indentations will be made with a Vickers indent at different angles with respect to the crystal lattice. There is a total of three indentations presented in this report, where the rotation of the Vickers and crystal direction of the silicon surface varies.

6.2.1 Sample 1

The first indent is made on a sample where the (100) plane is pointing out of the plane surface. The angle of the (001) plane in the crystal lattice with respect to the Vickers is approximately 33° and is shown in figure 6.9. The Vickers is driven by a piezo actuator which has a maximum travel length of $20\mu m$ at 60V.

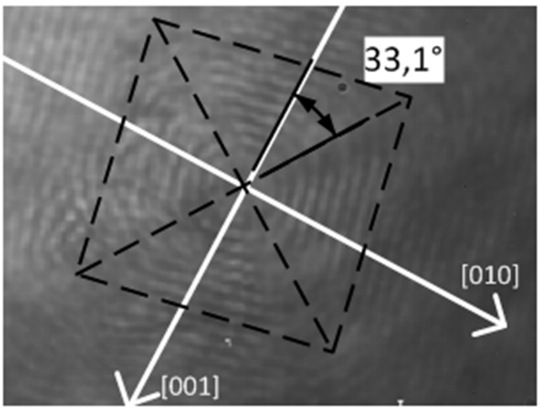

Figure 6.9: White lines represent(approximately) the <001> directions of the crystal lattice. The black square represents the Vickers indent and is drawn on the basis of the Newton rings from the Vickers.

In figure 6.9 the Vickers is some microns away from touching the surface. By increasing the voltage on the piezo to 23V, which equals a displacement of $8.4\mu m$, the Vickers makes contact with the surface. This is shown in figure 6.10(a). This means that the Vickers can be actuated another $11.6\mu m$ when it has made contact with the surface. The piezo is maximum actuated in 6.10(c).

A selection of phase maps that show several stages of the indentation are presented in figure 6.10. Only the area where the indentation is made is shown, and the field of view is approximately $85x70\mu m$.

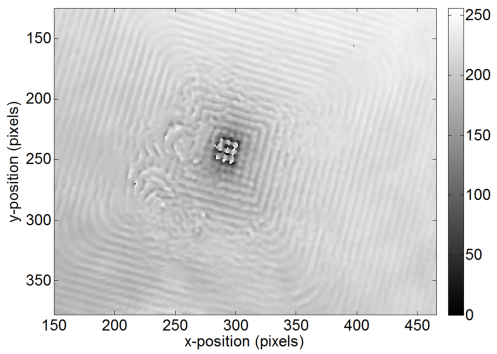

(a) Mod-2π phase map of the indent. Piezo at 32V and actuated 8.4μm.

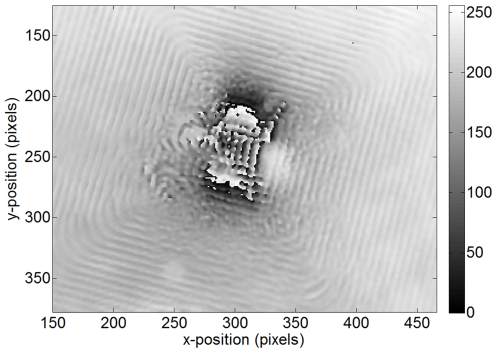

(b) Mod-2π phase map of the indent. Piezo at 44V and actuated 16.4μm.

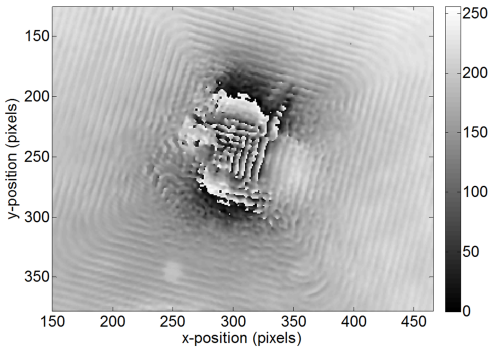

(c) Mod-2π phase map of the indent. Piezo at 61V and fully actuated; 20.6μm.

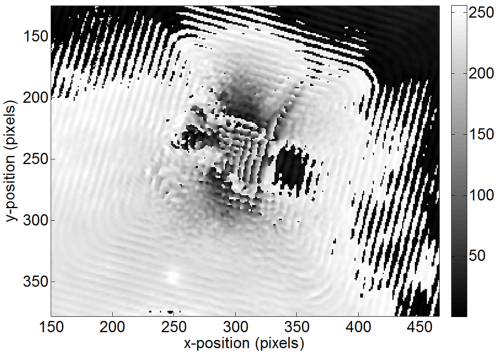

(d) Mod-2π phase map of the indent. Vickers is withdrawing from the sample. Piezo at 46V and actuated 17.8μm.

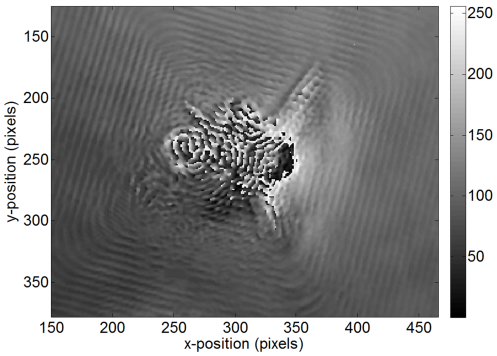

(e) Mod-2π phase map of the indent. Piezo at 15V and piezo 8.5μm.

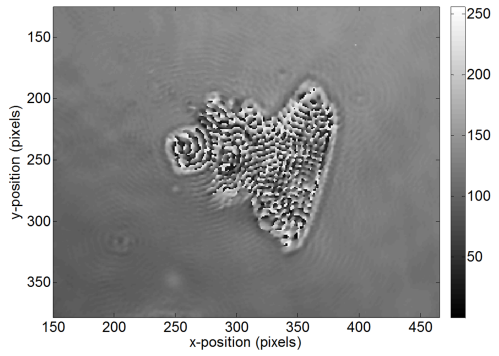

(f) Mod-2π phase map of indent after release of Vickers indent.

Figure 6.10: Mod-2π phase maps of indentation in the (100) plane. Vickers indent is 33° misaligned with respect to the [010] direction of the crystal lattice.

The structure in the middle of the indent is complex with few even surfaces. Due to this the unwrapping of the phase map to obtain an orthographical map is a difficult process. No suitable unwrapping algorithm was available and the phase maps therefore repeat the intensity gradient when moving over a distance equal to a half wavelength. These kind of phase maps are referred to as modulus-2π phase maps. A larger image of the indentation after the Vickers was removed (same as 6.10(f)) is shown in figure 6.11. The phase maps are 8bit gray images. The level of gray of each pixel is given by a number between 0 and 255, where 0 is black and 255 is white.

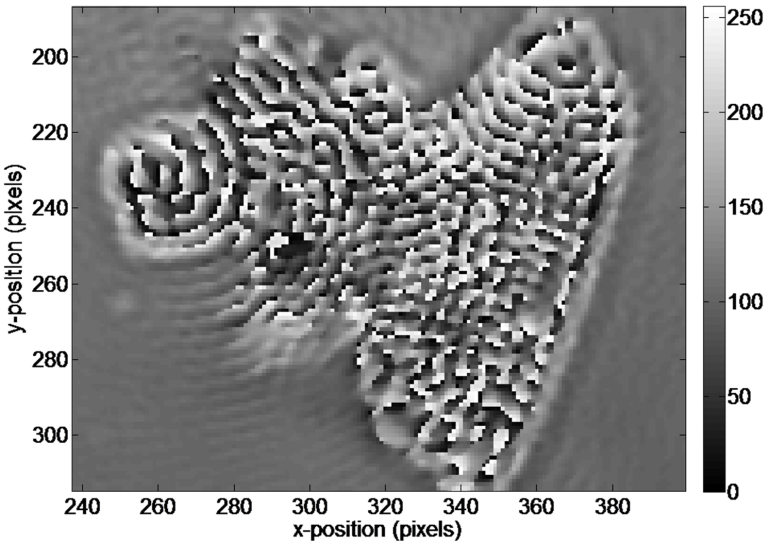

Figure 6.11: Enlarged mod-2π phase map of the indentation in the (100) plane with the Vickers 33° misaligned. Vickers is removed from the sample.

To have a clearer image of the indent, the beamsplitter was taken out of the setup. Interferometry is not possible without the beamsplitter, and thus the clearer image does not contain any phase information. The image may help understand how the phase map can be interpreted as edges and structures are better resolved. The image is shown in figure 6.12.

The sample (silicon lens) was taken to the NanoLab at NTNU for further investigation of the indentation. The measurements were performed by Søren Heinze from NTNU. A Scanning Electron Microscope was used to capture high resolution images. These images are taken of the plane surface of the silicon lens which means that the indent is seen from the outside contrary to the phase maps which are seen from the inside. Due to this the, SEM images are vertically mirrored and rotated for easier comparison. Only one image from the SEM is presented in this report, and can be seen in figure 6.13.

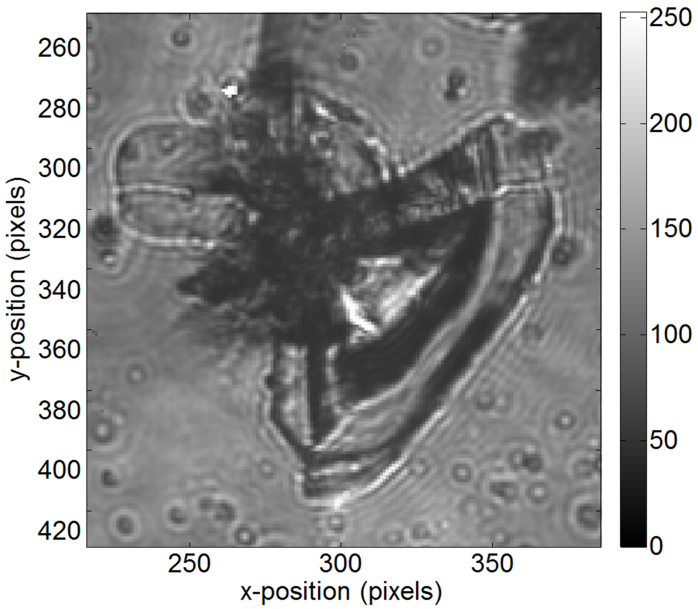

Figure 6.12: Image of the indentation in the (100) plane with the Vickers 33° misaligned. The SLD is used as background illumination and the beamsplitter is removed for optimal imaging.

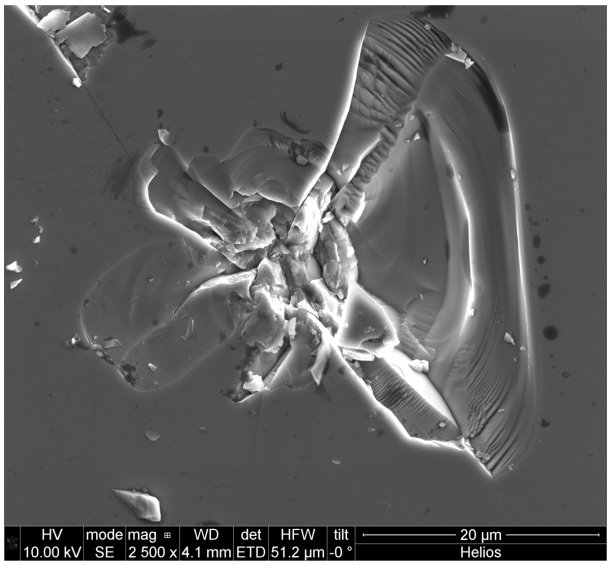

Figure 6.13: SEM image of the indent in the (100) plane with the Vickers 33° misaligned. Image is taken by Søren Heinze in a Scanning Electron Microscope.

6.2.2 Sample 2

In this experiment the corners of the Vickers indenter is aligned with the <001> directions of the lattice which is illustrated in figure 6.14. A series of phase maps of this indentation are shown in figure 6.15. Only the area of interest is shown, yielding a field of view of approximately $80x70\mu m$.

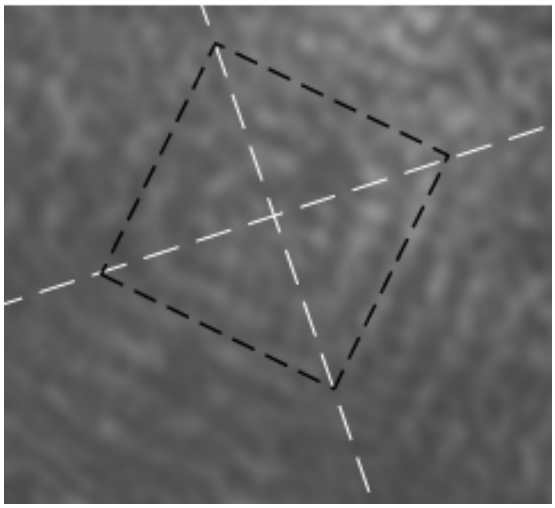

Figure 6.14: White lines represent (approximately) the <001> directions of the crystal lattice. The black square represents the Vickers indent and its corners are aligned with the crystal lattice.

The indent made contact with the surface when actuated $5.3\mu m$ which is seen in figure 6.15(a). The Vickers is actuated another $9.2\mu m$ into the silicon surface and phase maps are taken at approximately every $0.6\mu m$. The three first phasemaps after contact with the silicon surface are seen in figure 6.15(a)-(c) and show that deformation happens at an early stage.

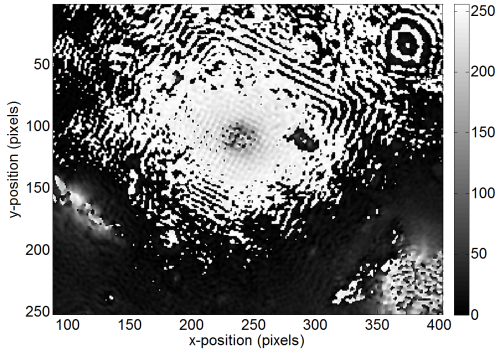

(a) Mod-2π phase map of the indent. Piezo at 15V and actuated 5.3μm.

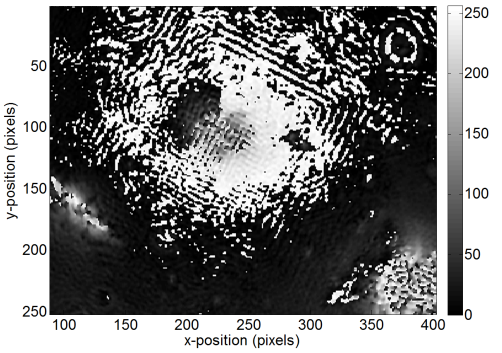

(b) Mod-2π phase map of the indent. Piezo at 17V and actuated 5.9μm.

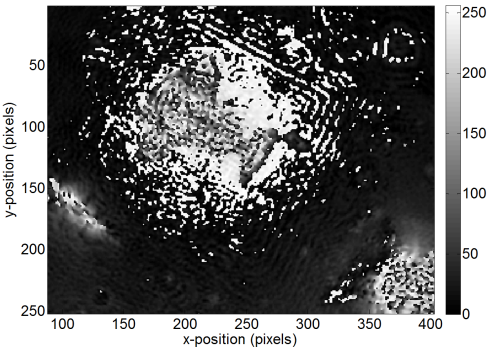

(c) Mod-2π phase map of the indent. Piezo at 18V and actuated 6.6μm.

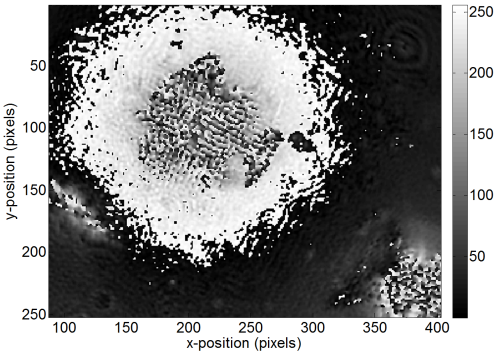

(d) Mod-2π phase map of the indent. Piezo at 40V and fully actuated; 14.5μm.

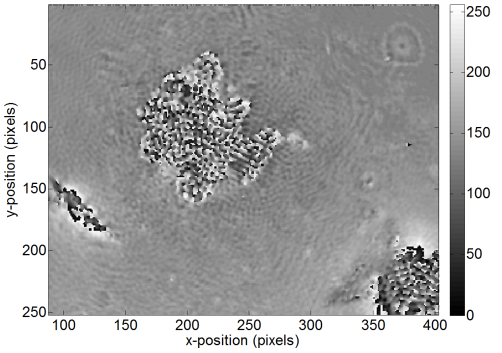

(e) Mod-2π phase map of the indent. Piezo at 42V and piezo 4.9μm. Vickers now withdrawing from the sample.

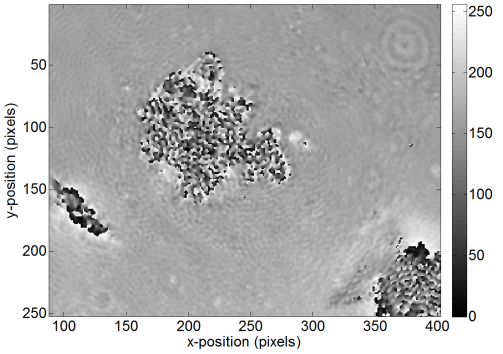

(f) Mod-2π phase map of indent after release of Vickers indent.

Figure 6.15: Mod-2π phase maps of indentation in the (100) plane. Corners of the Vickers indent are aligned with the [010] and [001] directions of the the crystal lattice.

6.2.3 Sample 3

In the two previous samples the plane surface is cut so the (100) plane was pointing out of the surface. The third sample is cut so the (111) plane is pointing out of the plane surface of the lens. The wikers is in this case aligned with on of the perpendicular <111> direrciones, shwon in figure 6.16. The Vickers makes contact with the plane silicon surface when the indent is at 16V which equals an actuation of $5.4\mu m$. Phase maps are taken at every $0.5\mu m$ separation and the piezo is actuated to $20.3\mu m$. Six phase maps of the indent are presented in figure 6.17 where the field of view is approximately $90x70\mu m$.

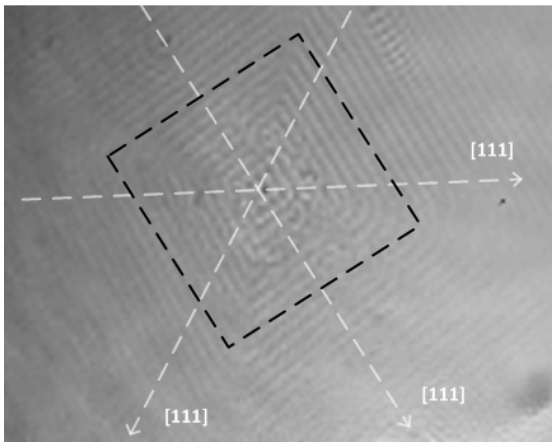

Figure 6.16: White lines represent (approximately) the <111> directions perpendicular to the surface of the crystal lattice. The black square represents the Vickers indent.

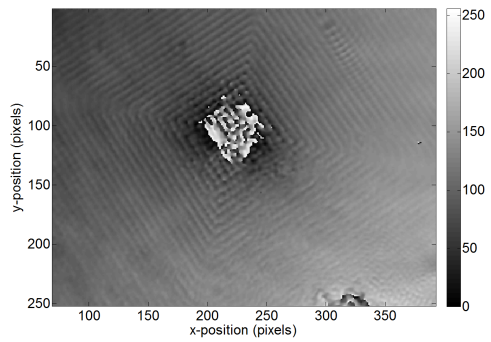

(a) Mod-2π phase map of the indent. Piezo at 32V and actuated 12μm.

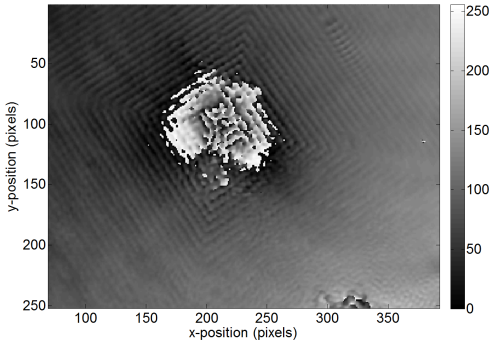

(b) Mod-2π phase map of the indent. Piezo at 43V and actuated 15.5μm.

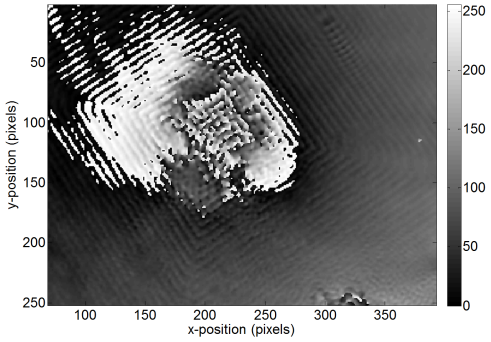

(c) Mod-2π phase map of the indent. Piezo at 60V and fully actuated; 20.3μm.

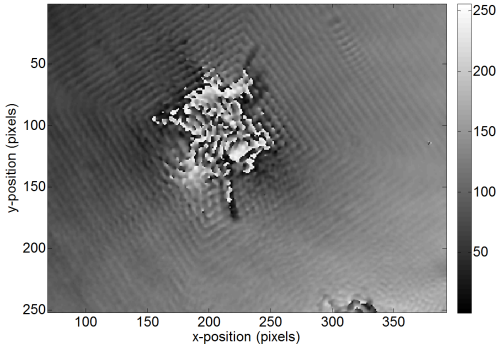

(d) Mod-2π phase map of the indent. Piezo at 33V and actuated 14.3μm. Vickers now withdrawing from the sample.

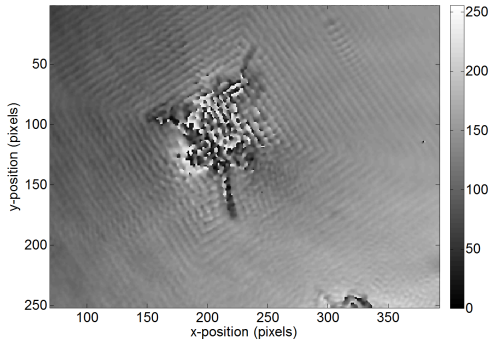

(e) Mod-2π phase map of the indent. Piezo at 24V and piezo 11.4μm.

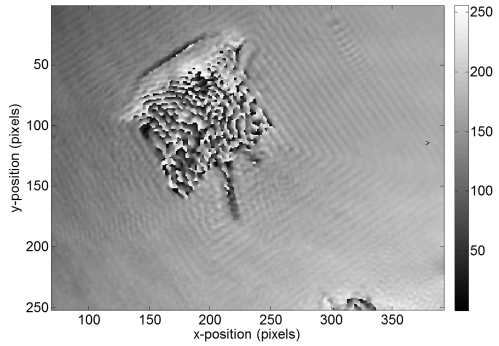

(f) Mod-2π phase map of the indent. Piezo at 23V and piezo 8.4μm.

Figure 6.17: Mod-2π phase maps of indentation in a (111) plane. The Vickers indenter is aligned with one of the <111> directions which are normal to the surface.

A possibility when using phase maps is that one phase map can be subtracted from another to calculate the difference between them. Deducting two phase maps will in this case reveal how the deformation has progressed from one stage to another. Deducting phase map shown in figure 6.17(e) with 6.17(f) will show the deformation when the Vickers was moved out of the sample from $11.4\mu m$ to $8.4\mu m$. The result of such a subtraction is presented in figure 6.18.

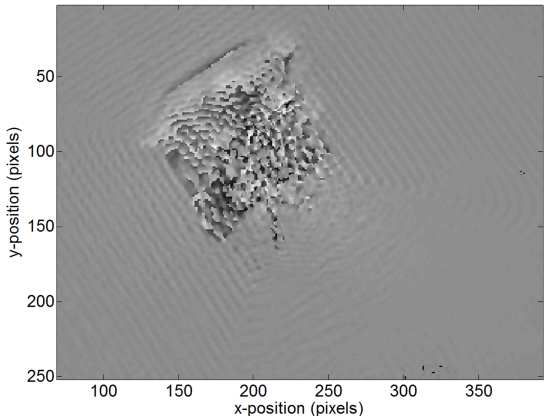

Figure 6.18: Mod-2π phase map of the deformation when releasing the Vickers from $11.4\mu m$ to $8.4\mu m$. Indentation is in a sample with the (111) plane pointing out of the surface and Vickers aligned with one of the <111> planes.

The beamsplitter was in this case also removed and the indent was imaged without the aberrations from the beamsplitter. The result is shown in figure 6.19.

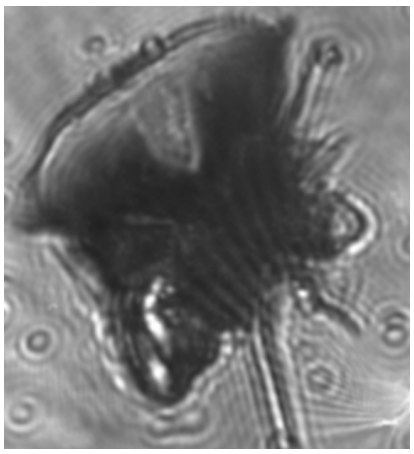

Figure 6.19: Image of the indent in the (111) plane with the Vickers aligned with one of the <111> planes. SLD is used as background illumination and the beamsplitter is removed for optimal imaging.

6.3 Quantification

In fall 2010 the first experiment of recording phase maps of an indentation was performed [25]. This indentation was also examined in a confocal microscope by Sergio Armada. An image of the indentation was made with a corresponding depth profile. This image and depth profile is shown in figures 6.20(a) and 6.21. These confocal microscopy images can be used to verify if the depth information from the phase maps are valid. There is a line plotted in figure 6.20(a). The depth profile of this line is shown in figure 6.21. From $16 - 20\mu m$ an even wedge from a chipping can be seen. This wedge is the outmost part of the line in figure 6.20(a) and is $1\mu m$ deep according to the profile plot.

The phase map of the same indent is shown in figure 6.20(b). The profile line in figure 6.20(a) has an angle of approximately 33% to the upper crack. A $20\mu m$ line with the same angle is drawn in the phase map in figure 6.20(b), where the blue part represents the last $4\mu m$. Taking a closer look at the phase along this line will reveal how deep it is. The blue part of the line in figure 6.20(b) covers three fringes. From one fringe to another fringe the depth has increased with half a wavelength. As we are working inside silicon, the wavelength has to be scaled with a factor $n = 3.5$ equal the refractive index. Half a wavelength inside silicon equals $1280nm/(3.5 * 2) \approx 0.18\mu m$. Three fringes implies a total depth of $0.55\mu m$. The result from the confocal microscope proved a depth of $1\mu m$ which is almost a factor two higher.

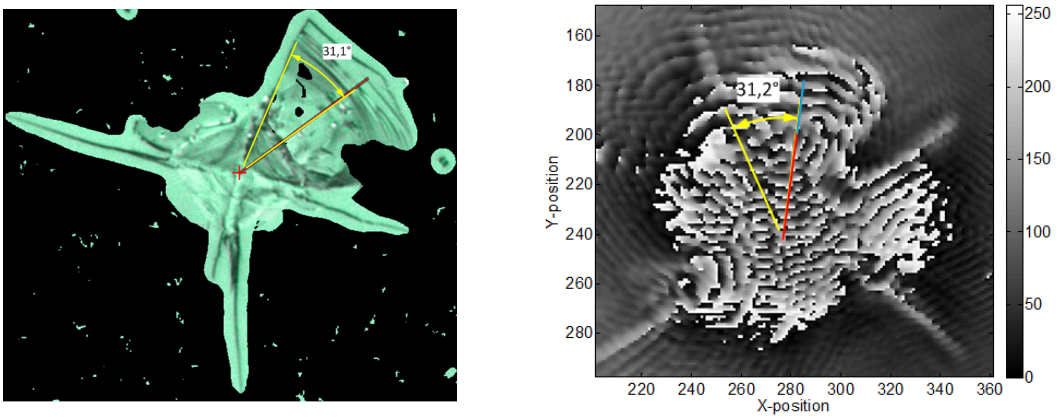

(a) Confocal microscope image of an indentation. The red line indicate the depth profile shown in figure 6.21.

(b) Mod-2π phase map of the indentation. The depth profile along the red and blue line is calculated with the mod-2π phase map

Figure 6.20: Confocal microscope and mod-2π phase map of indentation taken in fall 2010.

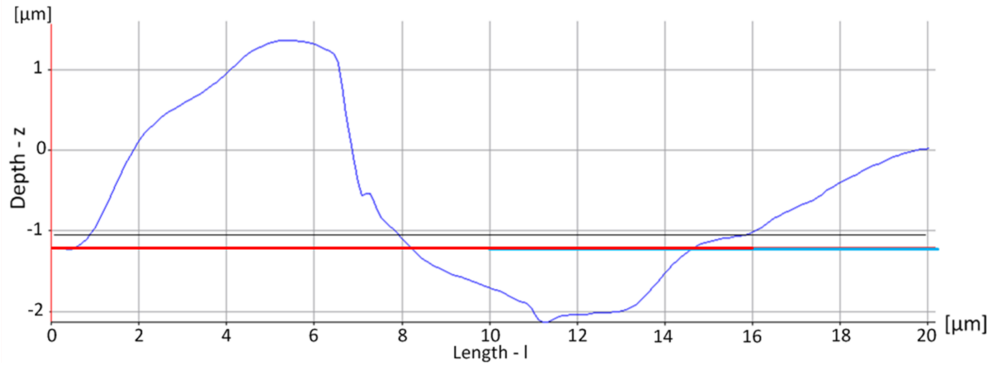

Figure 6.21: Depth profile of a chipping. The corresponding line is shown in figure 6.20(a). The part blue part from $16\mu m$ to $20\mu m$ is used as a reference for calculation.

7 Discussion

7.1 Resolution

Two different light sources were used in the setup shown in figure 5.5. The introduction of the SLD resulted in another resolution than with halogen illumination. The halogen illumination has a broader spectrum than the SLD, and a part of this spectrum is absorbed when imaging inside silicon. The spectral response curve is affected by both the illumination and camera, and has a center of gravity at approximately 1460nm [27] whereas the SLD has 1280nm. This results in a resolution of $1.5\mu m$ as seen in figure 6.4. Switching from halogen illumination to the SLD increased the resolution as expected and provided a resolution of $1.1\mu m$.

The microscope objective is an infinity corrected objective and works optimally together with a tube lens. The tube lens increases the resolution with a factor of 1.3 for halogen illumination and 1.4 for the SLD. These two numbers should in theory be equal. The figures in section 6.1 showing the photos of the resolution charts for the halogen and SLD illumination are cropped and do not show the original position of the chart on the photo. As the positioning of the resolution chart is done manually, it varied a bit from measurement to measurement. If the surface of the lens is perfect and all components are perfectly aligned, the best resolution is obtained at the center of the plane surface of the lens. In practice the components are always a bit misaligned, and this may lead to different resolution at different places in the image. By inspecting the resolution images closely it is seen that the fan pattern is not resolved equally on all sides. A good example of this is figure 6.6. Here the lower part of the resolution chart is not as well resolved as the left, right or top part. These small differences are most likely the reason the tube lens functions better with the SLD than the halogen lamp.

When the beamsplitter is present the effect of the tube lens is reversed, and the resolution drops from $1.5\mu m$ to $1.6\mu m$. The beamsplitter introduces spherical aberrations which the microscope objective is not designed for. The tube lens can not correct the aberrations, and seem to enhance the problem. This may be the reason the tube lens has little effect on the image together with the beamsplitter.

An other effect due to the beamsplitter is the grid pattern seen in figures 6.7 and 6.8. By inspecting this grid pattern in the area around the frame of the resolution pattern, it is seen that the pattern has the same angle as the frame itself. This indicates that the grid pattern originates from the frame and the pattern itself.

7.2 General indentation

By inspecting the indents in samples one, two and three, it can be seen the background intensity is changing during the indentation. This is seen in figures 6.10, 6.15 and 6.17 for sample one, two and three, respectively. This can mean that the plane back surface of the sample lens is pressed together by the indenter and is compressed. A more plausible explanation is that the sample lens itself moves. Pressing the indenter against the sample can make the sample move inside the sample holder even though it is fastened in the lens tube by retaining rings. The background in sample 2, figure 6.15, is changing from black to light gray. The black area has 0 gray level, while the light gray has 160 gray level. 0 to 255 gray level equals movement of half a wavelength. A change in the background from 0 to 160 graylevel is thus $160/255 * \frac{1}{2}\lambda \approx 400nm$. A displacement of $400nm$ is small and could be explained by either of the two scenarios mentioned above.

Another displacement may be the Vickers indenting system itself. When actuating the piezo, the piezo and Vickers indenter itself may be pressed a bit backward instead of into the sample. Due to this it is not certain that the readouts from the strain reader correspond to how far into the sample the piezo actually is. This feedback of the Vickers is measured in advanced indenting systems, and is desired for more precise results with this setup as well.

Incoming light will be reflected at twice the incident angle. If a slope is so steep that total internal reflection occurs, the light will have an angle of reflection of at least $16.6° * 2 = 33.2°$. The microscope objective collects light at a maximum angle of 23.6° which means that only a small part of the light which is totally internal reflected will contribute to the image. The source is collimated when hitting the convex part of the lens. This will make the illumination converge inside the lens meaning the incident light on the plane surface has a slight angle. Due to this angle more light is reflected in the direction of the microscope objective and chipping with larger angles can be imaged.

The theoretical estimate for the axial resolution from chapter 4.2.3 is $0.7\mu m$. From the depth profile from the confocal microscope in section 6.3 it is seen that indentation can be expected to be larger than $0.7\mu m$. This means that some parts of the indent do not lie inside the focal point, and the structures from these areas may not be as clear. The theoretical estimate of $0.7\mu m$ did not consider the aberrations introduced by the beamsplitter. With the beamsplitter in the system the axial resolution may be changed, but this was not investigated in the scope of this thesis.

As the structure of the indent is not a flat surface, multiple reflections may occur. The light beam has then been reflected several times, and maybe even

experienced total internal reflection. If this light hits the CCD it will seem to originate from a place in the indent, but the phase does not correspond to the depth. The phase is in this case altered by the extra optical path length of the light, as well as phase change introduced by total internal refection. Such effects are unfortunate for interpreting the phase maps.

At atmospheric pressure the silicon has a diamond structure. During indentation the pressure on the silicon will increase and the lattice structure may change into several metastable phases [28]. A body centered tetragonal phase is most likely just beneath the indent and this phase behaves like a metal. How these metastable phases influence the reflected light is uncertain. If a change in the refractive index is introduced this will give rise to reflections as well as alter the phase of the light. When using the phase for depth and structural investigation a uniform medium is of preference and these phase transformations may distort the phase map. Using the setup for examining the phase transformations is another interesting aspect, but is not considered in this report.

The phase maps of all three samples are hard to interpret. There are few continuous phase transitions in the area of the indent. This might be due to too abrupt transitions in the material and residue silicon from the indentation. Figure 6.13 shows a SEM image of the indentation in sample 1. This image provides great detail of the surface of the indent, and it is seen that the surface is rough and irregular. It is likely that multiple reflections occur and make the phase maps stochastic in some areas.

Some areas where chipping has occurred have smooth surfaces and the phase transitions are continuous. Such an area can be seen to the left in sample 1. A round chipping can be observed in phase maps 6.10(f) and enlarged in 6.11. Inspecting this round chipping without the beamsplitter present (upper left corner of figure 6.12) it is seen to have a more rectangular shape with rounded corners and a vertical split in the middle. This is verified with the SEM image presented in figure 6.13. The depth and size of this round chipping may be calculated from the phase map with the same technique used in section 6.3 if the slope of the chipping is not too steep. Having SEM and better resolved images to compare the structures with helps to understand what kind of structures that can be localized with the phase maps.

In figure 6.11 the pixelation in the images can be seen. The phase fringes are not as smooth in every area and the form of the fringes may seem abrupt. A camera with higher resolution will solve this problem and the phase transitions will be smoother.

7.3 Sample differences

Not much deformation except cracks could be seen when the Vickers was pressed into sample 1 in figure 6.10(a)-(d). At full indentation, shown in figure 6.10(c), parts of a pyramid shape can be seen, with cracks emerging from three sides. When releasing the Vickers from $20.6\mu m$ to $17.8\mu m$, dark areas which represent a depth change in the surface can be seen on the left and right side of the indentation. When releasing the Vickers completely, the area on the left side becomes a round chipping, while the right side becomes a triangular chipping. This might be due to stress that is built up in the sample, and on release results in chipping.

Looking at the indentation in sample 3 shown in figure 6.17, it is somehow similar to sample 1. Cracks emerge from the indented area and chipping occurs at the top and left side of the indentation. The size and form of the chipping are different and are most likely an effect of indenting in the [111] plane instead of [100]. The distinct change in background intensity where chipping occurred in sample 1 is not seen in sample 3 and prediction of chipping is harder.

Aligning the corners of the Vickers with the <001> directions of the crystal lattice in sample 2 produced different deformation than with unaligned Vickers. A large deformation on the left side of the indentation could be seen after actuating the piezo only $5.9\mu m$ in figure 6.15(b). When increasing the piezo to $6.6\mu m$ in the figure the deformation at the left side had grown significantly, and another deformation at the right side had appeared. This huge deformation happened at an early stage when the piezo was on its way into the sample. The actuation of the Vickers stopped at $14.5\mu m$ shown in figure 6.15(d), and was then released. When the Vickers was released from sample 1 and 3, chipping occurred. This was not the case for sample 2, and the reason may be that not enough stress was built up as the Vickers was not actuated fully to $20\mu m$. Another possibility is that the deformation in the beginning of the indentation absorbed some of the stress built up by the Vickers, and prevented chipping during release.

7.4 Quantification

The indent from the project assignment was examined in a confocal microscope in figure 6.20. The last $4\mu m$ of the $20\mu m$ line proved to have a depth of $1\mu m$. This is equal to an average angle of 14°. The depth of this $4\mu m$ line calculated from phase maps provided another result; $0.55\mu m$. This is a large deviation which has to be analyzed.

From the image of the resolution chart in figure 6.8 it is seen that two lines which have a pitch smaller than $1.6\mu m$ are not resolved. This is also true for the interference fringes. If the distance between each destructive interference fringe is smaller than $1.6\mu m$ the lines will not be resolved. This affects the phase maps in the same way.

As the fringes from the phase maps are directly connected to the surface topography, the resolution of the system sets a limit to how steep wedges that can be measured. Closer fringes correspond to steeper wedges. If the angle of a wedge is too large, the interference fringes will be so close that they are not resolved by the microscope objective. Given the resolution and the effective wavelength of the system, an upper angle of limitation can be calculated. The measurement of the spatial resolution indicates that two fringes cannot be closer than $1.6\mu m$ which is equal to $0.63 fringes/\mu m$. From one fringe to another the depth is half a wavelength in silicon; $1280nm/(3.5 * 2) \approx 0.18\mu m$. With the transverse length equal to $1.6\mu m$ and the depth equal to $0.18\mu m$ this limitation angle can be calculated to $tan^{-1}(\frac{0.18}{1.6}\mu m) = 6.42°$. This implies that if the angle is above $6.42°$ the interference fringes are too close to be resolved by the setup.

The pixels on the camera sample the analog image [29]. If we for simplicity assume that the pixels are circular detectors, each pixel will sample the analog image with a form of an airy disk. Consider the case where the slope is so steep that the interference fringes are not resolved. This is illustrated in figure 7.1. Note that the slope of the silicon surface is not shown in figure 7.1, only the resulting interference fringes.

The contribution to one pixel is the area that the airy disk covers. This area is illustrated with the blue dotted line in figure 7.1. As there is a number of interference fringes within one airy disk, the different phases of the light will be summarized and the destructive and constructive interference will cancel each other out. The residue of the summarization will then represent the phase of the light. The summarization of the phases are illustrated with the shaded area in the interference fringes in figure 7.1. The net summarization from a neighboring pixel will result in a slightly different phase.

The pixel represented with blue in figure 7.1 has a positive net phase value, while the neighboring pixel represented with dotted green line has a negative net phase value. Expanding to more pixels will reveal a sinusoidal intensity pattern, where the corresponding phase has a saw-tooth form. The periodicity of this new phase is lower than the periodicity of the original non-resolved phase of the interference pattern.

The size of the airy disk in figure 7.1 is formed by the microscope objective.

The airy disks from two neighboring pixels are so close that they overlap each other.

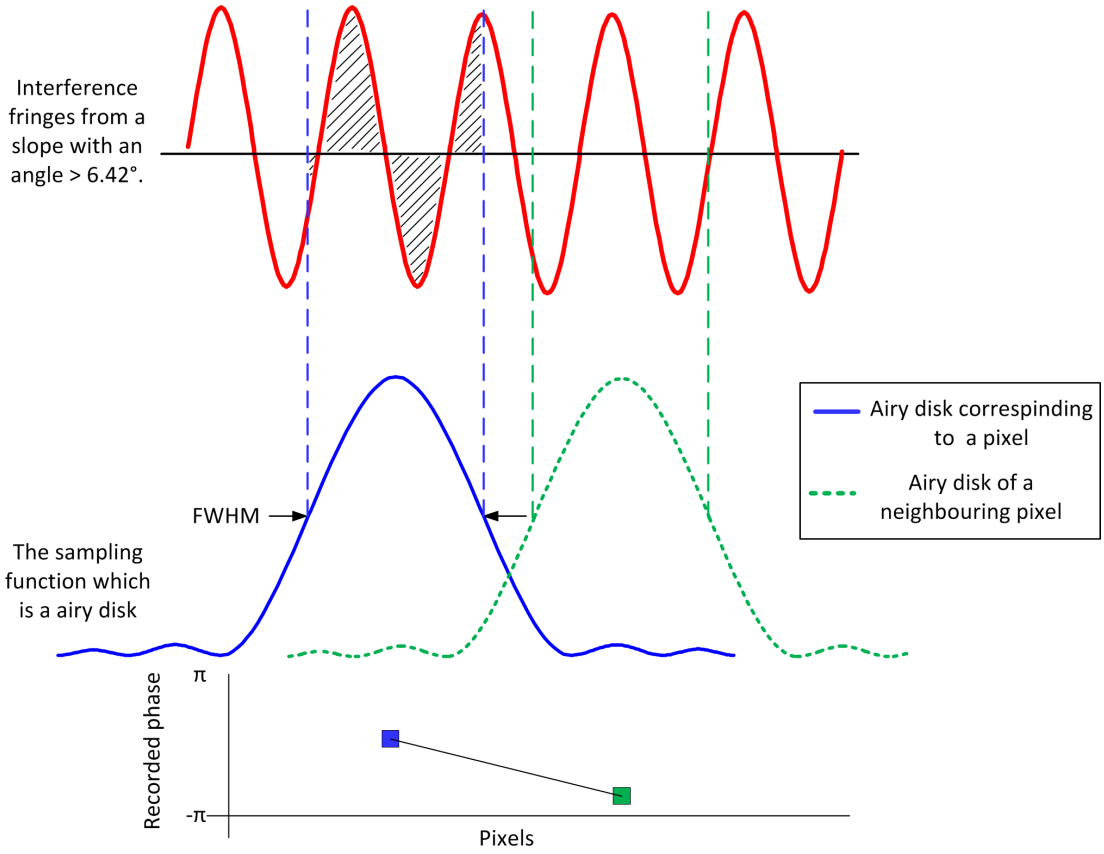

Figure 7.1: Illustration showing what happens when imaging interference fringes with a frequency higher than the resolution limit for the imaging system. The summarization of interference fringes within the airy disk corresponding to one pixel is indicated. Two slightly overlapping pixels is shown. Frequency of the resulting phase is lower than the frequency of the original interference pattern.

The smallest period that can be resolved is $1.6\mu m$. According to the Nyquist theorem in section 4.7 the lens needs a sampling frequency twice the highest frequency or half the period of the analog signal for a perfect reconstruction. The smallest period that can be resolved by the optical setup is $1.6\mu m$. This means that the lens is operating with a sampling period of $1.6\mu m/2 = 0.8\mu m$. If the image contains fringes with a period smaller than $1.6\mu m$ these periods will result in samples which are aliases of larger periods.

Consider a pattern with a period smaller than $1.6\mu m$. This is similar to the resolution chart used in figure 6.1. Toward the center of the pattern the lines

are so close that they are not resolved by the system. This will not result in the same effect as with the phase maps. An interference pattern containing phase information created the intensity on the CCD and destructive and constructive interference could in that case cancel each other out. This cancellation does not happen when imaging an intensity pattern i.e. the resolution chart, and all the intensities which a airy disk covers will be squared and summarized. The result will in this case be a blurring effect.

When performing indentations, some depth levels of the indent does not have optimal focus. This was discussed in more detail in section 7.2. The sampling frequency in these unfocused areas will be lower, and the threshold for aliasing is thus reduced.

7.5 Advantages and limitations of the LCI technique

As for all measuring systems the current setup has limitations and advantages. The different aspects of the setup will here be accounted for.

The main advantage with this LCI setup is that deformation in silicon can be recorded and imaged in-situ. As the source operates at 1280nm the deformation is imaged from the inside, and the view is not blocked by any Vickers indent or steel wire which is in contact with the silicon. With solid immersion utilized the optical spatial resolution of the system is currently at $1.6\mu m$ which is enough to detect deformation.

A high optical spatial resolution is a trade off with respect to depth of focus. High spatial resolution results in short depth of focus wich was theoretically calculated to $0.7\mu m$. Deep deformations will thus have unfocused areas at some depth levels as discussed in section 7.2.

The coherence layer is theoretically calculated to be $4.1\mu m$ which is wide enough to cover a whole indentation. This means that phase maps of the whole depth of the indentation is recorded. For inspection of an indent this is not optimal, as it is harder to separate different depth levels for inspection.

The interpretation of the phase maps is a challenge. As mentioned in sections 7.2 and 7.4 the phase maps may contain false depth information which need further investigation.

Section 7.4 also examined how steep chippings that can be characterized. The angle of the chipping is limited to 6.42°.

8 Future work

Resolution
The resolution of the system is critical. By increasing the resolution of the system steeper chippings may be characterized. If the resolution of the system was increased to $0.8\mu m$, 1.25 fringes pr micrometer could be resolved. The resulting limitation angle for the chipping will then increase to $tan^{-}1(\frac{0.18}{0.8}\mu m) = 12.7°$.

By introducing a pellice beamsplitter, the light path does not consist of 15mm of glass as it did with the cubical beamsplitter present. A pellice beamsplitter consist of a thin membrane which separates the light beam. A pellice with a membrane of $2\mu m$ has been suggested for the setup and is illustrated in figure 8.1. The thin membrane eliminates aberrations, and will increase the resolution of the system. The working distance for the microscope objective is exactly 20mm. This introduces a problem since the lenses have a center thickness of 8mm and the pellice itself 35mm long. A 35mm long pellice at 45° will have 12.7mm clearance from the membrane to the microscope objective. The working distance of the microscope objective at 20mm is thus not sufficient.

This can be solved by designing lenses which are thinner. The lens holders are 12.7mm in diameter. A plano-convex silicon lens with a diameter of 12.5mm, a radius of curvature at 6.25mm, and a center thickness of 6.25mm will fit within the lens holder. With such a lens there will be about 1mm clearance from the membrane to the silicon lens. The pellice can also be a bit misaligned, meaning that the light beam does not hit the center of the pellice. This way the microscope objective is closer to the pellice and the clearance for the silicon lens increases. This is illustrated to some degree in figure 8.1 where the pellicle is shifted a bit toward the lower right corner. Having enough clearance for the lenses is important so the reference lens doesnt block the light path for the sample lens.

Aliasing
Chippings with too large angles introduce aliasing as discussed in section 7.4. If the angle of the chipping can be roughly estimated, this information could be used to 'unwrap' the aliased frequencies. This is possible because the frequency spectrum repeats itself. If the angle is $> 6.43°$ and a frequency is detected on the camera, the frequency has several aliases at higher frequencies. Knowing roughly what angle is measured, it is possible to tell which alias the detected frequency belong to.

A rough estimate of the depth of a chipping may be obtained by scanning the coherence layer through the chipping. Measuring the envelope of the interference pattern in each pixel, will provide information about the depth of the chipping.

This is the same technique used in optical coherent tomographt (OCT). A narrow coherence layer is preferred for this configuration as it results in a high axial resolution.

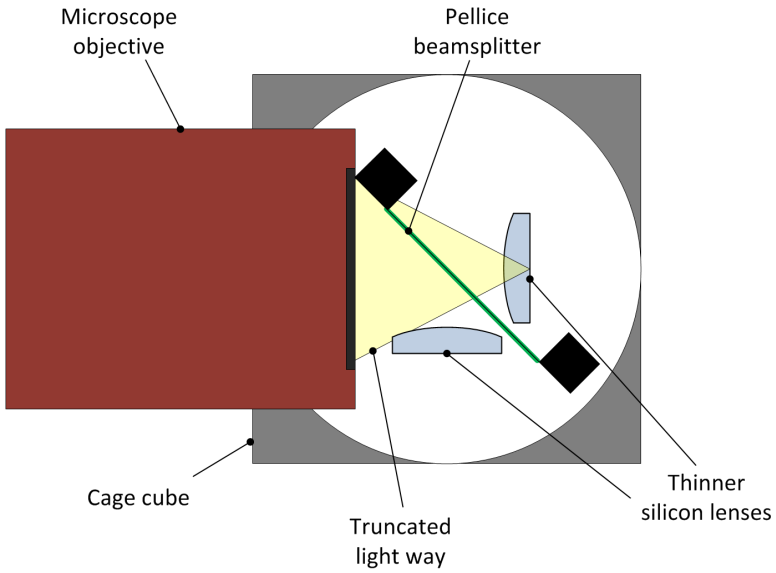

Figure 8.1: Figure shows a draft of the cage system with the pellicle beamsplitter in the center and the thinner lenses at each side. The pellice reduces aberration and the lenses are designed thinner for space clearance.

9 Conclusion

An interferometer for in-situ characterization of the silicon wafer sawing process in a lab environment has been developed. The interferometer is based on low coherence interferometry with a near infrared illumination source. The near infrared illumination makes it possible to image the process of silicon deformation from the inside as silicon is transparent for this wavelength. The interferometer is used to obtain in-situ phase maps of the deformation which can be used to quantify the size and depth of potential chipping.

The silicon sample is viewed through a microscope objective as the deformations under investigation are in the micrometer range. A silicon solid immersion lens was implemented into the system to increase the spatial resolution. The spatial resolution is dependet on the effective wavelength and numerical aperture of the microscope objective. The depth of focus is dependent on the spatial resolution, and there is thus a trade-off between these two parameters. The lower limit where silicon still is transparent is at $1250nm$ and a source with a wavelength of 1280nm was chosen to approach this limit.

The theoretical estimates gave an optical spatial resolution of $0.6\mu m$, depth of focus of $0.7\mu m$ and a coherence length of $4.1\mu m$. The depth of focus thus defines the axial resolution of the system. The coherence length and depth of focus have not been measured quantitatively in this thesis. An indent with a known depth has been used to qualitatively check the coherence layer. It could be seen that the coherence layer covered the whole depth of the indentation. The optical spatial resolution was measured to $0.8\mu m$. For interferometric measurements with the beamsplitter present, the spatial resolution then dropped to $1.5\mu m$. The beamsplitter thus reduces the spatial resolution by approximately a factor of two.

The phase maps from several Vickers indentations showed that the LCI setup is able to detect chipping and emerging cracks in-situ. Three samples have been exposed to the Vickers indenter. Two of the samples are cut in the (100) direction and the last is cut in the (111). The indentation in the (100) plane proved to be different than indentation in the (111) plane. One of the indentations in the (100) plane was done with the corners of the Vickers aligned with the lattice direction, while the other was performed with a misalignment between the Vickers and the lattice direction. With the corners misaligned chipping occurred when the Vickers was released from the sample. When aligning the Vickers a large deformation occurred at an early stage, and no chipping was observed on release.

Calculations of the depth of a chipping using the recorded phase maps have been shown. The calculations did not agree with the depth profile from the con-

focal microscope. This was because the angle of the chipping was too large and the interference fringes could not be resolved. Aliased frequencies were hence present in the image. The calculations proved that the setup has limitations on the steepness of the chippings and this limitation is dependent on the spatial resolution. If the angle of a chipping is above 6.4° aliasing will occur. For smaller angles the setup can be used to characterize small deformations in silicon.

In other areas of the indentation the phase response can be interpreted several ways. The phase map in these areas may contain false information due to multiple reflections, abrupt surfaces and phase shift due to total internal reflections. Consequently the whole topography of the indentation is not readable. The present version of the setup is best suited for inspection of chipping and has its limitations if the chipping is too steep or has an abrupt surface.

Further improvement of the optical setup is needed for clearer images. Improvement of the indentation device is also needed. Cooperation with other departments which have experience with indentation is of value for development in the right direction. There exist advanced machines for indentation, and the Vickers indent in this setup is built mostly to provide a proof-of-principle for the setup.

References

[1] M. Rinio H.J. MöllerT, C. Funke and S. Scholz. Multicrystalline silicon for solar cells. *Thin Solid Films 487 p179 to 187*, 2005.

[2] Tomoko Haraguchi Masaki Tanaka, Kenji Higashida. Microstructure of plastic zones around crack tips in silicon revealed by hvem and afm. *ScienceDirect*, 2003.

[3] Kay Gastinger and Lars Johnsen. Near infrared low coherence speckle interferometry (nir-lcsi) as a tool for the investigation of silicon in solar cell production. *SPIE*, 7387, 2010.

[4] Bahaa E. A. Saleh and Malvin Carl Teich. *Fundamentals of Photonics*. John Wiley & Sons, Inc., second edition, 2007.

[5] Karl Rottmann. *Matematisk formelsamling*. Spektrum Forlag, 2003.

[6] Wolfgang Drexler and James G. Fujimoto. *Optical Coherence Tomography Technology and applications*. Springer, 2008.

[7] Brett E. Bouma and Guillermo J. Tearney. *Handbook of Optical Coherence Tomography*. Marcel Dekker, Inc, 2002.

[8] Eugene Hecht. *Optics*. Addison Wesley, fourth edition, 2002.

[9] Olympus microscopy resource center. `http://www.olympusmicro.com/primer/anatomy/immersion.html`, 2011.

[10] S.M. Mansfield and G.S. Kino. Solid immersion microscope. *Appl. Phys. Lett.*, 57, 1990.

[11] James B. Pawley. *Handbook of Biological Confocal Microscopy*. Springer Science+Business Media, LLC, third edition, 2006.

[12] James C. Wyant. `http://www.optics.arizona.edu/jcwyant/Optics505(2000)/ChapterNotes/Chapter09/phaseshiftinginterferometry.pdf`. 2011.

[13] Geir Ove Rosvold. Fast measurements of phase using a pc-based frame grabber and phase stepping technique. 1989.

[14] Katherine Creath. Phase-shifting speckle interferometry. *Appl. Opt*, 24, 1985.

[15] Maurizio Vannoni, Marcelo Trivi, and Giuseppe Molesini. Phase-shift interferometry with a digital photocamera. 2007.

[16] M.V. Mantranadi and D. Malacara. *Optical shop testing*. Wiley-Interscience, 2007.

[17] Oxford instruments electron backscatter diffraction. `http://www.ebsd.com/ebsd-explained/`, 2011.

[18] Brent L. Adams David P. Field Adam J. Schwartz, Mukul Kumar. *Electron Backscatter Diffraction in Material Science*. Springer Science+Business Media, 2009.

[19] John G. Proakis. *Digital signal processing - Principles, Algorithms and Applications*. Pearson Prentice Hall, fourth edition, 2007.

[20] Thorlabs. `http://www.thorlabs.com`, 2011.

[21] Superlum. `http://www.superlumdiodes.com`, 2011.

[22] Xenixs. `http://www.xenics.com`, 2011.

[23] Vickers hardness test. `http://www.gordonengland.co.uk/hardness/vickers.htm`, 2011.

[24] National Instruments. Labview. `http://www.NI.com/labview/`, 2011.

[25] Ove Simonsen. Characterization of solar cell wafers using nir-interferometry. Master's thesis, NTNU, 2010.

[26] Steven W. Smith. *The Scientist and Engineer's Guide to Digital Signal Processing*. http://www.dspguide.com, 1998.

[27] Ove Simonsen Astrid Aksnes Kay Gastinger, Lars Johnsen. Inspection of processes during silicon wafer sawing using low coherence interferometry in the near infrared wavelength region. *Proc. SPIE*, 8082, 2011.

[28] A. George. Properties of crystalline silicon. *Emis Datareview Series No. 20*, 1999.

[29] Gerald C. Holst. What causes sampling artifacts? *Proc. SPIE*, 6941, 2008.

A Appendix

A.1 Paper

Inspection of processes during silicon wafer sawing using low coherence interferometry in the near infrared wavelength region

Kay Gastinger[(1)*], Lars Johnsen[(2)], Ove Simonsen [(3)], and Astrid Aksnes [(3)]

[(1)] NTNU NanoLab, 7491 Trondheim, Norway, [(2)] SINTEF IKT Optical measurement systems and data analysis, 7465 Trondheim, Norway, [(3)] NTNU, Dept. of Electronics and Telecommunications, 7491 Trondheim, Norway

ABSTRACT

Multi-wire sawing of silicon wafers is a tribological process. Slurry consisting of small silicon carbide particles embedded in polyethyleneglycol carries out the abrasive material removal process. During this process small silicon chips are removed from the bulk material. Low coherence interferometry (LCI) is widely used for high accuracy surface topography measurements of materials. This paper presents an application of LCI where the surface of a material (silicon) is inspected from the inside. Light in the near infrared (NIR) wavelength region is used. High spatial resolution is necessary to be able to observe the processes on the micro scale. Therefore a modified solid immersion approach is suggested. That makes it possible to reach a spatial resolution in the range of the illumination wavelength. The topography changes produced by the chippings are in the range of some micrometers. To be able to estimate the volumes of the Si chippings interferometric phase measurements are applied.

Keywords: low coherence interferometry¸ NIR interferometry, solar cell inspection, tribology, solid immersion

1. INTRODUCTION

Silicon (Si) wafers for photovoltaics (PVs) are today mainly produced by multi-wire sawing, where silicon blocks are cut into wafers of about 150-180 µm thickness. The sawing process introduces surface defects on the wafers. This generates a surface roughness in the micrometer range and micro-cracks propagating into the Si material. These cracks can lead to breakage further down the production line. This production step is thus one of the most critical processes in the solar cell production.

The wire sawing process depends on a sawing liquid (slurry) consisting of cutting particles (Silicon Carbide - SiC) and a carrier (polyethyleneglycol - PEG). Wafer sawing is thus an abrasive cutting process.

Wafer sawing technology is today mainly based on empirical knowledge. The lack of fundamental knowledge and understanding of the microscopic cutting processes in the sawing channel are major drawbacks for further developments and optimisations in the PV industry.

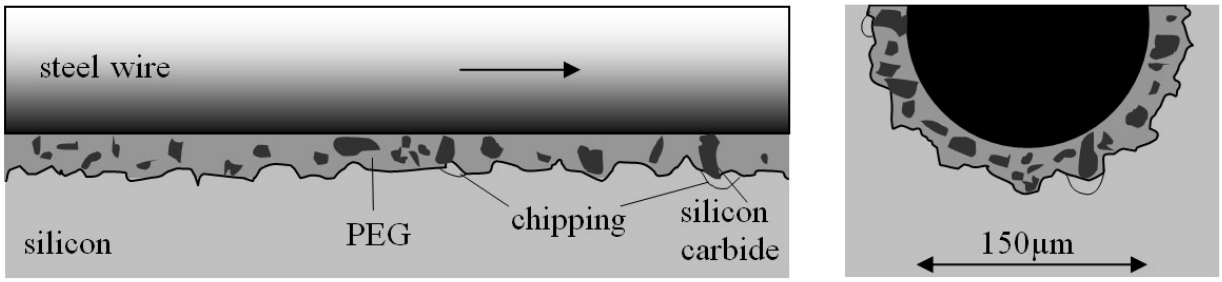

Figure 1 Description of the microscopic sawing process during multi wire sawing of silicon. Left: The steel wire moves with high velocity (typ. 12m/s) through the sawing channel. The silicon carbide particles in the sawing liquid get squeezed between the wire and the silicon surface. This process generates small indents on the silicon surface leading to micro-cracks and the removing of small silicon chippings. Right: cross section of the sawing zone

* phone +47 73590457, email: kay.gastinger@sintef.no

Optical Measurement Systems for Industrial Inspection VII, edited by Peter H. Lehmann, Wolfgang Osten, Kay Gastinger, Proc. of SPIE Vol. 8082, 80820U · © 2011 SPIE
CCC code: 0277-786X/11/$18 · doi: 10.1117/12.889498

Modelling of the sawing process is rather sophisticated due to the necessity of a multi parameter approach. A widely accepted theory is that the SiC particles introduce micro-cracks in the Si material. These cracks propagate and lead to chipping of the Si. For optimisation of the wafer quality a better understanding of this abrasive process is necessary [1,2]. Fig 1 illustrates the microscopic processes in the sawing channel. The diameter of the wire is about 150µm. the mean size of the SiC particles is about 10µm.

Optical inspection can contribute to increase basic knowledge and thus simplify the models of the abrasive process. Since the chipping area generated during indentation of the SiC particles is in the range of 10-20µm, microscopic techniques with high spatial resolution are essential.

High purity Si is nearly transparent for light with wavelengths in the range 1.25µm to about 6µm. Silicon has a high refractive index. In the near infrared range (1.25µm – 1.7µm) the refractive index is approximately given by n_{Si}= 3.5.

Following the Abbe criteria, the maximum obtainable resolution in an optical microscope with a numerical aperture of NA=0.5 is $\Delta x = 1.22\lambda$ in air. This results in a rather low spatial resolution of 1.5µm. In addition, the effective numerical aperture is limited by the refraction of the light beams when exiting the plane surface of the Si material.

In microscopy the concept of immersing the microscope objective in an index matching liquid is well established. Immersion increases the resolution of a microscope objective by removing all refractive interfaces. The concept of solid immersion was developed in the 1990's. The first solid immersion microscope was introduced by Mansfield and Kino [3]. Immersion is here realised by placing a lens with a high refractive index close to the object under investigation. Mansfield and Kino also suggested this method for examining features inside silicon. Using principles from Born and Wolf [4], a second type of solid immersion lens was demonstrated by Davidson [5]. Here an even larger viewing angle is obtained and consequently improves the resolution further. This approach of solid immersion reduces the depth of focus and is not well suited for the here presented application where not only spatial details, but also depth details are under investigations. The current paper presents a modified approach to solid immersion. The purpose of this work is the study of features inside the Si material. A tailor made plano-convex Si lens can thus be used to realise "immersion" as well as being the test sample itself. Initial attempts to increase the spatial resolution using this concept are presented by Gastinger and Johnsen [6,7]. Here, the spatial resolution is increased by a factor of 3.5 by the use of a silicon solid immersion lens since the investigated phenomena occur inside the silicon material.

The thickness of the Si chippings is expected to be up to 5µm. Thus high z-resolution is required to estimate the chipping volume. Low coherence interferometry is a well-known technique for high resolution measurements of surface topography with accuracy down to the nm range. We thus present in this paper a NIR low coherence interferometer for measurement of the volume of the Si chippings.

2. THEORETICAL BACKGROUND

For describing the theoretical aspect, theory from microscopy and interferometry has to be considered. To optimise the measurement system theoretical investigations presented for full-field optical coherence tomography systems can be used [8]. The properties and challenges of these systems are similar. Tuning the right parameters to optimize the system is crucial for the application.

2.1. Imaging system

There are several criteria for defining the resolution limit. A commonly used expression for the spatial resolution is [8]:

$$\Delta x = \frac{4\lambda_c}{\pi}\frac{1}{2NA} \tag{1}$$

where NA is the numerical aperture and λ_c is the central wavelength. The numerical aperture is defined in the medium as sin(Θ) where Θ is the half angle of the collected light cone.

To obtain high spatial resolution a low center wavelength of the light source and high numerical aperture of the microscope objective are desired. A wavelength of 1280nm was chosen to meet the requirements of transparency in

silicon and to obtain high spatial resolution as seen from equation 1. To further enhance the optical resolution the numerical aperture can be increased.

The features inside the silicon material are imaged using a microscope objective with NA = 0.4. Imaging through a plane Si surface (n_{Si}=3.51) will only collect light that emerges from the object with an angle within 6.54°. Light above 6.54° will be refracted away from the microscope objective. Total internal reflection occurs at 16.55° as seen in figure 2a). The numerical aperture inside the Si material is thus $NA_{Si} = 0.11$. However since the effective centre wavelength of the light source in Si is λ_{Si} = 366nm the limited spatial angle of the light cone is compensated by the lower effective wavelength inside the silicon.

The theoretical resolution of surface and subsurface imaging is thus the same: $\Delta x_{air} = \Delta x_{Si} \approx 2.1\mu m$.

For traditional microscopy, liquid immersion is a known method for improving the spatial resolution. Choosing a liquid immersion with a refractive index equal or close to the index of the material will eliminate the refraction at the immersion / material interface, as shown in figure 2b). A larger part of the light cone will be collected by the microscope and increase the numerical aperture and hence improve the resolution.

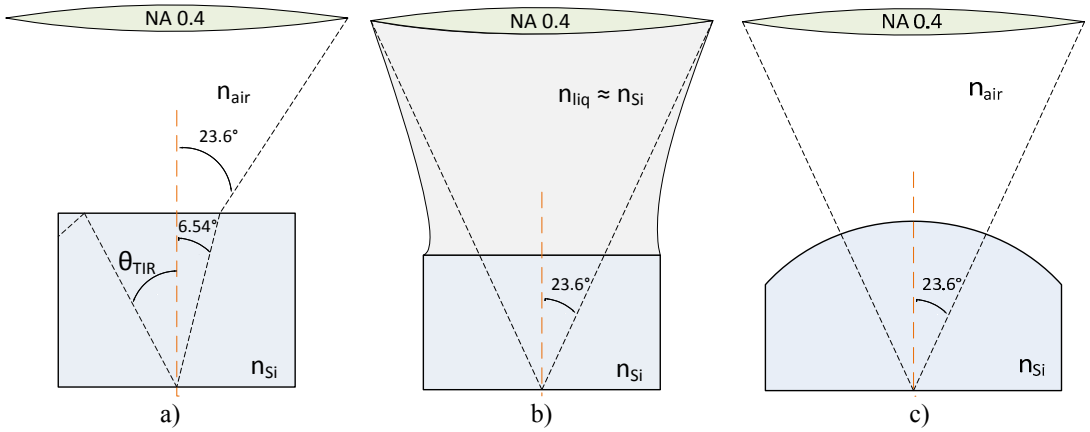

Figure 2 Illustrating different microscopy techniques. (a) conventional subsurface microscopy in Si where total internal reflection (TIR) occur at 16.55°, (b) liquid immersion and (c) solid immersion.

As there are no immersion liquids with a high enough refractive index to match silicon, another type of immersion has to be used. Forming the top surface of the silicon block as a lens will cause the rays emerging from the object to have a normal incidence to the silicon / air interface as seen in figure 2c). This is known as solid immersion and refraction at the interface is avoided. Implementing solid immersion for improved resolution for internal imaging of silicon sawing was proposed by Gastinger and Johnsen [6]. In an ideal situation all rays of light have close to normal incidence to the interface and the paraxial criterion is satisfied. Thus spherical and chromatic aberrations are eliminated. The lens thickness has to be fitted to the radius of curvature and must be adapted to the working distance of the microscope objective.

With solid immersion the effective numerical aperture is unchanged, $NA_{air} = NA_{Si} = 0.4$., but the effective wavelength is decreased with a factor *n.* Hence the spatial resolution is increased with a factor n, $\Delta x_{Si} \approx 0.6\mu m$.

The calculated resolutions assume an ideal situation where the lens is perfect. This may not be the case, and the lens can have an error in the convex part which makes an error in the curvature of radius. This can lead to a displacement of the optical axis, meaning that the field of view is not at the center of the lens, and hence the resolution is altered. If the curvature is not perfect, the focus may not be exactly at the planar surface of the silicon lens. This also results in reduced resolution.

The depth of focus is the optical depth resolution and is defined in equation two as two times the Rayleigh range z_r [8],

$$\Delta z_{opt,Si} = 2z_r = \frac{2\lambda_{c,air}}{n_{Si}\pi NA^2} \quad (2)$$

Applying the parameters given above the depth of focus is calculated to be $\Delta z_{opt,Si} = 1.4\mu m$.

2.2. Interferometer system

Low coherence interferometry (LCI) is widely used for the high accuracy inspection of the topography of surfaces [9]. Commercial systems obtain diffraction limited spatial resolution and nanometer resolution of the 3D height profile. Optical Coherence Tomography (OCT) systems [10] enable the measurement of the inner structure of an object. The lateral and depth resolution of commercial systems is specified in the range of 1-50µm, depending on the spectrum width of the low coherent light source.

Figure 3 shows the basic configuration of a low coherence interferometer. For simplicity a Michelson configuration is shown. The light from a low coherence light source (i.e. a superluminescent diode) is divided into an object and a reference beam. In the reference beam the light is reflected by a moveable reference mirror. In the object arm the light is reflected by the object. The returning beams interfere in the beam splitter and the interference signal is detected by a detector (i.e. a camera). The technique utilises the temporal coherence of a broad band light source. Interference occurs only for object light having an optical path length difference (PLD) within the coherence length of the source. Thus the probing depth can be selected by translating the reference mirror. In figure 3 two cases are illustrated. The solid line shows the coherence layer adjusted at the object surface, while the dashed line shows the probing of the object backside.

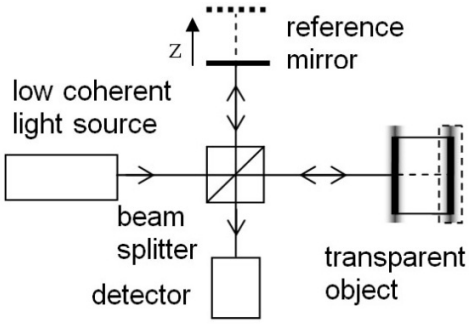

Figure 3 Michelson type low coherence interferometer

The measurement of the chipping volume can be carried out with algorithms known from interferometric deformation measurement based on phase shifting [11]. First the coherence layer is adjusted at the interface of interest. By subtracting the phase map of the chipping area before and after the chipping process, the change of the 3D surface profile and thus the chipping volume can be determined.

This algorithm can be applied to plane surfaces but also to rough surfaces. At rough surfaces speckles occur. The corresponding technique has been introduced as Low Coherence Speckle Interferometry [12].

The depth resolution of a low coherence interferometer consists of two factors. Both the depth of focus of the imaging system and the coherence length of the LCI system have to be evaluated. For systems with low numerical aperture the depth of focus may exceed the coherence length of the system. For such systems the wavelength and the coherence length decide the depth resolution. A commonly used expression for the coherence length for a source with a Gaussian spectrum is [8]

$$\Delta z_{c,Si} = \frac{2ln2}{n_{Si}\pi}\frac{\lambda_{c,air}^2}{\Delta\lambda},$$

Where $\Delta z_{c,Si}$ represents the FWHM of the LCI system and $\Delta\lambda$ is the FWHM of the source. As we are working inside silicon both λ_c and $\Delta\lambda$ have been scaled with the refractive index, n_{Si}.

For high NA the depth of field may be shorter than the FWHM of the coherence length of the interferometer system. Then the depth resolution given in equation (2) is valid for the axial resolution of the interferometer system. The coherence length of the system is calculated to be $\Delta z_{c,Si} = 6.2\mu m$. Considering the depth of focus $\Delta z_{opt,Si} = 1.4\mu m$ we can see that the axial resolution of the system is given by the depth of focus. This means that the components which are out of focus still contribute to the interference signal, but have a reduced spatial resolution.

Depending on the application, high or low axial resolution is desired. Examining the tomography of a silicon wafer after sawing requires a fine axial resolution which can be realized by a source with a broad spectrum. For in-situ investigations the depth of field and coherence length are required to be sufficiently long to cover the whole surface tomography. As the application requires high-resolution images over a wide object depth a trade-off between the depth of focus and the spatial resolution is necessary.

3. EXPERIMENTAL SETUP

In this work an imaging Linnik type interferometer was built for in-situ investigation of the tribological processes involved in multi wire sawing of silicon wafers. For in-situ investigation the setup was designed to view the process from the inside of the material relative to the sawed surface. To avoid absorption in Si it is necessary to work at wavelengths longer than about 1240nm. To compensate for the long optical wavelengths and still achieve high lateral resolution solid immersion is utilised in the imaging system. A sketch of the interferometer setup is shown in figure 4.

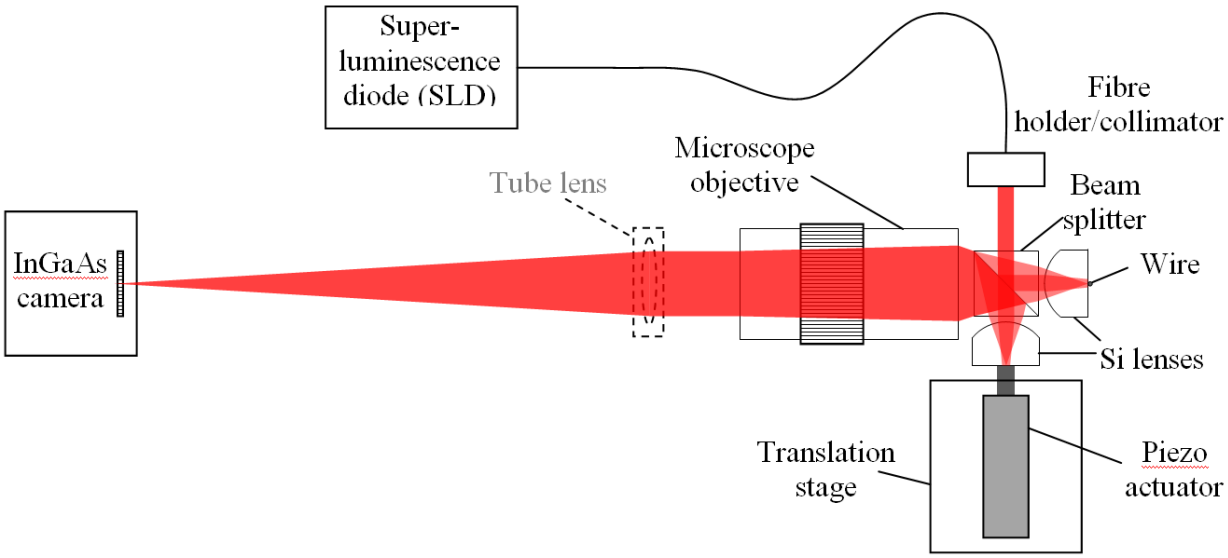

Figure 4 A sketch of the Linnik type interferometer setup is shown. (The tube lens necessary for the microscope objective to work in infinity corrected mode was not present in the experiments published here).The abrasive operation is performed on the object silicon lens. An identical Si lens is used to balance the optical path in the reference arm. The planar silicon/air interface (30% reflection) of the plano-convex silicon lens is utilized as reference mirror.

The illumination source is a fibre coupled superluminescent diode (SLD), Superlum S1300, operating at a centre wavelength of 1280nm with a spectral width of 34nm (full width half maximum). At the fibre output the beam is collimated before it enters the NIR-optimized 50/50 beam splitter cube (15x15mm). The object is a custom made plano-convex Si lens (R=8mm, t_{centre}= 8mm, AR on convex side) chosen to facilitate high resolution through solid immersion optics.

When working in the centre of curvature of the silicon lens both spherical and chromatic aberrations are minimized (at the optical axis) as all rays in the imaging path are perpendicular to the silicon lens surface. An identical silicon lens is used in the reference arm to achieve a balanced interferometer setup. The planar silicon-air interface (30% reflection) is used as reference mirror surface. The reference is mounted on a manual positioning stage for alignment (angle and z-position) and a piezo stage is incorporated for phase shifting and short range scanning. A Mitutoyo M Plan Apo NIR (20x, NA 0.4, working distance 20mm) is used in the imaging arm. For image capture a Xenics Xeva-1.7 InGaAs camera is used. The camera resolution is 640x512 pixels (20µm pixel pitch) and the maximum frame rate is 15fps at full resolution.

The left image in figure 5 shows a close-up of the Linnik interferometer. The interferometer is built in a compact and robust configuration to avoid the influence of mechanical vibrations on the interferometric measurements. The right image in figure 5 shows the silicon lens photographed on a mirror to visualise its plano-convex shape.

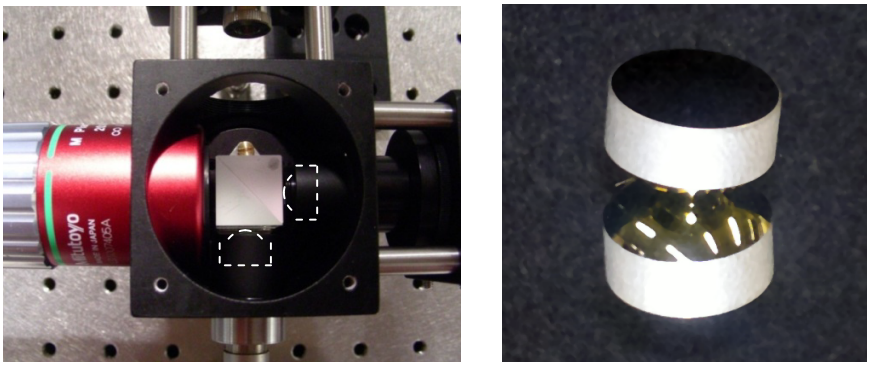

Figure 5 Details of the Linnik interferometer, left: The interferometer setup with the beam splitter cube in the centre of the picture. The position of the silicon lenses are indicated in the image with white dashed lines. right: the custom made silicon lens (positioned on a mirror) used as reference and object.

4. EXPERIMENTAL RESULTS

This chapter presents results of investigations of the spatial resolution of the imaging system. The resolution measurements were carried out with and without the silicon lens present to highlight the effect of the solid immersion lens. Furthermore phase measurements obtained at a real sawing channel will be presented. These measurements demonstrate the proof-of-principle for the interferometric investigation of the chipping process.

4.1. Resolution measurements of a USAF resolution chart

No standard resolution chart was available to test the spatial resolution for the Si-internal imaging system shown in figure 4. Therefore the setup given in figure 6 was used to get an estimate of the resolution and investigate the influence of the Si lens.

A 1951 USAF high resolution chart was imaged with and without the silicon lens. Due to the fact that the resolution chart is too large to fit in the original system, the measurements were carried out in a separate setup shown in figure 6. A tungsten halogen lamp which has a broader wavelength spectrum than the SLD was used for background illumination. The tungsten halogen lamp works as gray body radiation and was driven to approximately 3200K. The spectral response curve of the illumination/camera combination is the product of their respective response curves. Operating without the silicon lens the centre of gravity of the resulting response curve is approximately 1260nm which is close to the SLDs centre wavelength.

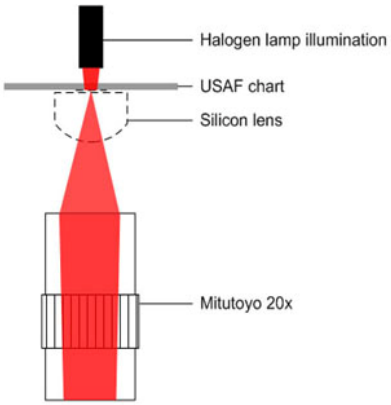

Figure 6 Illustration of the setup used for investigations of spatial resolution

For imaging through the silicon lens the 900-1240nm band is absorbed. This means that the centre of gravity of the response curve of the illumination/camera combination is approximately 1460nm and a slightly poorer resolution than with the SLD is expected. The effective wavelength is thus longer with the silicon lens present. Still increased resolution due to the increasing numerical aperture caused by the silicon lens is expected.

Figure 7a shows the spatial resolution of the imaging system without the Si lens in place. Considering the horizontal elements in figure 7a, the smallest element which still has a modulation amplitude of 10% of the normalized dynamic range is in group 8 element 2 (upper left element in column 8). An intensity plot of this element is given in figure 8a. This element has a pitch of 3.5µm which defines the resolution of the system. Inspection of the vertical resolution in figure 7a reveals that the amplitude of the signal has dropped to 10% already at the largest element in group eight (lower right in the zoomed image). This corresponds to a vertical resolution of 3.9µm.

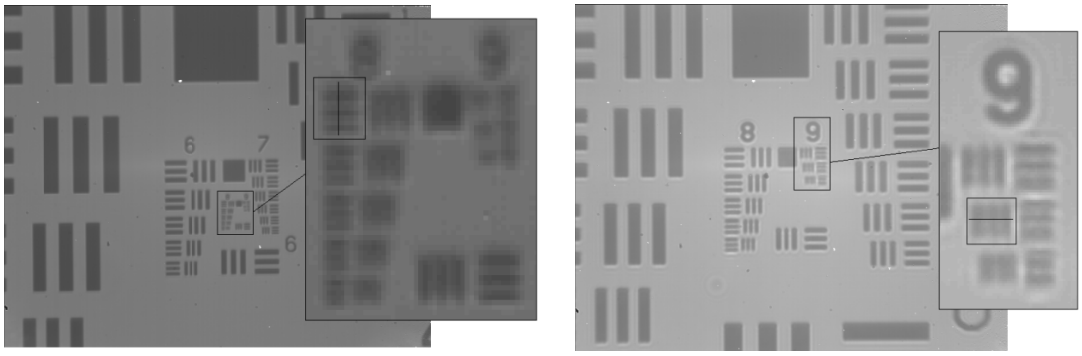

a) b)

Figure 7 Results of the resolution measurement with magnified high resolution charts (group 8 and 9) recorded (a) without silicon lens and (b) with the silicon lens in place. The elements with the highest spatial resolution are marked with a square in the magnified groups

The USAF resolution chart is imaged through the silicon lens is shown in figure 7b. The magnification of the imaging system is increased to 66x. The smallest resolved vertical element is found in group 9 element 2. The signal amplitude of this element is plotted in figure 8b and shows that the imaging system including the Si lens has a resolution better than 1.7µm. The horizontal resolution is the same as the vertical resolution for this case.

The magnification and resolution is clearly improved by including the Si lens in the setup. As the USAF resolution chart was resting on the silicon lens, an air gap between the lens and the chart is present. If this air gap is large enough, refraction at the silicon/air surface may introduce spherical aberration which reduces the resolution. This effect has not been accounted for. It has to be considered that the camera pixel resolution in image 7b) is much higher than in 7a).

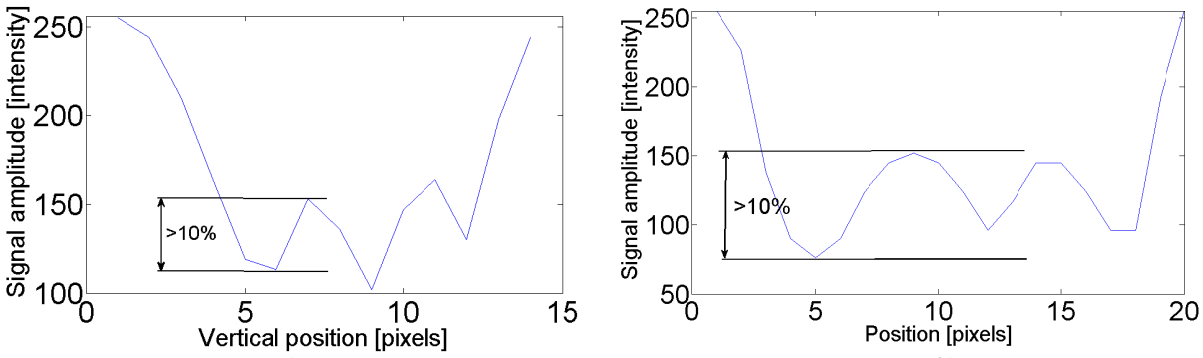

a) b)

Figure 8 Plot of the intensity amplitude from the resolution measurements. Figure (a) corresponds to the intensity profile along the line of the highest resolution element in figure 7a, while figure (b) corresponds to the line drawn in the highest resolution element in figure 7b.

Furthermore, the microscope objective used for the measurements is an infinity corrected objective. This means that a tube lens is required for achieving high quality imaging and optimized resolution. At the time of the measurements no tube lens was available for wavelength around 1280nm. As part of the future work in this project a suitable tube lens will be included in the system.

4.2. Interferometric measurements of the sawing channel

To simulate the sawing process, the plane surface of a silicon lens was cut with a sawing wire. This resulted in a sawing channel used as a test sample for the system. The sawing channel is shown in figure 9, where the direction of the channel is almost diagonal, expanding from the lower right to the upper left corner. These measurements were carried out with the SLD as a light source. The field of view is approximately 210µm x 170µm.

a) b) c)

Figure 9 Images of the coherence layer scanned through the sawing channel. Coherence layer placed (a) at the plane Si lens surface, (b) at the edges of the sawing channel (area 1 and 2) and (c) at the bottom of the sawing channel (area 3).

An image where the coherence layer is placed on the planar surface of the silicon lens is shown in figure 9a). The coherence layer is then scanned longitudinal to the optical axis along the sawing channel. Images showing the coherence layer at the sides and at the bottom of the sawing channel are shown in figure 9b) and c), respectively. Areas within the coherence layer are marked by dotted lines. The sawing channel has a rough surface and the interference pattern is therefore not seen as a fringe pattern as it is on the planar surface in figure a). The sawing channel is rather deep, and the coherence layer is not thick enough to cover the whole depth of the channel. The results demonstrate the system's ability to isolate specific depths of the sample to perform measurements on. Improved depth resolution can be achieved by exchanging the light source of the system. The InGaAs camera has a detection range from 0.9µm to 1.7µm which offers the opportunity to use a source with much broader spectrum. This will narrow the coherence layer and improve depth resolution for a more precise investigation of the sawing channels tomography.

4.3. Phase measurements

As described earlier, the reference arm of the interferometer is mounted on a piezoelectric actuator. This provides the opportunity to record phase maps. Five images with a step of a quarter wavelength are captured and used to calculate the phase in each pixel using the five-frame technique [13].

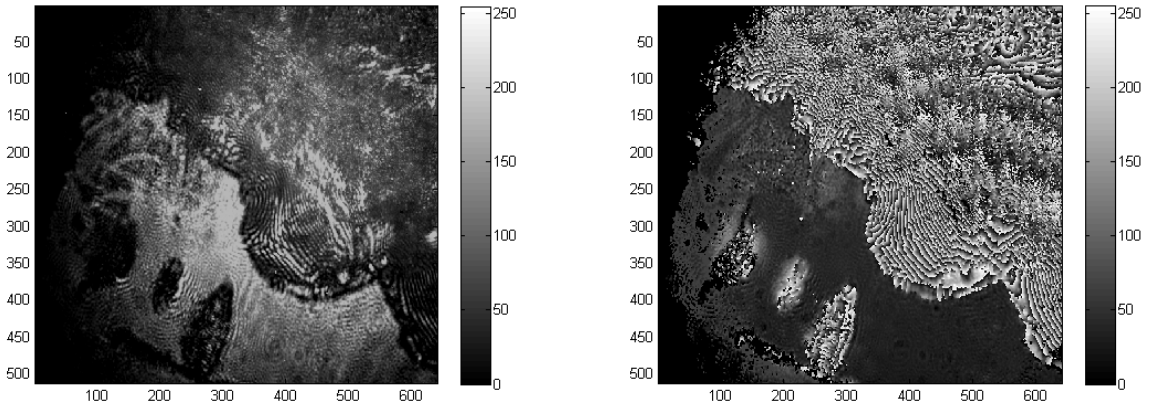

a) b)

Figure 10 Interferometric measurements at the sawing channel area. (a) interference intensity of the sawing channel and (b) mod-2π phase map of the same area

Recording several phase maps during the sawing process can be used to investigate how the sawing affects the surface. Deducting one phase map from another the deformation occurring between the two measurements is revealed. This experiment is not yet been carried out, but the principle has been demonstrated with the same system by Gastinger and Johnsen for surface measurements [6]. Figure 10a shows the surface of the sawing channel while figure 10b shows the mod-2π phase map of the same surface.

5. CONCLUSIONS

A near infrared low coherence interferometer (NIR LCI) has been developed for inspection of processes during silicon wafer sawing. A silicon solid immersion lens was utilised making it possible to reach high spatial resolution (on the order of the illuminating wavelength). The spatial resolution of the NIR LCI is dependent on the effective numerical aperture, the required depth of focus, the required magnification, and the effective wavelength in the medium. There is a trade-off between spatial resolution and depth of focus. Theoretical estimates gave spatial resolution $\Delta x \approx 0.6\mu m$, coherence length $\Delta z_{c,\,Si} = 6.2\mu m$, and depth of focus $\Delta z_{opt,\,Si} = 1.4\mu m$. Resolution measurements using an USAF chart yielded a spatial resolution $\Delta x \approx 1.7\mu m$, which is a factor 3 higher than theoretical estimates. This deviation is reasonable since a different setup is used where the object is not directly at the planar silicon surface. Furthermore contribute spherical aberrations, imperfections in the lens, and uncertainty with respect to the detected center wavelength of the halogen source to a reduction of the spatial resolution.

Proof-of-principle of the technique was demonstrated through the investigation of silicon with chippings removed from the bulk material using an abrasive cutting process. The silicon was sawed using slurry of small silicon carbide particles embedded in PEG. Features inside the Si material were studied by moving the coherence layer axially into the structure and performing measurements at specific depths. Phase measurements were performed by stepping the reference mirror a quarter wavelength and capturing the image for 5 successive steps. We present a work in progress. Future work will be to measure deformation by using these phase-stepping techniques.

In conclusion, NIR LCI is an interesting tool for studying wafer sawing and other tribological processes in transparent media. Better knowledge of the microscopic cutting processes may aid developments and optimizations in the photovoltaic industry.

ACKNOWLEDGEMENTS

Several people have contributed to the present work. Nuria Espallargas and Sergio Armado have contributed to the tribological background of this project. Ole Johan Løkberg, Arne Røyset and Gudmunn Slettemoen have given input of great value to the theoretical investigations. The authors want to thank these people for their valuable contributions. The work is partly financed by the Norwegian Research Council through the user-driven innovation project “TyWatt”.

REFERENCES

[1] Möller, H.J., "Basic Mechanisms and Models of Multi-Wire Sawing", Adv. Eng. Mater., 6 7, 502-513 (2004)
[2] Möller, H.J., et al., "Multicrystalline silicon for solar cells", Thin Solid Films, 487 (1-2), 179-187 (2005)
[3] Mansfield, S. M. and Kino, G. S.,"Solid immersion microscope" Appl. Phys. Lett. 57, 2615 (1990)
[4] Born, M. and Wolf, E., [Principles of Optics], Pergamon, Oxford, 253 (1980)
[5] Davidson, M.P., "Aplanatic microlenses and applications in the semiconductor industry", Proc. SPIE 1926, 84 (1993)
[6] Gastinger, K. and Johnsen, L., "Near infrared low coherence speckle interferometry (NIR-LCSI) as a tool for the investigation of silicon in solar cell production", Proc. SPIE 7387, 738713 (2010)
[7] Johnsen, L. and Gastinger, K., "Microscopic near infrared (NIR) imaging for investigation of the saw-channel surface during wire-sawing of silicon", 25th European Photovoltaic Solar Energy Conference and Exhibition, Valencia (2010)
[8] Bouma, B.E. and Tearney, G.J. [Handbook of Optical Coherence Tomography], Marcel Dekker Inc, NY, (2002)
[9] Harasaki, A., Schmit, J. and Wyant, J. "Improved vertical-scanning interferometry," Applied Optics 39(13), 2107-2115 (2000)
[10] Fujimoto, J. G., Drexler, W., Morgner, U. , Kärtner, F. and Ippen, E., "Optical Coherence Tomography", Opt. Phot. News, 24 (2000)
[11] Creath, K., "Temporal phase measurements methods," in Interferogram Analysis, edited by D.W Robinson and G.T. Reid, IOP Publishing, Bristol, 94-140 (1993)
[12] Gastinger, K., "Low coherence speckle interferometry (LCSI): when speckle interferometry goes sub-surface", Proc. SPIE 7008, 70081I (2007)
[13] Hariharan, P., Oreb, B. and Eiju, T., "Digital phase shifting interferometry: a simple error-compensating phase calculation algorithm", Applied Optics 26(3), 2504-2505 (1987)

A.2 Custom Parts

Vickres-Piezo adapter

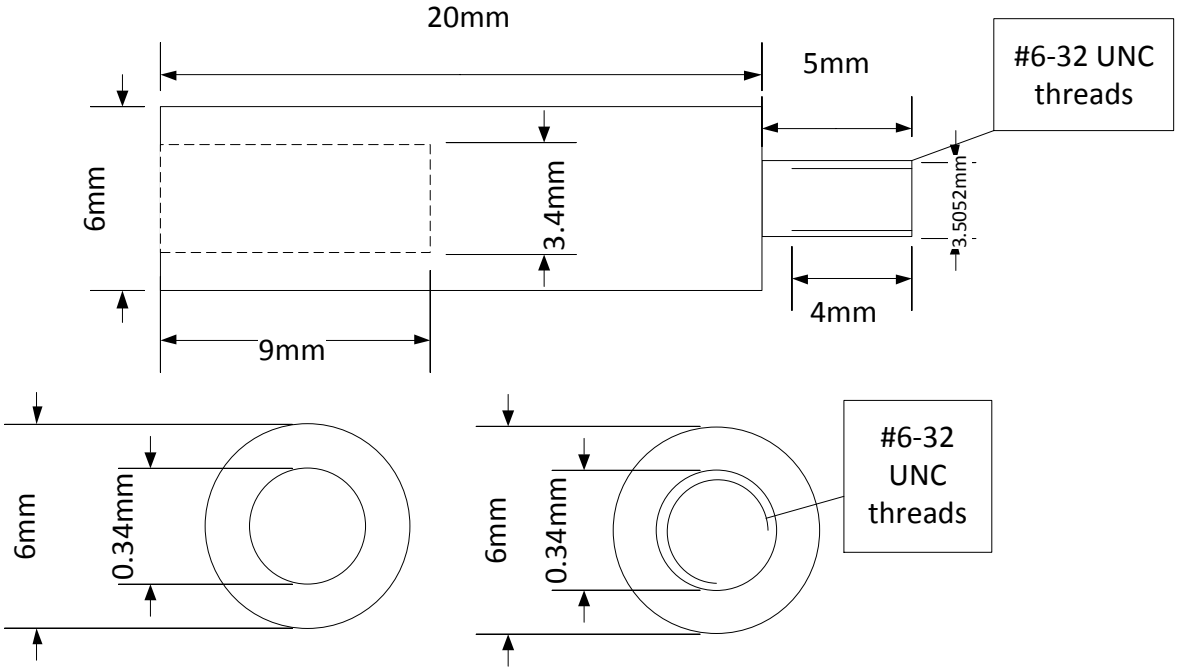

Reference lens holder

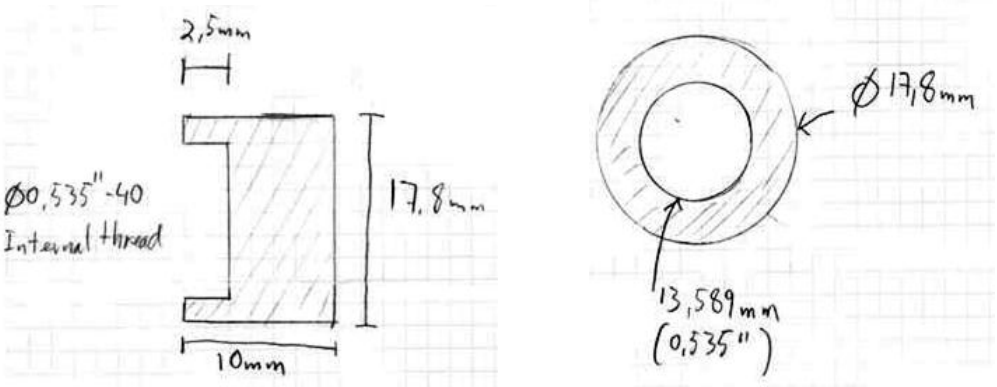

Beamsplitter stage

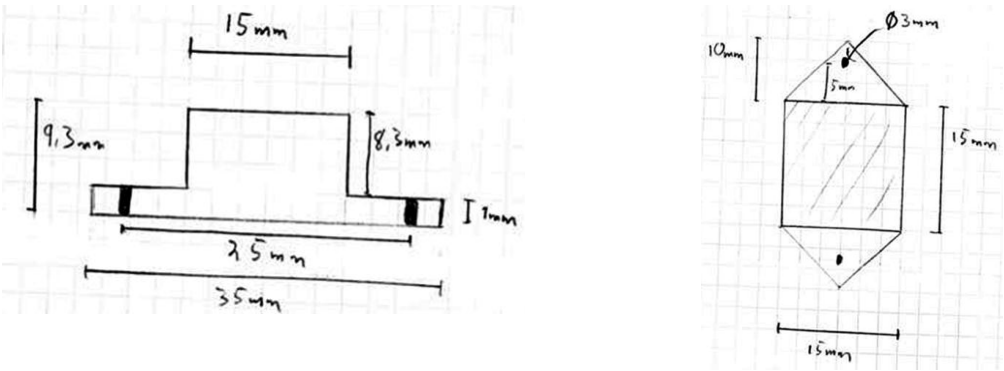

A.3 Superluminescent diode datasheet

High Output Power, Gaussian-like Optical Spectrum, Optically Isolated, Low-noise

Parameter	Device	Min	Typ.	Max
SM fiber output power – full power mode, mW	S1300-HP-I-G-B-20	15	20	-
SM fiber output power – low power mode, mW		1*	-	-
Mean wavelength, nm		1280	1290	1300
3 dB (FWHM) spectrum width, nm (full power)		45	-	-
Residual spectral modulation index (0.05 nm res), %		-	2.0	5.0
Output isolation		Built-in optical isolator (-30 dB)		
Fiber		SM, Corning SMF-28		
Output connector		FC/APC		
Long-term stability, %**		±0.5%		
Short-term stability, %***		±0.1%		

* other upon request. ** 8 hours, measurements taken every minute, 100 ms integration. *** 15 minutes, measurements taken every second, 100 ms integration. All measurements were taken after a one-hour warm-up period at ambient temperature 22±0.5 °C.

Optical Spectrum and Coherence Function

Full Power Mode

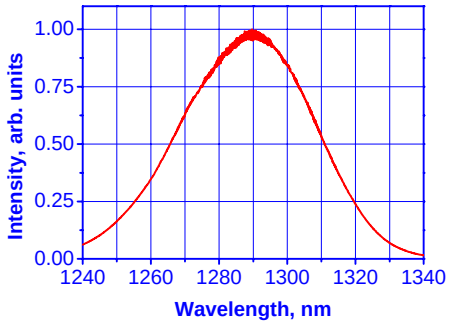

Low Power mode

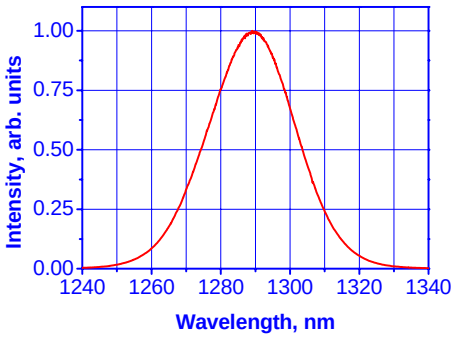

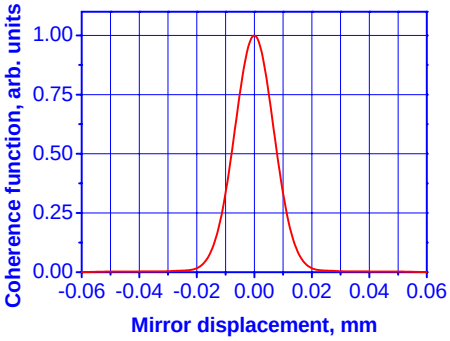

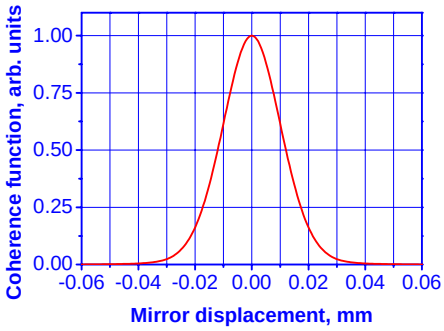

Typical RIN

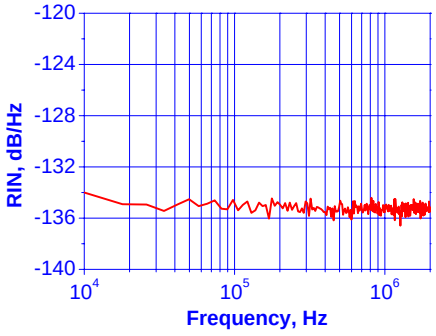

All specifications are subject to change without notice.
For more details check
http://www.superlumdiodes.com/s_broadlighters.htm.

A.4 Xenics NIR camera

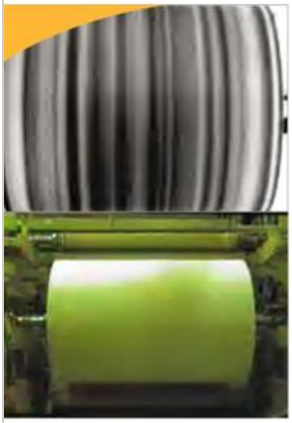

Top: tissue paper production infrared
Bottom: tissue paper production visual

Soldering iron

Solar cell inspection

Array Specifications	
Array Type	InGaAs
Spectral band	Standard: 0.9 to 1.7 µm
# Pixels	640 x 512
Pixel Pitch	20 µm
Array Cooling	TE1-cooled down to 263K
Pixel operability	> 99%
Gain	4 gain settings

Camera Specifications	Xeva 25 Hz	Xeva 90 Hz
Lens (included)		
Focal length	25 mm f/0.95	
Optical interface	C-Mount, spectrograph fixation holes (Broad selection lenses are available)	
Imaging performance		
Frame rate (full frame; uncorrected images)	25 Hz	90 Hz
Window of interest	Smallest window 8 x 128	
Integration type	Snapshot	
Exposure time range	1 µs up to 100 ms	
Noise level: Low gain High gain	7 AD counts 14 AD counts	
S/N ratio: Low gain High gain	67 dB 61 dB	
A to D conversion resolution	14 bit	
Interfaces		
Camera control	USB 2.0	
Image acquisition	USB 2.0 / CameraLink	
Trigger interface	TTL levels	
Graphical User Interface (GUI)	X-control Advanced	
Power requirements		
Power consumption	< 4 Watt, cooler: 30 Watt max	
Power supply	12 V	
Physical characteristics		
Camera cooling	Forced convection cooling	
Ambient operating temperature	0 to 50° C	
Dimensions	90 L x 110 W x 110 H mm	
Weight camera head	App. 1.8 kg	
Weight power supply	300 g	

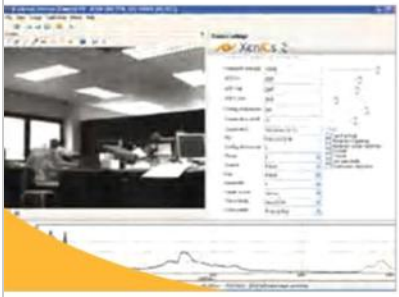

Applicable OS: Windows 2000 (SP4), XP Pro (SP2), VISTA (SP1)

X-Control Advanced	Xeneth radiometric
· Image live view · Store digital Pictures / Movies · Image histogram · Line profiles, Spot meters, Time profiles	X-control advanced features + thermography
· Black hot / White hot · False color mode with various color palettes	**Thermography studio**
· Video output format selection: PAL (CCIR) or NTSC (RS 170)	Analysis and report-generating software of real-time and static images

A dynamic link library (DLL) to communicate with the driver has been designed for flexible software development. A well-documented API with sample code in C, Visual Basic and Delphi is supplied, as well as a Linux SDK. Labview device drivers and a sample program (executable) are also available.

Product Selector Guide

Xeva-1.7-640 Part number	Digital output Interface	Cooling	Frame Rate	ADC	TrueNUC range [integration time up to]
XC137-025HZ	CameraLink	TE1	25 Hz	14 bit	50 msec
XC137-090HZ	CameraLink	TE1	90 Hz	14 bit	50 msec

Accessories

Part number	Type	Description	Available on following cameras
XC602	Trigger	Triad to BNC	All
XC606-5	CameraLink	MDR-26	All
XC503-201	Frame grabber	Xenics PCI-CL	All

Thermography Part number	Description	Available on following cameras
TH0800	Temperature calibration from 300°C to 800°C	All
TH1200	Temperature calibration from 300°C to 1200°C	All

Software Part number	Description	Available on following cameras
XERAD	Xeneth Radiometric	All
TST08	Thermography Studio	All

Inputs

Outputs

XB-004 issue 02

A.5 Mitutoyo NIR microscope objective

BD Plan Apo HR for Bright / Dark Field Observation

Order No.	Mag.	N.A.	W.D.	f	R	D.F.	View field 1	View field 2	Mass
378-845	50X	0.75	5.2mm	4mm	0.4μm	0.48μm	ø0.48mm	0.10x0.13mm	420g
378-846	100X	0.90	1.3mm	2mm	0.3μm	0.24μm	ø0.24mm	0.05x0.06mm	435g

Note:
These objectives offer extra-high resolving power.

DIMENSION

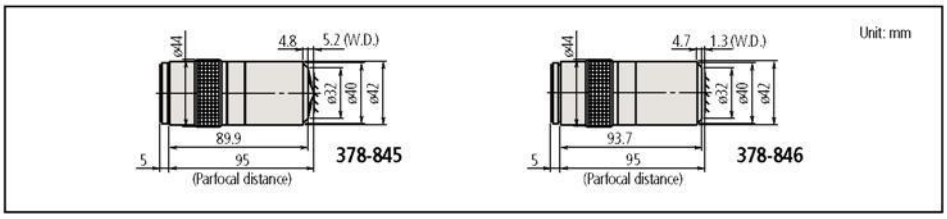

Near-infrared Radiation Corrected
M Plan Apo NIR for Bright Field Observation

Order No.	Mag.	N.A.	W.D.	f	R	D.F.	View field 1	View field 2	Mass
378-822-5	5X	0.14	37.5mm	40mm	2.0μm	14.0μm	ø4.8mm	0.96x1.28mm	220g
378-823-5	10X	0.26	30.5mm	20mm	1.1μm	4.1μm	ø2.4mm	0.48x0.64mm	250g
378-824-5	20X	0.40	20.0mm	10mm	0.7μm	1.7μm	ø1.2mm	0.24x0.32mm	300g
378-825-5	50X	0.42	17.0mm	4mm	0.7μm	1.6μm	ø0.48mm	0.10x0.13mm	315g
378-826-5	100X	0.50	12.0mm	2mm	0.6μm	1.1μm	ø0.24mm	0.05x0.06mm	335g
378-863-5	50X	0.65	10mm	4mm	0.42μm	0.65μm	ø0.48mm	0.10x0.17mm	450g
378-864-5	100X	0.70	10mm	2mm	0.74μm	0.56μm	ø0.24mm	0.05x0.06mm	450g

Note:
These objectives are designed that a workpiece's image can be focused within the focal depth even when the wavelength used is changed anywhere from the visible range (l = 480nm) up to near-infrared range (l = 1800nm). Therefore the M Plan NIR Series are suitable for laser repair. However, when the wavelength used exceeds 1100nm, the focussing position may slightly deviate from that in the visible light range due to changes in the glass dispersion and the refractive index.

DIMENSION

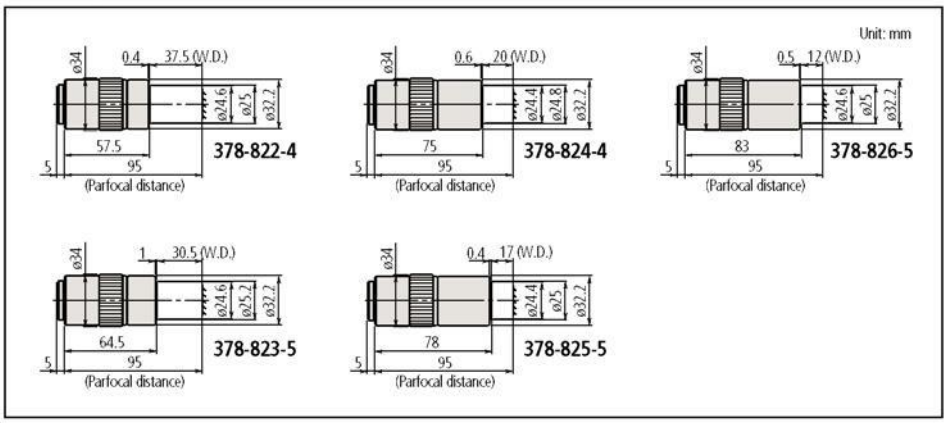

Near-ultraviolet Radiation Corrected
M Plan Apo NUV for Bright Field Observation

Order No.	Mag.	N.A.	W.D.	f	R	D.F.	View field 1	View field 2	Mass
378-817-4	20X	0.40	17.0mm	10mm	0.7μm	1.7μm	ø1.2mm	0.24x0.32mm	340g
378-818-4	50X	0.42	15.0mm	4mm	0.7μm	1.6μm	ø0.48mm	0.10x0.13mm	350g
378-819-4	100X	0.50	11.0mm	2mm	0.6μm	1.1μm	ø0.24mm	0.05x0.06mm	380g

Note:
These objectives are designed that a workpiece's image can be focused within the focal depth even the wavelength used is changed anywhere from the visible range (l = 620nm) to the near-ultraviolet range (l = 355nm). Therefore The M Plan NUV Series are suitable for laser repair using high frequency laser beam.

DIMENSION

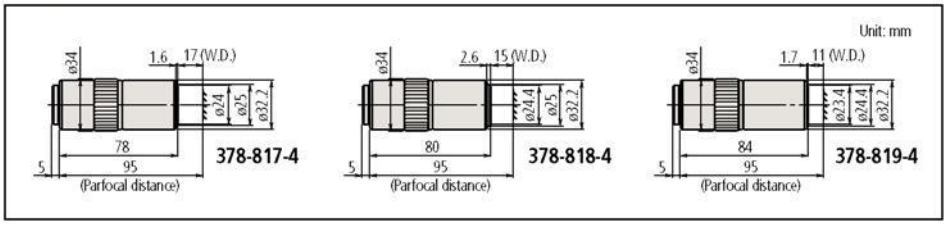

Mag.: Magnification
N.A.: Numerical aperture
W.D.: Working distance
f: Focal distance
R: Resolving power
D.F.: Focal depth
View field 1: Field of view when using ø24mm eyepiece
View field 2: Field of view when using 1/2" CCD camera

A.6 Piezoelectric actuator PAS005

Item #	PAS005	PAS009	PAS015
Travel	20 µm	40 µm	100 µm
Length	2.32" (59 mm)	3.74" (95 mm)	7.99" (203 mm)
Resolution*	20 nm	40 nm	100 nm
Capacitance	3.6 µF	7.2 µF	18 µF
Feedback	N/A		
Accuracy	N/A		
Repeatablity	N/A		
Piezo Blocking Force	1000 N at 60 V 1150 N at 75 V		
Operating Temp	-20 to 80 °C		
Piezo Input Voltage	0 to 75 V		

A.7 Piezoelectric actuator PAZ020

Piezoelectric Actuators without Feedback

Specifications
- Permanent Preload
- **Piezo Voltage:** 0 to 75 VDC
- **Drives:** Modular Drives
- **Opertating Temperature:** -20 to 80° C

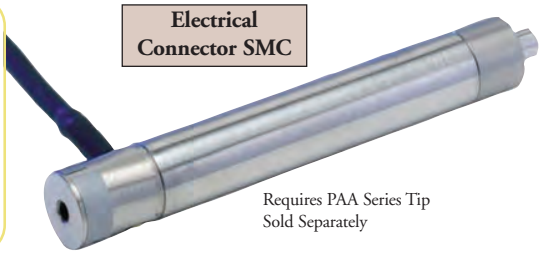

Required, Interchangeable Tips Sold Separately (Shown Below)

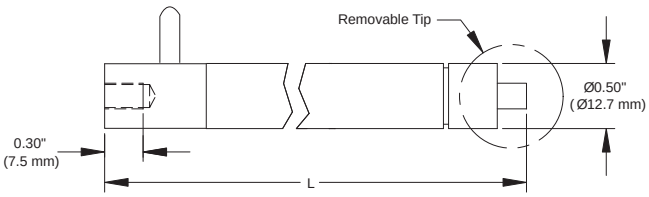

The PAS Series of Piezoelectric Actuators provide a convenient mounting package with adjustment ranges of 20 mm, 40 mm, or 100 mm. The tip of the actuator is tapped to accept any of our PAA Series Actuator Tips featured below.

Please refer to our website for complete models and drawings.

ITEM#	$	£	€	RMB	LENGTH L	TRAVEL	RESOLUTION
PAS020	$ 382.50	£ 265.20	€ 339,60	¥ 3,229.90	1.65" (42 mm)	20.0 µm	20.0 nm
PAS040	$ 565.00	£ 391.70	€ 501,70	¥ 4,770.90	2.36" (60 mm)	40.0 µm	40.0 nm
PAS100	$ 825.00	£ 572.00	€ 732,50	¥ 6,966.40	4.49" (114 mm)	100.0 µm	100.0 nm

End Tips for PAS/PAZ Series

The PAA series of actuator tips have been provided to enhance the mechanical interfacing of the PAS series of piezoelectric actuators featured above and the PAZ series featured below. These tips are precision-machined and feature a hardened steel insert for long life.

ITEM#	$	£	€	RMB	DESCRIPTION
PAA001	$ 21.00	£ 14.60	€ 18,70	¥ 177.40	Piezo Actuator Tip, Flat End
PAA005	$ 36.80	£ 25.60	€ 32,70	¥ 310.80	Piezo Actuator Tip, Ball End
PAA007	$ 24.30	£ 16.90	€ 21,60	¥ 205.20	Piezo Actuator Tip, M4 x 0.7 Threading
PAA013	$ 27.50	£ 19.10	€ 24,50	¥ 232.30	Piezo Actuator Tip, #8-32 UNC Threading

Piezo Actuators with Strain Gauge Feedback

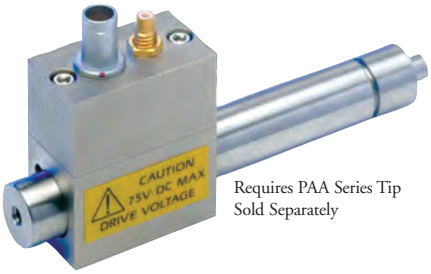

The PAZ series of piezoelectric actuators provides a wide selection of travel ranges (20 to 100 µm), the flexibility of replaceable tips, and feedback via a 7-pin LEMO connector that can be used in conjunction with our apt™ series of piezo controllers (see page 562). The Ø1/2" (Ø12.7 mm) mounting barrel provides compatibility with standard Ø1/2" (Ø12.7 mm) mounting bores.

Interchangeable Tips Sold Separately (Shown Above)

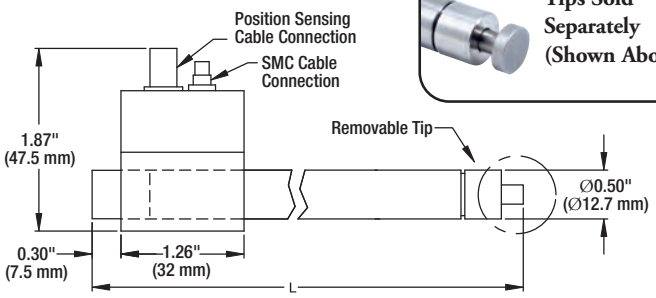

Please refer to our website for complete models and drawings.

ITEM#	TRAVEL	LENGTH L	RESOLUTION
PAZ020	20 µm	2.36" (60 mm)	5.0 nm
PAZ040	40 µm	3.07" (78 mm)	10.0 nm
PAZ100	100 µm	5.20" (132 mm)	25.0 nm

Please note that the actuators and tips are sold separately.

Piezo Actuators

ITEM#	$	£	€	RMB	DESCRIPTION
PAZ020	$ 770.00	£ 533.80	€ 683,70	¥ 6,501.90	Piezoelectric Actuator with Feedback, 20 µm Travel
PAZ040	$ 915.00	£ 634.30	€ 812,40	¥ 7,726.30	Piezoelectric Actuator with Feedback, 40 µm Travel
PAZ100	$ 1,390.00	£ 963.60	€ 1.234,00	¥ 11,738.00	Piezoelectric Actuator with Feedback, 100 µm Travel

A.8 National instruments 9263

Technical Sales
Norway
66 90 76 60
ni.norway@ni.com

NI 9263

4-Channel, 100 kS/s, 16-bit, ±10 V, Analog Output Module

- 4 simultaneously updated analog outputs, 100 kS/s
- 16-bit resolution
- Hot-swappable operation
- -40 to 70 °C operating range
- NIST-traceable calibration

Specifications

Specifications Documents

- Specifications
- Data Sheet

Specifications Summary

General	
Product Name	NI 9263
Product Family	Industrial I/O
Form Factor	CompactDAQ , CompactRIO
Operating System/Target	Windows , Real-Time
Measurement Type	Voltage
Isolation Type	Ch-Earth Ground Isolation
RoHS Compliant	Yes
Analog Input	
Channels	0 , 0
Single-Ended Channels	0
Differential Channels	0
Analog Output	

Channels	4
Resolution	16 bits
Max Voltage	10 V
Maximum Voltage Range	-10 V , 10 V
Maximum Voltage Range Accuracy	0.11 V
Minimum Voltage Range	-10 V , 10 V
Minimum Voltage Range Accuracy	0.11 V
Update Rate	100 kS/s
Digital I/O	
Bidirectional Channels	0
Input-Only Channels	0
Output-Only Channels	0
Number of Channels	0 , 0 , 0
Counter/Timers	
Counters	0
Physical Specifications	
Length	9 cm
Width	2.3 cm
I/O Connector	Screw terminals
Minimum Operating Temperature	-40 °C
Maximum Operating Temperature	70 °C
Minimum Storage Temperature	-40 °C
Maximum Storage Temperature	85 °C
Timing/Triggering/Synchronization	
Triggers cDAQ Chassis	No

A.9 LabVIEW code for calibrating the phase-step piezo

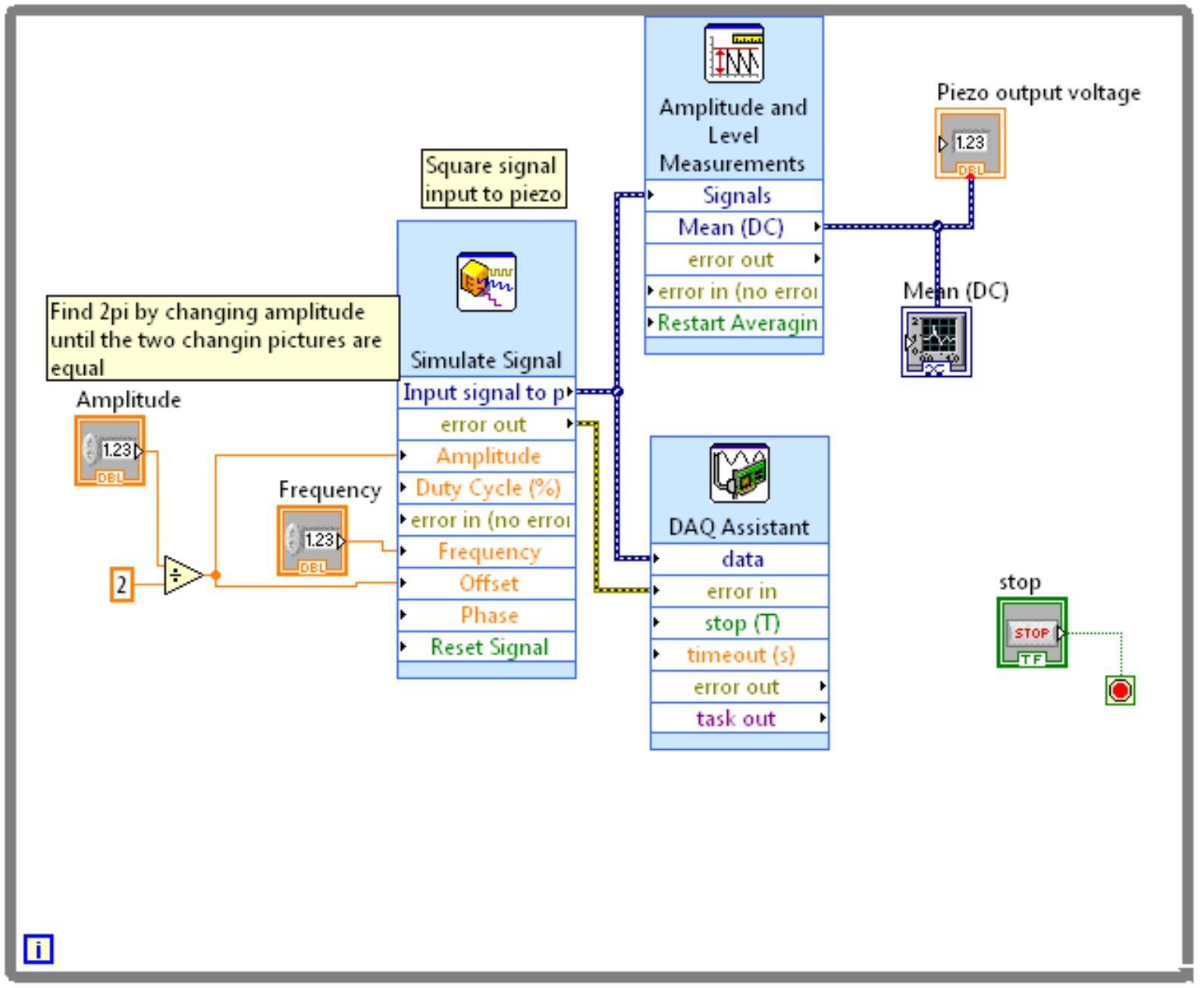
Square signal input to piezo
Find 2pi by changing amplitude until the two changin pictures are equal
Amplitude
Frequency
2
Simulate Signal
Input signal to p
error out
Amplitude
Duty Cycle (%)
error in (no erroi
Frequency
Offset
Phase
Reset Signal
Amplitude and Level Measurements
Signals
Mean (DC)
error out
error in (no erroi
Restart Averagin
Piezo output voltage
Mean (DC)
DAQ Assistant
data
error in
stop (T)
timeout (s)
error out
task out
stop
STOP
TF

A.10 LabVIEW code for recording a phase map

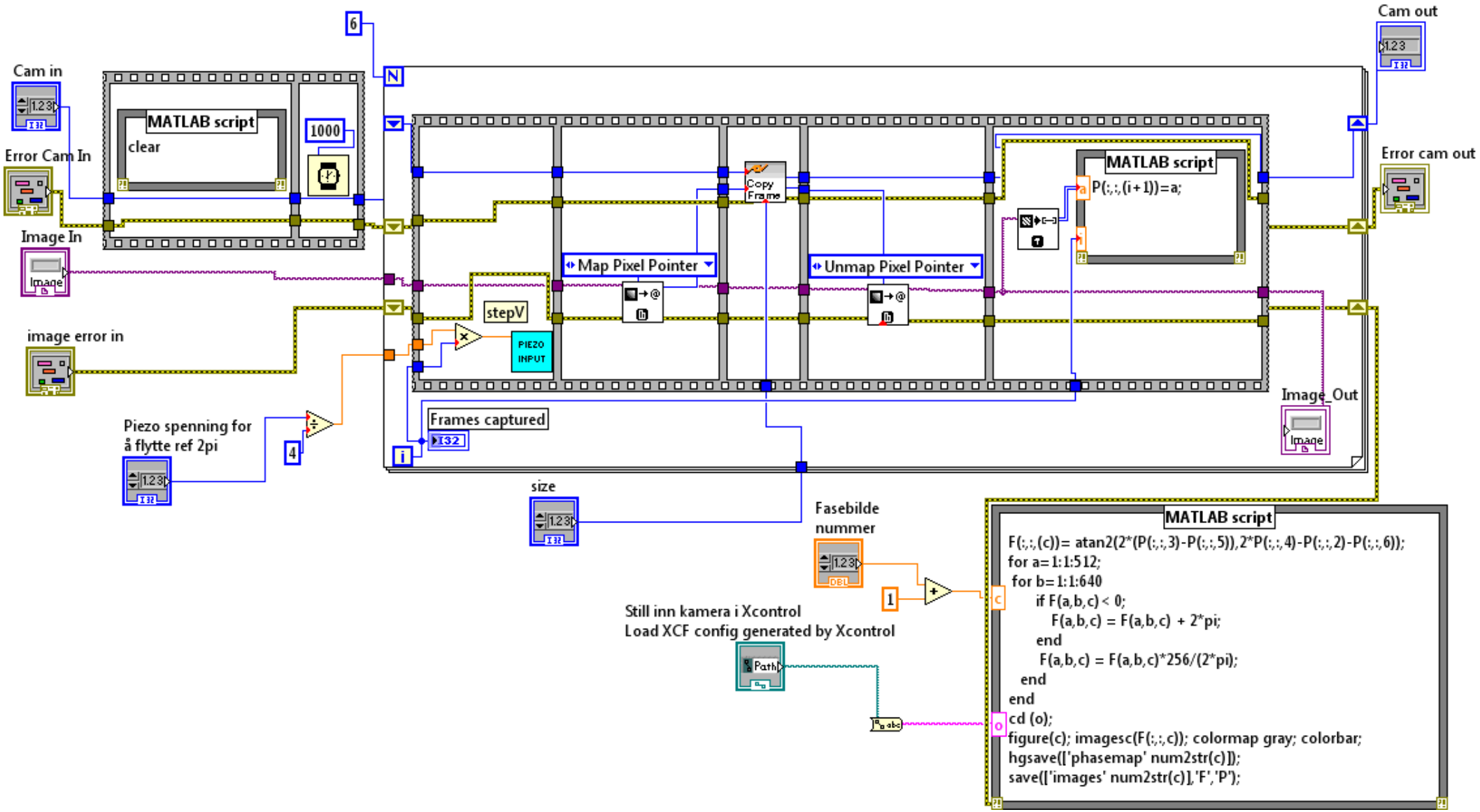
Cam in
Error Cam In
Image In
image error in
Piezo spenning for
å flytte ref 2pi
MATLAB script
clear
1000
6
N
i
Map Pixel Pointer
Unmap Pixel Pointer
Copy
Frame
stepV
PIEZO
INPUT
Frames captured
I32
4
size
MATLAB script
P(:,:,(i+1))=a;
Cam out
Error cam out
Image_Out
Fasebilde
nummer
1
Still inn kamera i Xcontrol
Load XCF config generated by Xcontrol
Path
MATLAB script
F(:,:,(c))= atan2(2*(P(:,:,3)-P(:,:,5)),2*P(:,:,4)-P(:,:,2)-P(:,:,6));
for a=1:1:512;
for b=1:1:640
if F(a,b,c)< 0;
F(a,b,c) = F(a,b,c) + 2*pi;
end
F(a,b,c) = F(a,b,c)*256/(2*pi);
end
end
cd (o);
figure(c); imagesc(F(:,:,c)); colormap gray; colorbar;
hgsave(['phasemap' num2str(c)]);
save(['images' num2str(c)],'F','P');

A.11 LabVIEW code for ramping the piezo

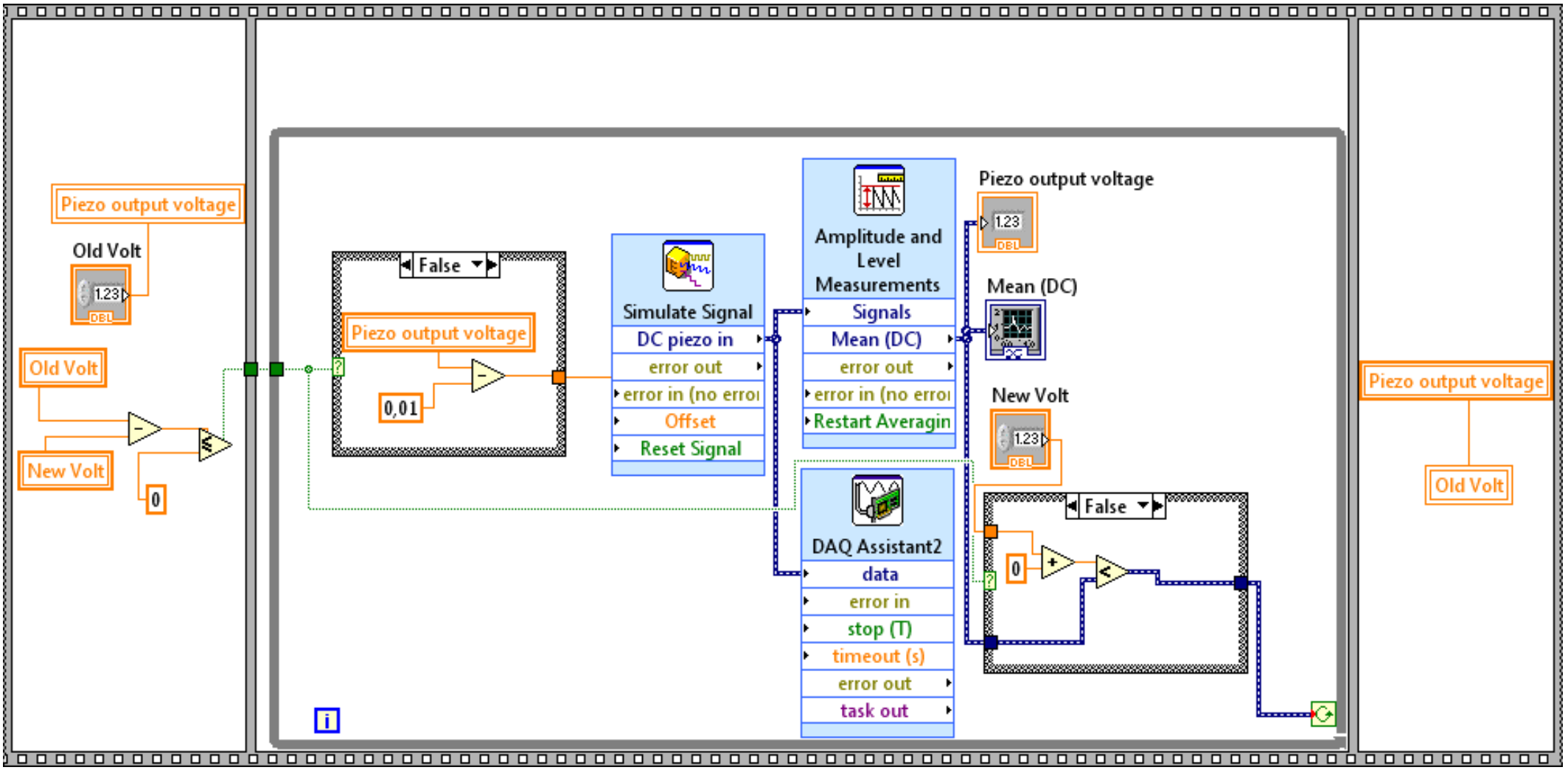
Piezo output voltage
Old Volt
1.23
DBL
Old Volt
New Volt
0
False
Piezo output voltage
0,01
Simulate Signal
DC piezo in
error out
error in (no erroi
Offset
Reset Signal
Amplitude and Level Measurements
Signals
Mean (DC)
error out
error in (no erroi
Restart Averagin
DAQ Assistant2
data
error in
stop (T)
timeout (s)
error out
task out
Piezo output voltage
1.23
DBL
Mean (DC)
New Volt
1.23
DBL
False
0
Piezo output voltage
Old Volt

A.12 LabVIEW code for indentation and phase recording

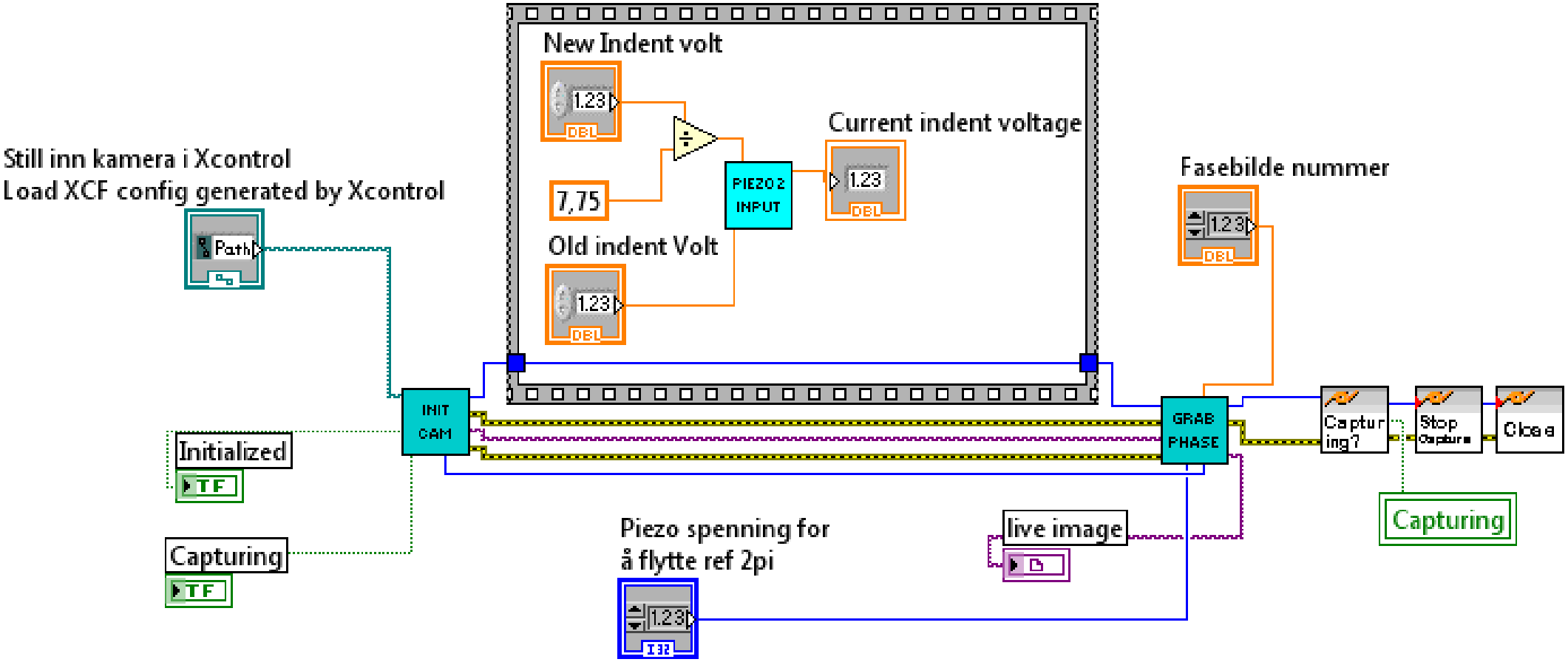
Still inn kamera i Xcontrol
Load XCF config generated by Xcontrol
Path
Initialized
TF
Capturing
TF
INIT CAM
New Indent volt
1.23
DBL
7,75
Old indent Volt
1.23
DBL
PIEZO 2 INPUT
Current indent voltage
1.23
DBL
Piezo spenning for
å flytte ref 2pi
1.23
I32
Fasebilde nummer
1.23
DBL
GRAB PHASE
live image
Captur ing?
Stop Capture
Close
Capturing